

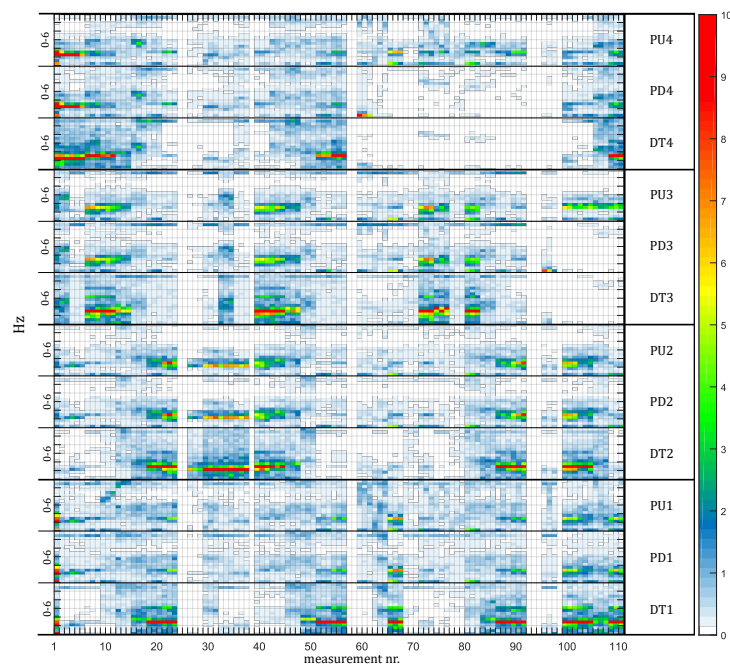
Magnus Farstad Perkunder

Interaction between turbine pressure pulsations and transients in the penstock

Master's thesis in Energy and Process Engineering

Supervisor: Torbjørn K. Nielsen

July 2019



Magnus Farstad Perkunder

*Interaction between turbine pressure
pulsations and transients in the penstock*

Master's thesis in Energy and Process Engineering
Supervisor: Torbjørn K. Nielsen
July 2019

Norwegian University of Science and Technology
Faculty of Engineering
Department of Energy and Process Engineering

EPT-M-2018-xx

MASTER THESIS

for

Student Magnus Farstad Perkunder

Spring 2019

*Interaction between turbine pressure pulsations and transients in the penstock**Interaksjon mellom trykkpulsasjoner fra turbiner og transienter i trykksjakt***Background and objective**

There is an ongoing research project called Fatigue loads in Hydro Turbines, where one of the main issues is to understand how pressure pulsations from the turbine interact with fluid transients in the attached system. These pressure pulsations create fatigue loads and might damage the turbine. Field measurements will be performed at Kviteseid power plant in spring 2019.

Kviteseid power plant has four identical Francis turbines but two of them seem to function in a more problematic way (vibrations, cracks, etc.). The differences in penstock geometry (length and section) for each of the turbine may explain the premature wear of those turbines. Indeed, the time needed for a pressure wave to travel from the turbine to the air cushion chamber and back is different for each turbine, generating varied excitation frequencies. The goal of the field measurements is to find out if and to which extent the differences in the nearest penstock geometry can affect the transient behaviour upstream the turbines and hence the fatigue loads at each turbine.

The objective of this student work is to identify the interaction between the pressure pulsations caused by the turbine and the attached system, with focus on fatigue loads, using both numerical model, model tests and field measurements.

The following tasks are to be considered:

- 1 Investigate resonance frequencies that may occur and plan field measurements at Kvilldal accordingly
- 2 Measure and analyse pressure pulsations in the Francis model turbine at the Hydropower Laboratories
- 3 Complete and assess 1D numerical model for simulating the pressure response of the penstocks to the pressure pulsations due to RSI.
- 4 Measure pressure pulsations on all four turbines of Kvilldal power plant
- 5 Analyse the results with focus on water way resonance and comparison with numerical model
- 6 If the student will go to Nepal for a excursion, earlier and further work will be presented as a publication and presented at the conference; *9th International symposium on Current Research in Hydropower Technologies (CRHT-IX)* at Kathmandu University

The field measurements and analysis of the results will be the main task in the following Master project.

Within 14 days of receiving the written text on the master thesis, the candidate shall submit a research plan for his project to the department.

When the thesis is evaluated, emphasis is put on processing of the results, and that they are presented in tabular and/or graphic form in a clear manner, and that they are analyzed carefully.

The thesis should be formulated as a research report with summary both in English and Norwegian, conclusion, literature references, table of contents etc. During the preparation of the text, the candidate should make an effort to produce a well-structured and easily readable report. In order to ease the evaluation of the thesis, it is important that the cross-references are correct. In the making of the report, strong emphasis should be placed on both a thorough discussion of the results and an orderly presentation.

The candidate is requested to initiate and keep close contact with his/her academic supervisor(s) throughout the working period. The candidate must follow the rules and regulations of NTNU as well as passive directions given by the Department of Energy and Process Engineering.

Risk assessment of the candidate's work shall be carried out according to the department's procedures. The risk assessment must be documented and included as part of the final report. Events related to the candidate's work adversely affecting the health, safety or security, must be documented and included as part of the final report. If the documentation on risk assessment represents a large number of pages, the full version is to be submitted electronically to the supervisor and an excerpt is included in the report.

Pursuant to "Regulations concerning the supplementary provisions to the technology study program/Master of Science" at NTNU §20, the Department reserves the permission to utilize all the results and data for teaching and research purposes as well as in future publications.

The final report is to be submitted digitally in DAIM. An executive summary of the thesis including title, student's name, supervisor's name, year, department name, and NTNU's logo and name, shall be submitted to the department as a separate pdf file. Based on an agreement with the supervisor, the final report and other material and documents may be given to the supervisor in digital format.

- Work to be done in lab (Water power lab, Fluids engineering lab, Thermal engineering lab)
- Field work

Department of Energy and Process Engineering, 10. January 2019

Torbjørn K. Nielsen
Academic Supervisor

Co-Supervisor(s): Celine Faudot, Post Doc at the Waterpower Laboratory

Acknowledgments

This master thesis is written at the Hydropower Laboratory at the Norwegian University of Science and Technology (NTNU) during the spring semester 2019. The work is a continuation of a project assignment carried out by the author during the corresponding fall semester. The fieldwork conducted at Kvilldal hydropower plant was a collaboration between NTNU, Statkraft, and Flow Design Bureau AS (FDB).

The results presented in this thesis would not have been possible without the assistance of several people. I want to take this opportunity to acknowledge my gratitude. Firstly I would like to thank my supervisor, Torbjørn K. Nielsen for his valuable guidance and sharing of knowledge throughout the year. It has been truly inspiring to work with Torbjørn, and our discussions have helped to form this thesis. I would also like to thank my co-supervisor Celine Faudot for her contributions in the discussions with Torbjørn, and all the help related to planning and implementation of the fieldwork. Thank you for all guidance and answers during the last year. Concerning the fieldwork, I would like to thank Andreas Tønnessen and Morten Kjeldsen from FDB for their assistance before and during the measurements at Kvilldal. I would also like to show gratitude to Erik Jacques Wiborg from Statkraft for the collaboration in the planning of the fieldwork, and for making them possible. I am also immensely grateful to Verner Helland for his assistance during the fieldwork. Verner operated the turbines manually during the measurements and helped us with all practical challenges.

I am incredibly grateful to my dear friend Dr. Kjetil Eik Haavik, for the help related to seismic interferometry. Kjetil proposed to apply the post-processing techniques to the measurements in the Hydropower Laboratory and developed the foundation of the MATLAB script used to find the propagation velocity in the penstock. Kjetil also provided useful literature and guidance. I am also appreciative to family members Johan Nedregård, Camilla Farstad, Laura Terragni, and Halfdan Farstad for the valuable input in the completion of this thesis. I would also like to thank postdocs Bjørn Winther Solemslie and Chirag Trivedi for their guidance. Lastly, I would like to thank the Ph.D. Candidates and fellow students at the Hydropower Laboratory for sound advice, exciting discussions, and memorable moments.

Summary

Cracks from fatigue loads are a significant concern in modern high head Francis turbines because the cracks lead to considerable cost for turbine manufacturers and power plant owners. Several cases of developing cracks on runner blades shortly after the runners' operational debut have resulted in the research project called "Fatigue loads in Hydro Turbines". The work presented in this thesis is part of the project and investigate transients in waterways connected to high head Francis turbines through measurements and numerical simulations. Earlier research concludes that rotor-stator interaction is the leading cause of cracks in high head Francis runners. Transients generated by rotor-stator interaction and their ability to cause resonance in the waterways is, therefore, a focus in this assignment.

The main results in this thesis come from measurements conducted at Kvittdal hydropower station, which consists of four High head Francis turbines with separate penstocks. The separate penstocks allow pressure fluctuations generated at one turbine to affect the inlet conditions of other turbines which make the power plant an exciting research object. The turbines were operated manually during the measurements when 111 measurement series were conducted, covering 34 different load combinations. Several of the load combinations involved closed bulb valves. Pressure transducers upstream the closed valves detected transients generated by the draft tube surges at other turbines. Transients related to rotor-stator interaction were observed with small amplitudes in the penstocks close to operational turbines, but not upstream the closed bulb valves.

Measurements performed on the Francis rig in the Hydropower Laboratory at NTNU resulted in the observation of the propagation velocity of transients in the penstock. Application of Seismic interferometry and deconvolution interferometry as post-processing techniques unveiled the propagation velocity during steady-state operation. The propagation velocity of transients has a crucial role in terms of resonance in waterways, which may lead to cracks resulting from fatigue in structural components due to an increase in stress.

A separate chapter presents the creation of one-dimensional models of the waterways upstream the turbines at Kvittdal and the penstock in the Hydropower Laboratory. The models are based on the characteristics method and are used to investigate the behavior of transients. The model of the penstock in the Hydropower Laboratory played a crucial role in the development and validation of seismic interferometry and deconvolution interferometry as post-processing techniques. Results from the measured data were compared against, the model which has a known wave-speed.

Knowing the wave-speed is valuable for designers who try to prevent resonance in power plants. Therefore, further research on how to best apply seismic interferometry and deconvolution interferometry as post-processing techniques are needed. Results were inconclusive when the methods were applied to the data from Kvittdal.

Sammendrag

Utmattingsbrudd er et kjent problem i moderne høytrykks Francisturbiner. Når et løpehjul sprekker, medfører dette store kostnader for både eier av kraftverket og leverandøren av hjulet. Det er dokumentert flere tilfeller av snarlig etter installasjon av nye løpehjul, noe som er bakgrunnen for at forskningsprosjektet *Fatigue Loads in Hydro Turbines* ble igangsatt. Denne masteroppgaven bidrar til prosjektet ved å undersøke transienter i komplekse vannveier som er tilknyttet høytrykk Francisturbiner. Tidligere studier har konkludert med at rotor-stator interaksjon er en hovedårsak til sprekkdannelsene i flere høytrykksmaskiner. Transienter generert av rotor-stator interaksjon har derfor vært et hovedfokus i denne oppgaven.

Hovedresultatene i oppgaven kommer fra trykkmålinger som ble gjort på Kvittdal kraftverk. Vannkraftverket består av fire høytrykk Francisturbiner med separate trykksjakter. Trykksjakterne er koblet sammen oppstrøms noe som tillater transienter generert av én turbin til å påvirke en annen. Det komplekse vannveisystemet gjør Kvittdal til et interessant forskningsobjekt med tanke på transienter. Feltmålingene består av totalt 111 måleserier som dekker 34 driftspunkter. Turbinene ble operert manuelt og noen av måleseriene ble gjort med stengte kuleventiler på en eller to turbiner. Plassering av trykksjakter oppstrøms de avstengte kuleventilene muliggjorde måling av transienter i trykksjakter som kun var påvirket av de operative turbinene. Transienter relatert til rotor stator interaksjon ble observert ved innløpet til aktive turbiner, men ikke oppstrøms de avstengte kule ventilene.

Målinger ble også gjort på Francisriggen i Vannkraftlaboratoriet på NTNU, mens turbinen opererte under stabile forhold, og resulterte i at bølgehastigheten i trykksjakten ble konstatert. Arbeidet innebar applikasjon av henholdsvis seismiskinterferometri og dekonvolusjonsinterferometri som postprosesserings teknikker. Det er viktig å kjenne verdien til bølgehastigheten siden den har en sentral rolle i mulig forekomst av resonans i vannveiene. Resonans bidrar til økt belastning på strukturelle komponenter og øker sannsynligheten for utmattingsbrudd.

Numeriske modeller, av vannveiene på Kvittdal og trykksjakten i Vannkraftlaboratoriet på NTNU er også blitt konstruert. De er basert på karakteristikkmetoden. All teori, alle antagelser og beskrivelse av hvordan metoden er implementert er samlet i et eget kapittel. Modellene er i hovedsak brukt til å undersøke trender i spektralanalysen som funksjon av ulike konstanter og variabler, men modellen av trykksjakten i Vannkraftlaboratoriet hadde også en viktig rolle i utviklingen av seismiskinterferometri og dekonvolusjonsinterferometri som postprosesserings teknikker. Resultatene fra måledataene ble sammenlignet med resultatene fra de simulerte dataene hvor bølgehastigheten er en kjent konstant.

Kjennskap til bølgehastigheten er verdifull i designfasen av vannveisystemer hvor det er viktig å minimere risikoen for resonans. Videre arbeid med utvikling av de nevnte postprosesserings teknikkene er derfor å anbefale. Resultatene fra måledataene fra Kvittdal viste ikke bølgehastigheten.

Nomenclature

δ_2	blade thickness
δ_v	boundary layer thickness added to blade thickness
ω	angular coordinate related to static frame of reference
ϕ	phase
ψ_j	constant used in the characteristics Method
ρ	fluid density
σ_D	classical fatigue limit in SN-diagram
τ	valve closure relationship
τ_0	wall shearing stress
θ	angle coordinate
A	Area of pipe, Amplitude
a	propagation velocity also referred to as wave speed
A_G	area of valve opening
B	amplitude
C^+, C^-	name for characteristics equations
C_d	discharge coefficient
C_v	constant, combining valve parameters
CM, CP	known constants in characteristics equation
D	pipe diameter
E	modulus of elasticity
E_m	constant related to valve closure

f	Darcy-Weisbach friction factor, frequency of pressure pulsation
f_{Bs}	blade passing frequency, related to number of blades at runner inlet
f_f	fundamental frequency of a pipe system
f_{gvr}	guide vane passing frequency, related to number of guide vanes
f_k	Von Karman vortex frequency
f_{Rhein}	Rheingans frequency
f_{upv}	frequency of upper draft Tube Vortex Rope
g	gravitational acceleration
H	instantaneous piezometric head
H_0	steady-state or mean pressure head
K	bulk modulus of elasticity
k	diametrical mode
k_1	empirical constant related to blade geometry
L	length of pipe
M, N	harmonic order
N	runner speed rpm, in relation to specific speed calculation in figure 3.4
n	rotational speed of runner
N_f	number of cycles in SN-diagram
nq	specific speed figure 3.4
P	pressure
Q	instantaneous discharge at a section
R	resistance coefficient
Re_x	Reynolds number at location x
S	stress amplitude in SN-diagram
St	Strouhal number
t	time
t_c	time of closure of a valve
T_f	fundamental time of a pipe section

V	instantaneous velocity
V_0	steady state or mean velocity
W	mean velocity at the separation point of a hydrofoil
W_2	mean velocity outside wake
x, y	coordinates
y	constant in relation to the upper part load cortex
Z_B	number of impeller blades
Z_{gv}	number of guide vanes
C_1	absolute velocity runner inlet
C_2	absolute velocity runner outlet
C_m	axial velocity component
C_t	tangential velocity component
U_1	peripheral velocity at runner inlet
U_2	peripheral velocity at runner outlet
W_1	relative velocity at runner inlet
W_2	relative velocity at runner outlet

Table of Contents

Acknowledgements	4
Summary	i
Sammendrag	ii
Nomenclature	iii
Table of Contents	ix
List of Tables	xi
List of Figures	xv
Abbreviations	xvi
1 Introduction	1
2 Kvittdal power plant	3
2.1 Kvittdal History	3
2.1.1 Turbine 3	4
3 Basic Theory	7
3.1 Francis Turbine	7
3.1.1 Splitter Blade Runner	8
3.2 Flow Features in Reaction Turbines	9
3.2.1 Rotor Stator Interaction	10
3.2.2 Draft Tube Vortex Rope	14
3.2.3 Von Karman Vortex Rope	17
3.2.4 Turbulence And Cavitation	19
3.2.5 Summary of the Frequencies Related to Flow Features	20
3.3 Fatigue and Structural Natural Frequencies	20
3.3.1 Fatigue in metals	20
3.3.2 Structural Natural Frequencies	21
3.4 Transients and Resonance in Waterways	22
3.4.1 The Propagation Velocity	23

3.5	Seismic Interferometry	26
4	One Dimensional Numerical Models	29
4.1	Kvilldal	29
4.2	Hydropower Laboratory	31
4.3	Theory	32
4.3.1	Fundamental Equations Transient Pipe Flow	32
4.3.2	Characteristics Method and Finite Differences	32
4.3.3	Assumptions and Boundary Conditions	34
4.4	Validation and Verification	40
4.5	Running a Simulation	42
5	Measurement Setup and Equipment	45
5.1	Pressure Transducers	45
5.2	Experimental setup	46
5.2.1	Hydropower Laboratory	46
5.2.2	Kvilldal	48
5.2.3	Uncertainties	49
6	Experimental Method	51
6.1	Hydropower Laboratory	51
6.1.1	Seismic Interferometry Plots	52
6.2	Kvilldal	54
6.3	Simulation of Kvilldal	58
7	Results	59
7.1	Hydropower Laboratory	59
7.1.1	Seismic Interferometry and Deconvolution interferometry on Simulated Data	59
7.1.2	Seismic Interferometry and Deconvolution interferometry on Experimental Data	61
7.2	Kvilldal One Dimensional Model	63
7.2.1	Changing Blind Tunnel	63
7.2.2	Closing Different Turbines	64
7.2.3	Waterway Configurations	66
7.2.4	Simulating With Different Wave-Speeds	68
7.3	Kvilldal hydropower plant	71
7.3.1	Seismic Interferometry	71
7.3.2	Turbine Data and Pulsation Frequencies	71
7.3.3	Operational Loads and Waterway Configurations	72
7.3.4	RSI	73
7.3.5	Operation Load and Rheingans Frequency	75
7.3.6	Case 1. Waterway Configuration	77
7.3.7	Case 2. Transient Events	81

8 Discussion	87
8.1 Hydropower Laboratory Seismic Interferometry and Deconvolution Interferometry	87
8.1.1 Simulated Data	87
8.1.2 Measured Data	87
8.2 Kvilldal Hydropower Plant	88
8.2.1 Simulations	88
8.2.2 Measurements	88
9 Conclusion	93
10 Further Work	95
Bibliography	97
Appendix A	I
Appendix B	II
Appendix C	III
Appendix D	XII
Appendix E	XVI
Appendix F	XXVIII
Appendix G	XXXIX

List of Tables

3.1	Main resonance conditions in a Francis turbine, recreated from [9].	20
5.1	Pressure transducers at the Hydropower Laboratory at NTNU	46
5.2	Pressure Transducers at Kvilldal	46
5.3	Placement of the pressure transducers at the Hydropower Laboratory at NTNU	47
6.1	Waterway configuration cases investigated.	55
6.2	Transient events and measurement series numbers.	55
6.3	Operating points, Turbine power output and measurement series numbers related to each operation point.	57
7.1	Turbine data at Kvilldal from Giskehaug [16].	71
7.2	Approximations of the expected frequencies related to flow features in the turbines at Kvilldal.	71
7.3	Notes related to different waterway configurations in figure 7.14.	79

List of Figures

2.1	Kvilldal power plant overview of the system. Taken from [16]	4
3.1	a) Axial view of high head Francis turbine. Taken from [3]. b) 3D model of runner with RSI loads. Taken from [22]	8
3.2	a) Runner with splitter blades [19]. b) illustration of how blades are numbered at Kvilldal.	9
3.3	Typical frequencies related to pressure fluctuations in reaction turbines. Taken from [9]	9
3.4	Level of dynamic stresses caused by RSI in hydraulic turbine [41]. GPF=gate passing frequency, $nq = \frac{NQ^{0.5}}{H^{0.75}}$	10
3.5	Stream lines between two guide vanes, redrawn from [3].	11
3.6	Sketch of how six channels in the runner at Kvilldal are facing an open guide vane channel. a) position 1. b) Rotated to the next channel.	11
3.7	a) Dynamic stress on high head Francis runner with $Z_B = 17$, $Z_{gv} = 28$, $m = 2$, $n = 1$ results in $ND = 6$ [22]. b) Illustration of rotor stator interaction	12
3.8	RSI modes [39]	12
3.9	Modeled RSI pressure distribution with data from Kvilldal. $k=6$ which implies that the field rotates in the clock wise direction.	14
3.10	Velocity diagram of a Francis turbine at different operating points. Redrawn from [13]	15
3.11	Draft tube vortex rope during part load. Taken from [9].	16
3.12	Von Karman vortices behind stay vanes and guide vanes [9].	17
3.13	a) Francis turbine blade. b) Kaplan turbine blade. c) vortex street behind the blade. [50]	19
3.14	SN curve, S is the stress amplitude, N_f is the number of cycles. Redrawn from [6]	21
3.15	Traveling and standing pressure wave. Taken from [36]	22
3.16	Propagation velocity in a mixture of water and air as a function of the volume percentage of air in the mix. Reconstructed from [11].	24
3.17	Seismic interferometry infinitely long pipe. Taken from [49]	26
3.18	Seismic interferometry pipe with reflection. Taken from [49]	27
4.1	Elements in model used to simulate Kvilldal.	29
4.2	Simulation elements used to simulate the Hydropower Laboratory together with a 2D drawing of the Francis rig in the hydropower laboratory.	31

4.3	Method of Characteristics computational domain.	33
4.4	Representation of the computational domain related to junction 4 in the 1D model of Kvilldal. The center of the junction is the common point <i>pipe1.NS</i> , <i>pipe2.1</i> and <i>pipe6.1</i>	36
4.5	Representation of the computational domain related to the series junction between pipe 6 and pipe 7 in the 1D model of Kvilldal.	37
4.6	Flow at reservoir in the beginning of a simulation used to verify the simulation model.	41
4.7	Independence study of simulation length, T_{max}	41
4.8	Transient plot of pressure in the conduit at Kvilldal. The flow at all turbines is set to zero at $t = 0$	43
5.1	Pressure transducers in the Hydropower laboratory at NTNU.	45
5.2	Francis rig at NTNU in open loop configuration. (1) centrifugal pump, (2) and (3) open water channel, (4) upstream pressure tank, (5) flowmeter, (6) generator, (7) Francis turbine, (8) downstream pressure tank, (9) water outlet to basement.	46
5.3	2D illustration of location of pressure transducers in the Laboratory at NTNU	47
5.4	2D sketch of the inlet, bulb valve, spiral casing and draft tube cone at Kvilldal. Measurements in <i>mm</i> with the uncertainty.	48
5.5	2D sketch of where the different pressure transducers are located at Kvilldal.	48
6.1	Seismic interferometry plot explained.	52
6.2	Power output for each turbine during the measurements.	56
7.1	Seismic interferometry applied to simulated data.	59
7.2	Deconvolution interferometry applied to simulated data.	60
7.3	Seismic interferometry applied to measurements from the Hydropower Laboratory.	61
7.4	Deconvolution interferometry applied to measurements from the Hydropower Laboratory.	62
7.5	4 cases simulated, spectral analysis from changing blind tunnel lengths.	63
7.6	4 cases simulated, spectral analysis from closing different turbines.	64
7.7	4 cases simulated with a combination of closed bulb valves and excitation forces. Spectral analysis with high amplitudes.	66
7.8	4 cases simulated with a combination of closed bulb valves and excitation forces. Spectral analysis with low amplitudes	67
7.9	Spectral analysis of the simulation of measurement series 72-74 in the experimental results focusing on large amplitudes.	68
7.10	Spectral analysis of the simulation of measurement series 72-74 in the experimental results focusing on small amplitudes.	69
7.11	Operation points with different waterway configuration.	72
7.12	Spectral analysis in the range 164-170 <i>Hz</i> from all steady state measurements.	73
7.13	Max amplitude in the Rheinegans frequency range, 1.45-1.55 <i>Hz</i> , together with the load for each measurement.	75
7.14	Case 1. Waterway configurations as described in table 6.1. Spectral analysis amplitudes of all sensors 0-6 <i>Hz</i>	77
7.15	Case 1. Some highlighted measurement series from Case 1.	80

7.16	Case 2. Transient measurements. Spectral analysis of of transient measurements for all sensors in the range 0-6 Hz.	81
7.17	Measurement series 93.	82
7.18	Measurement series 93 filtered.	83
7.19	Spectral analysis of measurement 93, Turbine 4 & 3	85
7.20	Spectral analysis of measurement 93, Turbine 2 & 1.	86
10.1	Ulla Førre Power plant system	I
10.2	Kvilldal turbine [30]	II
10.3	Picture of pressure transducer placed on the draft tube of turbine 1.	XII
10.4	Picture of pressure transducer placed on the draft tube of turbine 2.	XIII
10.5	Picture of pressure transducer placed on the draft tube of turbine 3.	XIII
10.6	Picture of pressure transducer placed on the draft tube of turbine 4.	XIV
10.7	Picture of pressure transducer placed upstream the bulb valve, (PU1, PU2, PU3, PU4). The mounting is similar on all the turbines.	XIV
10.8	Picture of pressure transducer placed downstream the bulb valve, (PD1, PD2, PD3, PD4). The mounting is identical on all the turbines.	XV
10.9	Spectral analysis of measurement 93-98, Turbine 4.	XVI
10.10	Spectral analysis of measurement 60-90, Turbine 3.	XVII
10.11	Spectral analysis of measurement 60-90, Turbine 2.	XVIII
10.12	Spectral analysis of measurement 60-90, Turbine 1.	XIX
10.13	Spectral analysis of measurement 93-98, Turbine 4.	XX
10.14	Spectral analysis of measurement 93-98, Turbine 3.	XXI
10.15	Spectral analysis of measurement 93-98, Turbine 2.	XXII
10.16	Spectral analysis of measurement 93-98, Turbine 1.	XXIII
10.17	Spectral analysis of measurement 99-111, Turbine 4.	XXIV
10.18	Spectral analysis of measurement 99-111, Turbine 3.	XXV
10.19	Spectral analysis of measurement 99-111, Turbine 2.	XXVI
10.20	Spectral analysis of measurement 99-111, Turbine 1.	XXVII

Abbreviations

CFD	=	Computational Fluid Dynamics
GPF	=	Gate Passing Frequency
RSI	=	Rotor Stator Interaction
PU	=	Penstock Upstream bulb valve
PD	=	Penstock Downstream bulb valve
DT	=	Draft Tube
NTNU	=	Norwegian Institute of Science and Technology
FDB	=	Flow Design Bureau AS

Introduction

This master thesis is part of an ongoing research project called Fatigue loads in hydro turbines. A primary goal for the project is to understand the interaction between pressure pulsations generated by reaction turbines and transients in the waterways. Several high head Francis turbines have experienced cracks from fatigue after a short operational period, and this thesis investigates the behavior of transients at Kvilldal hydropower plant where such events took place.

Pressure pulsations cause increased stress on structural components, which lead to fatigue, and transients exciting resonance in the waterways rise pressure and flow fluctuations. High head Francis turbines are reaction turbines where pressure fluctuations generated by the turbines interact directly with the water in the penstock. Turbines can, therefore, provoke transients which may induce resonance in the waterway. Kvilldal hydropower plant consists of four high head Francis turbines with separate penstocks. The geometry, characteristics, and history of Kvilldal are presented in the next chapter. Separate penstocks allow transients to develop and interact with the turbines, which makes Kvilldal an interesting research object. The literature study presented in chapter 3 intends to describe what a Francis turbine is and how turbines generate pressure fluctuations. The study also presents how transients develop in pipes and how resonance can occur. Chapter 3 also includes some theory concerning materials behavior and how fatigue in turbines can originate. Chapter 4 presents the governing equations in pipe flow and how the application of the method of characteristics can solve them. The chapter also includes all assumptions and conditions used in the one dimensional model of the complex waterway system at Kvilldal.

Pressure measurements and post-processing of measured data are the main focus of this thesis. However, numerical simulation models have also been used to investigate transients behavior in intricate waterways, and to compare the measured data with known systems. Experiments conducted in the Hydropower Laboratory at NTNU have involved the development of measurements and post-processing techniques as a preparation for the work related to the measurements at Kvilldal. Application of seismic interferometry and deconvolution interferometry resulted in the scientific paper in appendix F.

The fieldwork at Kvilldal was conducted 7th of May 2019 and was a collaboration between NTNU, FDB, and Statkraft. FDB stands for Flow Design Bureau AS. FDB specializes in flow measurements in hydropower plants and were responsible for most of the pressure transducers

and the data acquisition during the measurements. Statkraft is the owner of the power station and assisted with the planning and execution of the experiments. 111 measurements series were performed during 34 different operational points. The four turbines were operated on a wide load range also consisting of points with one or two closed turbines. Closing the bulb valves enabled measurements upstream the valves where transients only originate from the other turbines.

Kvilldal power plant

Kvilldal power plant is part of Ulla Førre power plant system which consists of 4 power plants and 2 pump stations. Appendix A includes an illustration of the system. Kvilldal has four 310 *MW* high head Francis turbines with separate penstocks. The head is 535 *m*, and the power plant is the largest in Norway in terms of installed effect [42]. Figure 2.1 presents an overview of the waterways at Kvilldal, and a picture of the turbine can be seen in Appendix B. The complex conduit system at Kvilldal is the reason why field measurements were conducted there as part of this master thesis.

As seen in figure 2.1, the four turbines are connected upstream and downstream. Upstream the turbines have separate penstocks. The part of the penstocks closest to the turbines are steel pipes with almost identical length and diameter. Above the trash racks in figure 2.1 the penstocks are rock tunnels in the mountain. These tunnels connect in upstream junctions which connect to a headrace tunnel, leading to an air cushion chamber. The air cushion chamber is the largest in the world and is designed to dampen transients in the system [42] [34].

The difference in penstock length between each turbine and the junctions is the factor that makes Kvilldal suited for the investigation of transients in a complex conduit. The junctions and the air cushion chamber act as reflection points for transients [11]. If transients reflect in an unfortunate manner, resonance may occur in parts of the system, and structural parts may experience increased loads [4]. Chapter 3 presents the theory needed to understand transients and how resonance can appear.

2.1 Kvilldal History

The information in this section is taken from a master thesis written by Sindre Gidskehaug in 2010 at NTNU [16].

Kvilldal power plant was completed in 1986, but the turbines were connected to the grid as construction of separate sections were completed. The turbines are numbered 1-4. turbine 1 is the one lowest in figure 2.1 while 4 is the uppermost turbine.

Kvittdal is operated to meet a calculated power demand that alters from day to day. The operation of the turbines is, therefore, over an extensive load range, which increases the probability of unfavorable operating conditions. Turbine 3 and 4 have been experiencing many cracks as a result of fatigue loads since the operational debut. Turbine 4 and turbine 3 were operative in respectively 1981 and 1982.

Statkraft is the primary owner of the power plant, and treat all four turbines as identical. However, turbine 1 and 2 were delivered at a later stage and constructed differently than 3 and 4. The main difference between the turbine pairs is the choice of welding material, which may be part of the explanation to cracks appearing in the welds. Note also that the construction of the turbines happened at a time when the production precision was lower than today, this would allow more significant individual differences and is a possible explanation for the history of turbine 3.

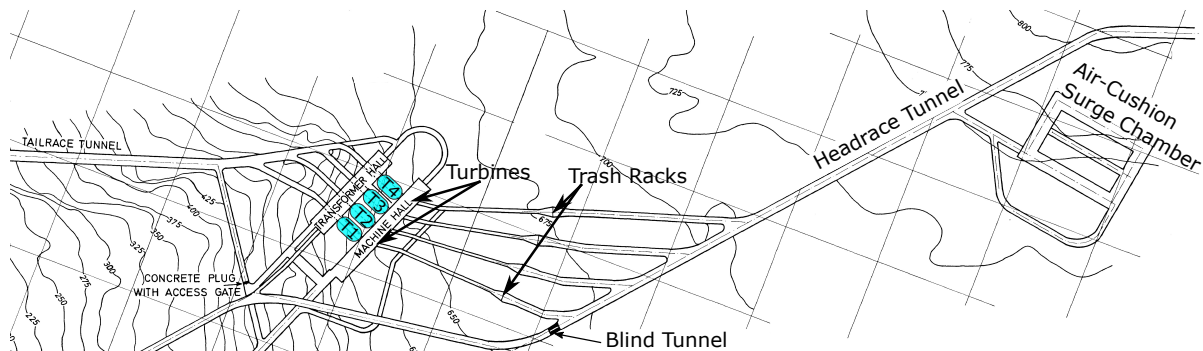


Figure 2.1: Kvittdal power plant overview of the system. Taken from [16]

2.1.1 Turbine 3

Turbine 3 is the turbine at Kvittdal with the most troubled history in terms of cracks resulting from fatigue. In early years the turbine vibrated violently at high loads which is assumed to be a contributing factor for the following history of events [16]. Figure 3.2 and Figure 3.1 describes the parts involved in the events and they're location on the turbine.

- *1988*: The first indication of crack formation is detected at main blades 1, 14 and 15.
- *1989*: The turbine was taken out of operation for 13 months. The runner needed repair, as a 2 m long S-shaped crack on blade 15 was detected. The crack developed from the middle of the blade tip at the runner outlet and ran up towards the inlet. Blade 15 is a main-blade, meaning that it runs through the entire turbine. 80% of the blade needed replacement, and the maximum load was limited from 310 MW to 290 MW.
- *2000*: The turbine was out of operation for 19 months. A crack at main-blade 15 was detected again. The crack was at the trailing edge of the blade and connected to the runner

band. The entire blade was replaced. As a consequence, the air entrainment system was modified, which resulted in a noticeable reduction in vibrations. The maximum load limitations imposed in 1989 was raised.

Det Norske Veritas, DNV, conducted an analysis of the blade after the incident which concluded that the crack resulted from fatigue. DNV also concluded that the crack most likely originated from the weld between the runner band and the blade.

- 2002: The runner needed repair again, and operation stopped, due to the detection of a 420 *mm* long crack on main-blade 14. The crack ran from the trailing edge of the blade towards the center of the blade. A new restriction was introduced, limiting power production to 288 MW.
- 2008: The turbine was taken out of operation, as a large crack in the weld between main blade 14 and the runner crown was detected. DNV analyzed the incident and concluded that the crack was caused by fatigue. The crack started at the high-pressure side on the trailing edge of the blade. DNV also uncovered a previous weld repair in the area of the crack. Giskehaug remarks that the welding material had different material properties than the impeller material [16].

Basic Theory

This chapter describes the basic theory needed to understand how the turbines at Kvilldal can generate pressure and flow fluctuations during steady state. It also has a brief introduction to some basic material properties and the natural frequency of Francis runner. Finally, the chapter discusses how resonance condition in waterways originates and the governing parameters, with focus on the propagation velocity.

3.1 Francis Turbine

The Francis turbine is the most efficient of the hydro turbines. The statement means that it converts more of the available energy in the flow to mechanical energy at the shaft than any other hydro turbine [9]. Francis turbines are applicable for heads between 25 and 700 meters and are the most used turbine type in Norway [1]. Figure 3.1 illustrates a high head Francis turbine and some of its main features. Figure 3.2 shows a splitter blade impeller and how the numbering of the blades at Kvilldal are arranged.

The main features of a Francis turbine are:

1. *The spiral casing*, where flow from the penstock is distributed around the runner and given a rotation.
2. *The stay vanes*, which sit in the spiral casing. They direct the flow towards the guide vanes and act as structural support.
3. *The guide vanes*, which act as a final gate into the runner. Flow is regulated by pivoting the guide vanes. The whole set of guide vanes is often referred to as the wicket gate.
4. *The runner*, which hangs on the turbine shaft. Seals on the lower and upper cover prevent direct contact between the rotating runner and the static structure.
5. *The draft tube*, that sits under the outlet of the runner and is designed to convert kinetic energy at the runner outlet to pressure energy at the draft tube outlet [3].

The Francis turbine is a reaction turbine, which means that it converts both pressure energy and kinetic energy in the flow to mechanical energy at the turbine shaft [3]. The flow through a

reaction turbine and the flow in the waterways are directly linked. The connection allows transients in the penstock and draft tube to interact with the turbine. Pressure fluctuations produced by the runner will, therefore, propagate in the attached waterway system.

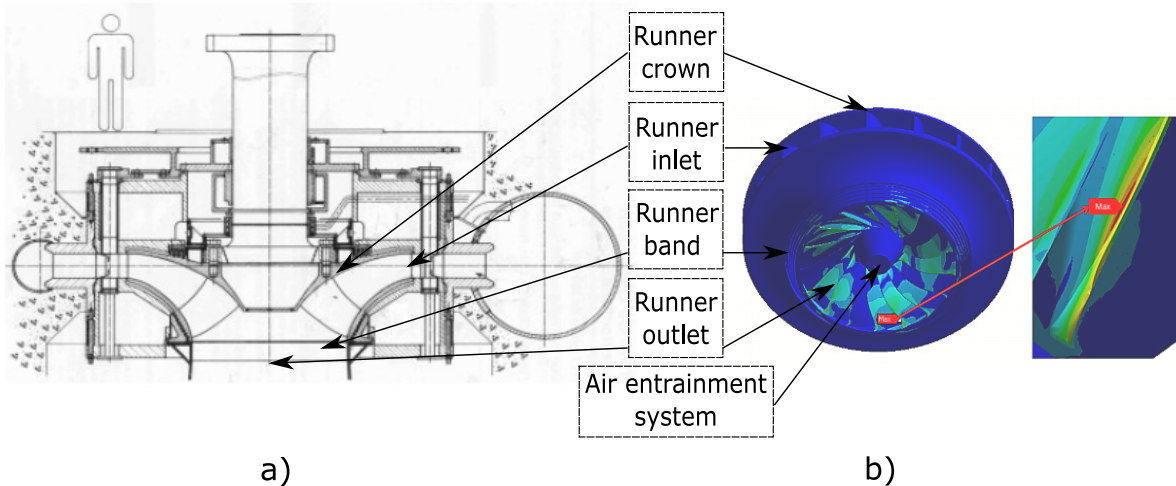


Figure 3.1: **a)** Axial view of high head Francis turbine. Taken from [3]. **b)** 3D model of runner with RSI loads. Taken from [22]

3.1.1 Splitter Blade Runner

The runner at Kvittdal is a splitter blade runner. The Lubuge station first successfully used such a runner in 1980, and it has since then been a popular choice in high head Francis installations [21]. An illustration of a splitter blade runner and how the blades are numbered at Kvittdal is given in Figure 3.2.

The main difference between a regular runner and a splitter-blade runner is that only half of the blades run from the inlet to the outlet. Figure 3.2 illustrates the difference between main-blades and a splitter-blades in a splitter-blade runner. Conventional Francis runners only consist of main-blades. The splitter-blade runner's design results in some beneficial attributes which are presented below as described by Masami Harano, Kiyohito Tani and Satoru Nomoto in 2006 [19].

1. There are *fewer blades at the outlet of the runner*, which means that the blades can be lengthened towards the center of the runner, (the hub). Extending the blades decreases the swirling flow at the outlet of the runner, which results in lower kinetic rotational energy. The latter improves the flow characteristics and efficiency during, both part load and high load operation. The decrease in rotating flow also reduces draft vibration, head cover vibration, and low-frequency vibrations related to part load.
2. There are *more blades at the inlet of the runner*. The load per blade is reduced, so that cavitation at the inlet becomes less likely. Flow at the inlet is more difficult to detach, which result in more flexible operating conditions.

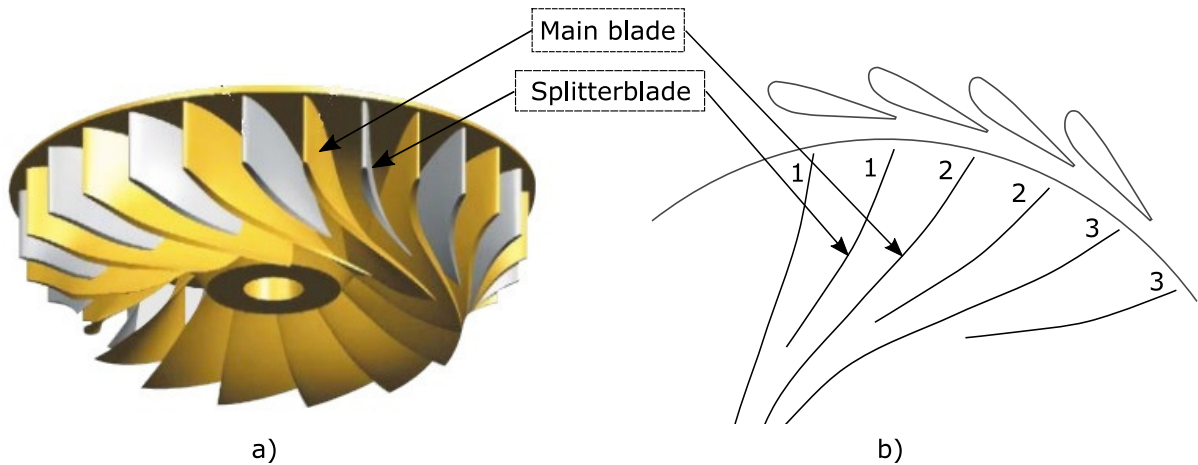


Figure 3.2: a) Runner with splitter blades [19]. b) illustration of how blades are numbered at Kvittdal.

3.2 Flow Features in Reaction Turbines

Mechanical, electrical and hydraulic forces are the three possible sources of vibration in hydropower plants [50]. During the field measurements at Kvittdal in May 2019, all turbines were operated on a wide load range. The investigation of flow features causing pressure fluctuations in the runner has been essential in terms of understanding the measured data during post-processing. Figure 3.3 displays frequencies related to pressure fluctuations that may occur in hydraulic machines and humans sensitivity to noise. The following sections address the sources of many of these frequencies.

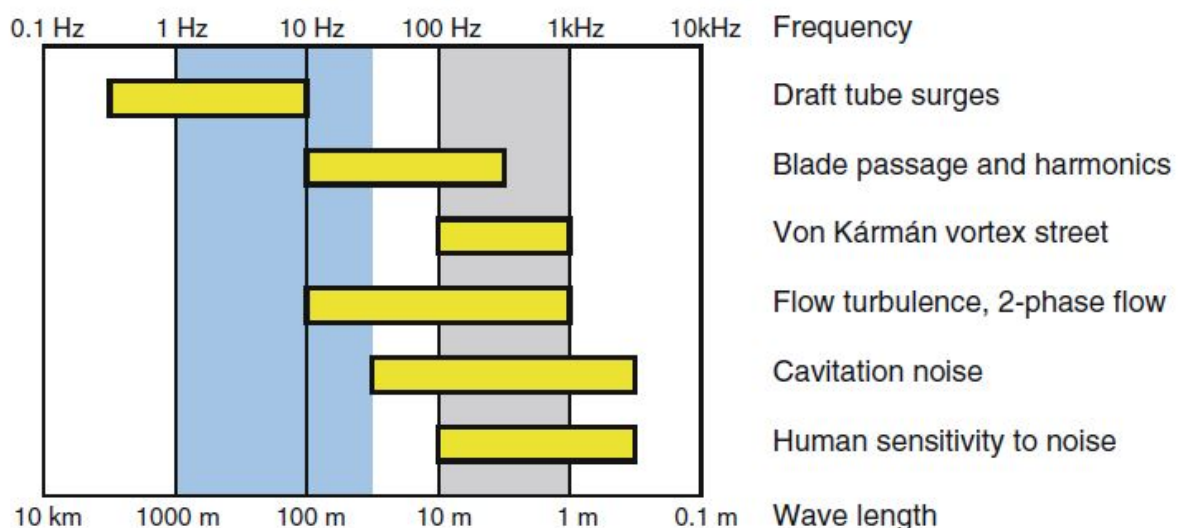


Figure 3.3: Typical frequencies related to pressure fluctuations in reaction turbines. Taken from [9]

3.2.1 Rotor Stator Interaction

Rotor Stator Interaction, RSI, is known to be the source of machine failure and of considerable costs in several hydropower plants [39] [45]. RSI causes pressure fluctuations in the water as the rotating runner interacts with the flow from the static guide vanes. High head Francis turbines are extra vulnerable to RSI as U.Seidel et al. conclude in a study on RSI effects in Francis turbines from 2012 [41]. Figure 3.4, from the study, shows that RSI causes approximately 80% of the total stresses in high head Francis turbines. In figure 3.3 RSI is covered by blade passage and harmonics, note that the frequency range covers the expected first harmonic of the natural frequency of a runner, $70 - 300Hz$ [45].

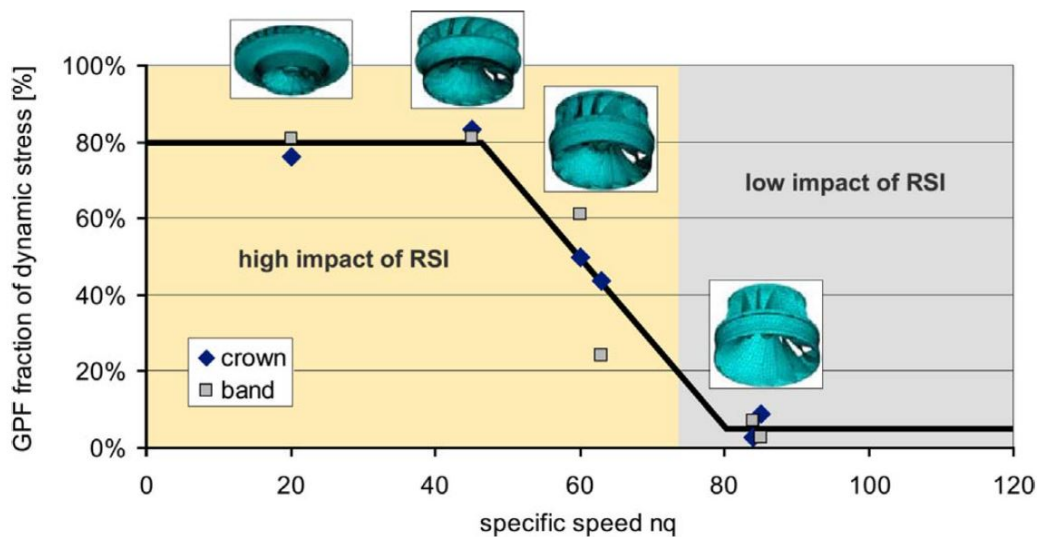


Figure 3.4: Level of dynamic stresses caused by RSI in hydraulic turbine [41]. GPF=gate passing frequency, $nq = \frac{NQ^{0.5}}{H^{0.75}}$

The distance from the wicket gate to the runner is one of the main differences between high and low head Francis turbines. The wakes behind the guide vanes induce mixing, so when the distance increases, the pressure field in the flow into the runner gets more evenly distributed. High head Francis machines are also related to greater velocities and thinner blades. The factors mentioned make high head machines vulnerable to fatigue caused by RSI [9].

Figure 3.5 shows potential flow streamlines through a pair of guide vanes [51]. The pressure distribution on top of the guide vanes needs to be greater than the pressure on the bottom to bend the streamlines as in the figure. The inlet of the runner will, therefore, face a high- and low-pressure region as it passes a guide vane.

The number of guide vanes and runner blades are designed to evenly distribute channels in the runner that experience maximum and minimum pressure, to ensure balance in the runner during operation. The turbine at Kvilldal has 30 runner blades at the inlet and 24 guide vanes. The arrangement results in six runner channels facing maximum pressure from the guide vane openings, and six channels facing minimum pressure. The difference in pressure results in a difference in the flow through the runner channels. The latter creates momentum varieties, which causes the runner structure to bend [9]. Figure 3.6 illustrates how six channels are placed

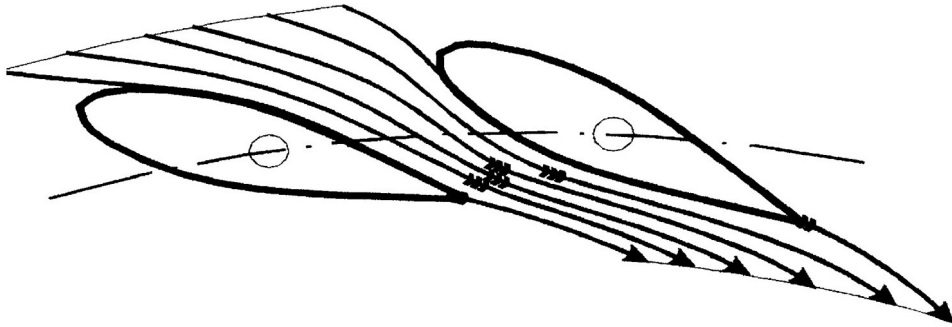


Figure 3.5: Stream lines between two guide vanes, redrawn from [3].

identically, relative to a guide vane.

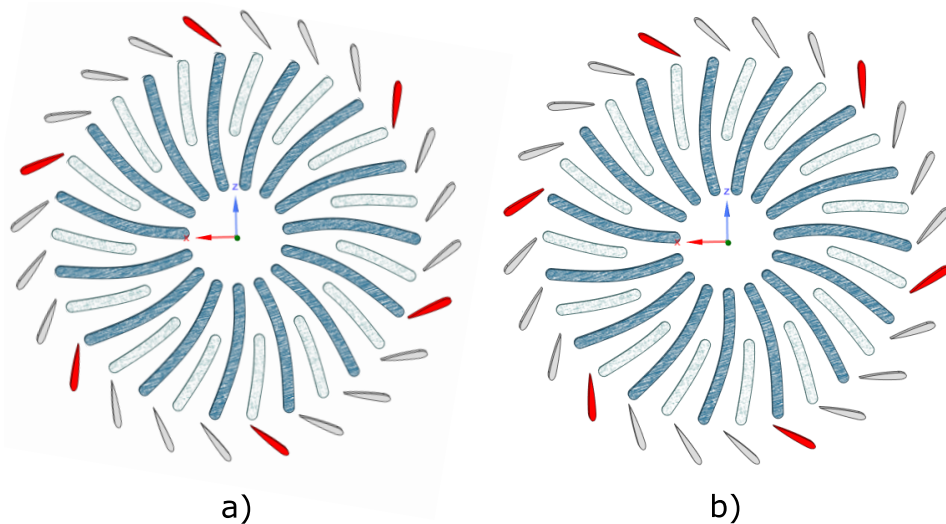


Figure 3.6: Sketch of how six channels in the runner at Kvilldal are facing an open guide vane channel. **a)** position 1. **b)** Rotated to the next channel.

Note that the vibrations in turbine 3 at Kvilldal happened during high load. When the load increases the distance in the vaneless space decreases, and the forces acting on the runner increases. RSI effects are expected to increase with the load [32]. If a runner bends due to RSI, the maximum dynamic stress is likely to occur in the center on the trailing edge of a main-blade. Figure 3.7 illustrates such stresses which are reliant on the structural rigidity of the blade, crown, and band. Static Von Mises stresses are awaited to change over the trailing edge as concluded by Huang et al. in 2014 [22]. During mid to high load operation, Huang et al. experienced static stresses close to the runner band at the outlet.

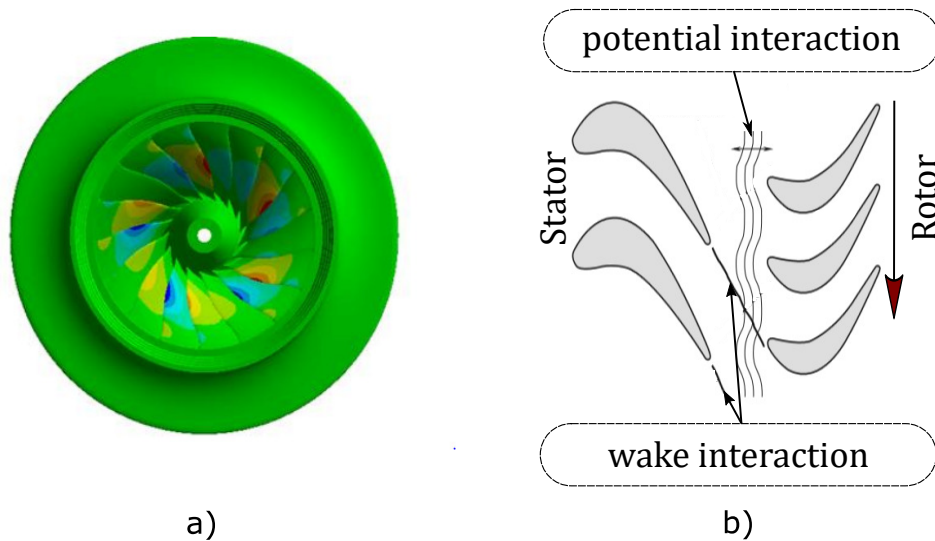


Figure 3.7: **a)** Dynamic stress on high head Francis runner with $Z_B = 17$, $Z_{gv} = 28$, $m = 2$, $n = 1$ results in $ND = 6$ [22]. **b)** Illustration of rotor stator interaction

RSI Theory

RSI is often represented as the combination of two flow distorting phenomena illustrated in figure 3.7. The two combining modes are caused by runner interaction and wake interaction. The first is rotating flow perturbations originating from the runner, while the second is flow perturbations generated by the wakes behind the guide vanes. The phenomena lead to two kinds of pressure fluctuations [50] [39].

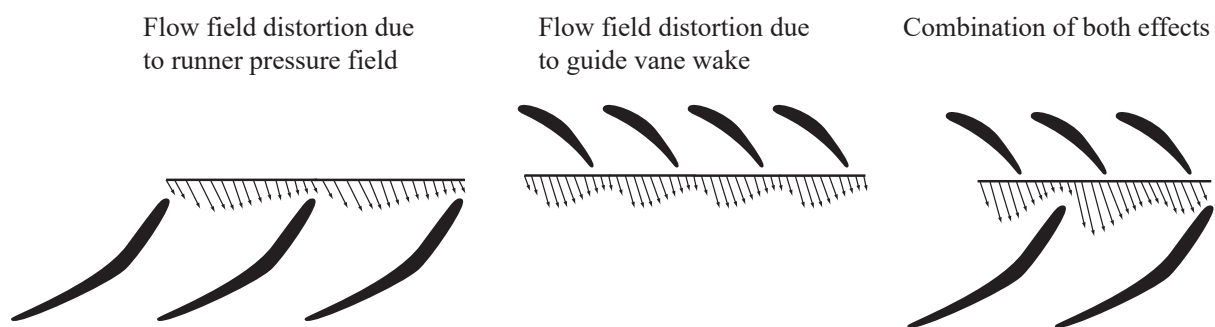


Figure 3.8: RSI modes [39]

- The first pressure phenomenon is a rotating diametrical pressure mode in the vaneless space. The mode may cause resonance between the rotating pressure field and the structure of the runner or the head cover. Resonance may lead to strong vibrations and noise, which can result in fatigue.
- The second pressure phenomenon is standing or traveling waves in the spiral casing known as phase resonance. The event may cause resonance with the structure of the pow-

erhouse leading to vibrations and noise. The standing waves can also cause transients in the penstock, which the fieldwork at Kvittdal investigates [39].

The frequencies related to the two fundamental pressure modes in figure 3.8 are known as the blade passing frequency and the guide vane passing frequency [50]. The blade passing frequency is observed in a static frame of reference and described by equation 3.1. f_{Bs} is the blade passing frequency in a static frame of reference, Z_B is the number of runner blades at the runner inlet, and n is the rotational frequency of the runner.

$$f_{Bs} = nZ_B \quad (3.1)$$

Equation 3.2 describes the pressure field related to a static frame of reference. N is the harmonic order, B_N and ϕ_N is the amplitude and phase for the N^{th} harmonic, θ_s is the angle coordinate in the stationary frame of reference. Z_{gv} is the number of guide vanes.

$$P_s(\theta_s, t) = \sum_{N=1}^{\infty} B_N \cos(NZ_{gv}\theta_s + \phi_N) \quad (3.2)$$

The guide vane passing frequency, f_{gvr} , is described by equation 3.3 which is observed in a rotating frame of reference.

$$f_{gvr} = nZ_{gv} \quad (3.3)$$

Equation 3.4 describes pressure field related to a rotating frame of reference. M is the harmonic order, B_M and ϕ_M is the amplitude and phase for the M^{th} harmonic, θ_r is the angle coordinate in the rotating frame of reference.

$$P_r(\theta_r, t) = \sum_{M=1}^{\infty} B_M \cos(MZ_B\theta_r + \phi_M) \quad (3.4)$$

The combination of the fundamental modes is illustrated figure 3.8 and described by equation 3.6. First the relationship in equation 3.5 is applied to obtain the solution for a stationary frame of reference [53].

$$\theta_r = \theta_s - \omega t \quad (3.5)$$

$$\begin{aligned} P_{MN}(\theta_s, t) = & \frac{A_{MN}}{2} \cos(MZ_B\omega t - (MZ_B - NZ_{gv})\theta_s + \phi_N - \phi_M) \\ & + \frac{A_{MN}}{2} \cos(MZ_B\omega t - (MZ_B + NZ_{gv})\theta_s + \phi_N - \phi_M) \end{aligned} \quad (3.6)$$

Inserting the turbine data from Kvittdal into Equation 3.6, with $M=N=1$ and zero phase change, yields the plots displayed in Figure 3.9. The pressure distribution clearly indicates 6 points where the runner is experiencing high pressure as discussed earlier in this section.

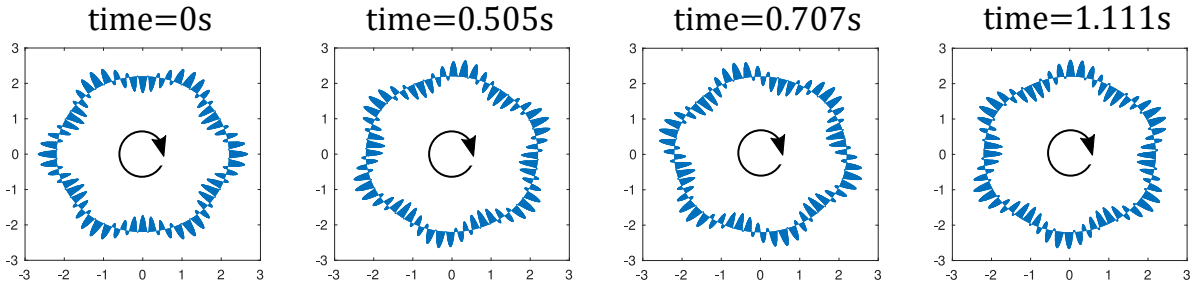


Figure 3.9: Modeled RSI pressure distribution with data from Kvittdal. $k=6$ which implies that the field rotates in the clockwise direction.

Equation 3.7 describes the diametrical mode k , which indicates how the pressure field is behaving in a stationary frame of reference. $k > 1$ means that the pressure field rotates in the same direction as the impeller while $k < 1$ states the opposite. Low k -values are of interest, as they are associated with the highest pressure amplitudes [45]. Pressure fields generating standing waves in the spiral casing are therefore expected to have low k values.

$$k = MZ_r \pm NZ_{gv} \quad (3.7)$$

Applying Equation 3.7 to the case illustrated in Figure 3.9 yields $k = 6$. This is the first harmonic ND=6.

other viscous effects: RSI is a phenomenon related to how the flow runs through the runner. Therefore, viscous effects are essential to have in mind when investigating RSI. The wake effect mentioned, but other effects are also significant. Non-uniform velocity field in the spiral casing, undesirable flow angle in the distributor and flow separation are all effects from viscosity that might contribute to the excitation of structural natural frequencies [50].

3.2.2 Draft Tube Vortex Rope

In Francis turbines, a vortex rope may form in the draft tube given the right circumstances. The discharge is the main governing factor, and different loads may generate a variety of vortex ropes. Dörfler et al. [9] present the following vortices, starting with the one related to the lowest load: Random pulsations, forced oscillations (half load surge), two threads (twin vortex), upper partial-load vortex (the 80% pulsation), and self-excited oscillation at high load (full-load surge). The swirl ratio, radial velocity distribution, and cavitation number σ play essential roles in the creation of the vortices. This subsection mainly focuses on the forced oscillations occurring at half load since they are dominating in the field measurements carried out at Kvittdal power plant.

The half load surge typically occurs in modern Francis turbines around 0.5 – 0.85% of best flow efficiency. The phenomenon was first investigated by Rheingans, who pointed to the problem with generator resonance [38]. The precession frequency of the corkscrew vortex is expected

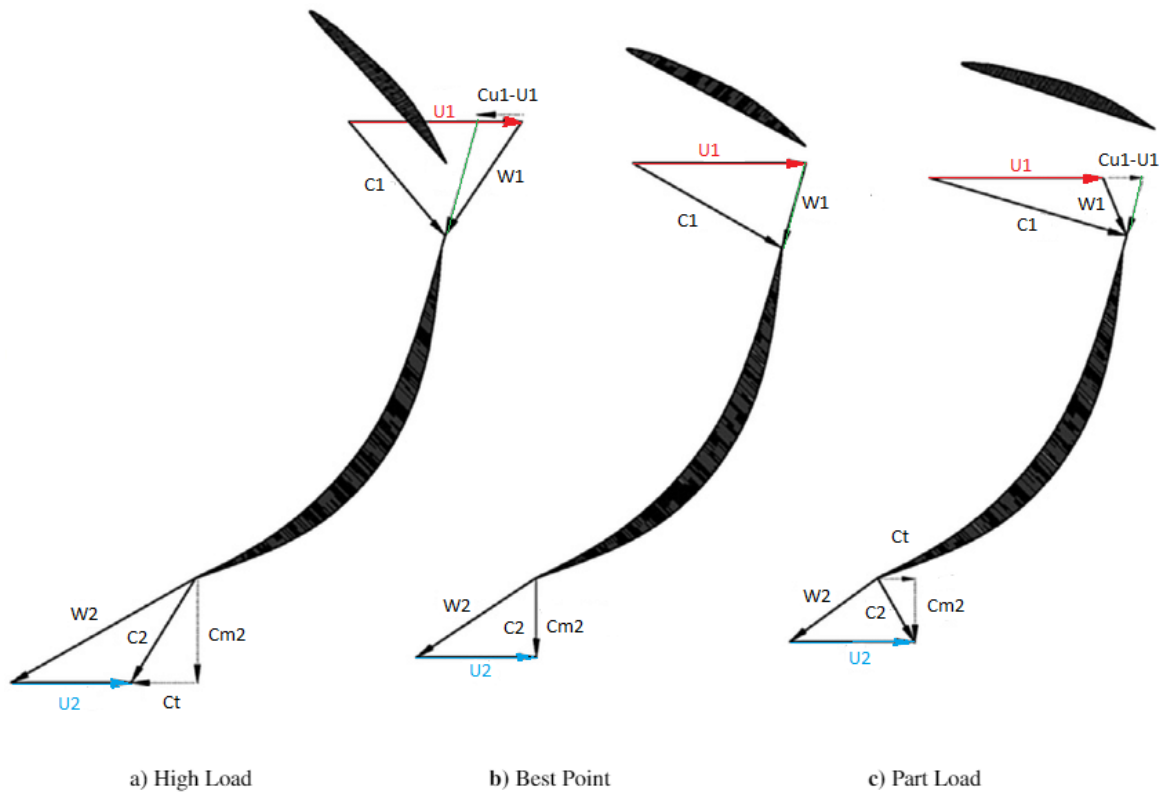


Figure 3.10: Velocity diagram of a Francis turbine at different operating points. Redrawn from [13]

to be in the same range as lower harmonics of the penstocks at Kvittdal, which might cause resonance condition in the waterways.

Figure 3.10 shows how the velocity diagram of a Francis turbine alters with different guide vane openings. At part load, the rotational velocity component c_t at the exit of the runner blade has the same direction as the runner, resulting in a low-pressure region in the center of the runner's exit area. Backflow in the axial direction occurs as a result of the pressure difference, forming a vortex rope. Any asymmetrical behavior in the backflow causes the vortex rope to transform into a helical vortex in the draft tube, figure 3.11 illustrates a vortex rope created in a Francis model during part load. This type of Vortex rope generates a diametrical pressure pulse rotating with the vortex. An axial pressure component due to the asymmetry of the vortex is also present. Surges in medium to large power plants related to this type of vortex are in the magnitude of 1 Hz [9].

The upper partial load vortex forms as higher frequency phenomena accompany the partial load corkscrew. Most observations in the past relate to machines with high specific speeds. The machines at Kvittdal has a medium speed number. If the vortices are present, the frequency spectrum is expected to show several narrow bands, where the center frequency differs with multiples of the precession frequency. The origin of the higher frequency component occurs when the vortex rope cross section gets stretched into an elliptical shape and rotates around

itself. The frequency related to this rotation is empirically found to be between 1-5 times the precession frequency [33] [40].

For high load conditions, the tangential velocity component is in the opposite direction of the runner rotation, as seen in the high load case in figure 3.10. When the tangential velocity gets sufficiently large a cavitated vortex emerges in the center of the draft tube [25]. The phenomenon seldom creates pressure fluctuations in the axial direction. Nevertheless, example cases of self-excited pressure and power pulsations during high load exists. Admission of small amounts of air into the draft tube can prevent these self-excited pulsations [9]. As mentioned in chapter 2, turbine 3 at Kvittdal experienced vibrations during high loads, until the modification of the air entrainment system in year 2000 [16].

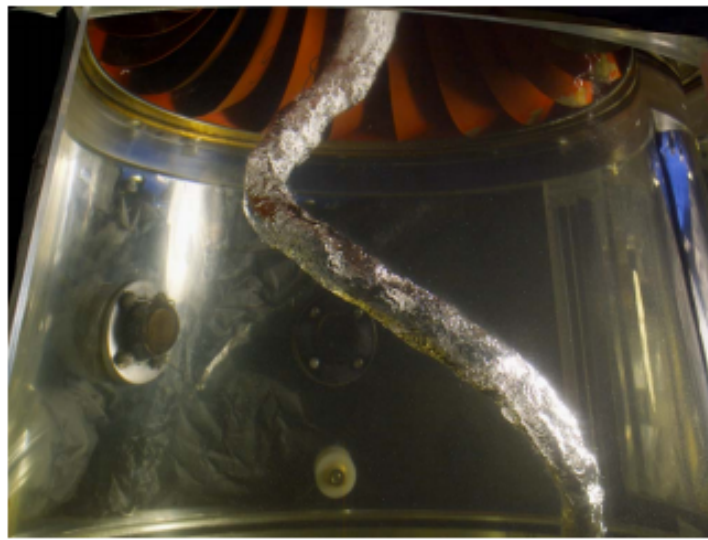


Figure 3.11: Draft tube vortex rope during part load. Taken from [9].

Draft Tube Vortex Theory

Equation 3.8 describes the half load surge as first empirically observed by Rheingans in [38] where n is the runner rotational frequency. The part load frequency is often referred to as the Rheingans frequency.

$$f_{Rhein} = \frac{n}{3.6} \quad (3.8)$$

For engineering purposes equation 3.9 can be used.

$$f_{Rhein} = \mu n \quad (3.9)$$

Wu et al. state $\mu \in [0.25, 0.34]$ in [50]. Dörfler et al. recommended $\mu \in [0.2, 0.4]$ in [9], but address that $\mu > 0.3$ is less likely.

The upper partial load vortex frequency can be described by equation 3.10 where $y \in [1, 5]$

$$f_{upv} = y f_{Rhein} \quad (3.10)$$

3.2.3 Von Karman Vortex Rope

The Von Karman Vortex street is a flow phenomenon that occurs as unsteady separation takes place when the flow interacts with a sufficiently bluff body. In Francis turbines, these vortices occur at several locations, such as downstream the wicket gate and in the runner. To initiate the shedding a minimum Reynolds number is required, for a circular cylinder a typical range where shedding is present is about $47 < Re < 10^7$ [50] [29].

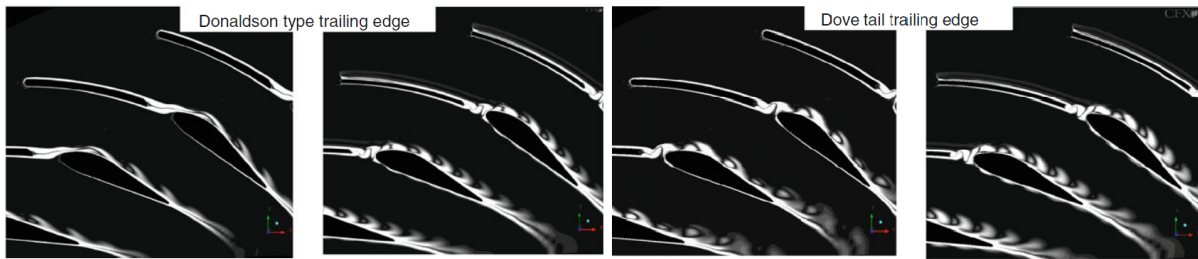


Figure 3.12: Von Karman vortices behind stay vanes and guide vanes [9].

The vortex rope originating from the trailing edge of the guide vanes, stay vanes, and the runner results in pressure disturbances. Classical wake theory can be used in the turbine as concluded by Antonsen in 2007 [1]. As mentioned earlier, the space between the wicket gate and the runner at Kvittdal is not the same for all the turbines. Antonsen [1] refers to Jernsletten 1995 [24] who concludes that the vaneless space in a Francis turbine is a sensitive area. By increasing the distance between wicket gate and runner in a model Francis turbine with 5.1 mm Jernsletten [24] observed that pressure pulses decreased with 30%.

For low head Francis and Kaplan turbines, the frequencies related to the shedding downstream the wicket gate can directly generate structural vibration if the vortices interact with the tip of the runner blades and excite the natural frequency of the runner blade [50]. This is not a concern in high head Francis machines.

Theory

The frequencies related to vortices, f_k , in a turbine can be estimated with Equation 3.11 [50]. The frequency is a function of the Strouhal number, St , the velocity at the separation point, W , the virtual boundary layer thickness, δ_v , and the blade thickness δ_2 .

$$f_k = St \frac{W}{\delta_2 + \delta_v} \quad (3.11)$$

The Strouhal number generally has values between 0.18 and 0.25 [50]. Early studies by CA. Gøngwer in 1952 [17] concluded that $St = 0.19$ was most appropriate.

In 1960 Heskestad and Olberts [20] did experiments on several geometries which resulted in Equation 3.12. In the experiments the Strouhal number was measured to be $St = 0.18$.

$$f_k = 0.01St \frac{BV_0}{\delta_2 + \delta_v} \quad (3.12)$$

V_0 is in this case the mean velocity of the stream outside the wake. B is a relative frequency which alters with the shape of the trailing edge. Tables with values of B can be found in [20].

The virtual boundary layer thickness can be obtained by empirical formulas found in literature such as [50]. Equation 3.13 yields the virtual boundary layer thickness on a runner blade with circular trailing edge.

$$\delta_v = 0.0294 \frac{x}{Re_x^{1/5}} \quad (3.13)$$

Re_x is the Reynolds number related to the blade length, x .

Stationary Blades

In the design process of stay vanes and guide vanes, it is vital to make sure that the shedding frequency does not match the natural frequencies of the structure. The main challenge is to obtain an excellent empirical method for calculating the Strouhal number since the Reynolds number in the model and prototype scale are very different.

A study performed by Vu et al. [48] conclude that CFD can be used to predict the shedding frequencies, but the prediction is not exact. The study obtained CFD calculations of the shedding frequencies within 18% of the actual frequencies, while Antonsen concluded that his simulations were within 15% of the actual frequencies [1]. Vu et al. state that structural design should ensure that structural frequencies are at least 20% away from the predicted frequencies [48].

Rotating Blades

Under the right conditions, vortex shedding also occurs on rotating blades. For a Francis turbine, the shedding occurs at the trailing edge of the runner at part load. Shedding takes place on the suction side of the blade, as the inflow has a high angle of attack. Figure 3.10 illustrates the event. Shedding may also originate from the leading edge of the blades in a Francis runner. Inter-blade vortices occur when the flow angle at the inlet is no longer properly aligned with the blade inlet angle. High incidence on the blade leads to a vortex, running from the inlet towards the outlet [9].

$$f_k = k_1 \frac{W_2}{\delta_2} \quad (3.14)$$

Equation 3.14 generally holds for Reynolds numbers in the range $250 < Re < 2 \cdot 10^5$. k_1 is an empirical constant determined by the shape of the trailing edge [50]. The Reynolds and Strouhal numbers are defined by the following relations:

$$Re = \frac{\rho W_2 \delta_2}{\mu} \quad St = \frac{f_k \delta_2}{W_2} \quad (3.15)$$

The value of W_2 in a Francis turbine increases from crown to band. A consequence of this is that the values of f_k vary through the runner [50]. A vortex originating close to the inlet of the runner with a frequency unequal to the natural frequency of the runner may increase as the velocity increases. If the frequency evolves and matches the natural frequency of the structure, the lock-in phenomenon described by Dörfler et al. in [9] occurs.

The shape and roughness of the blades and trailing edge are essential factors that govern how the vortex shedding develops. This causes challenges when we try to understand prototype behavior using model scale simulations [45].

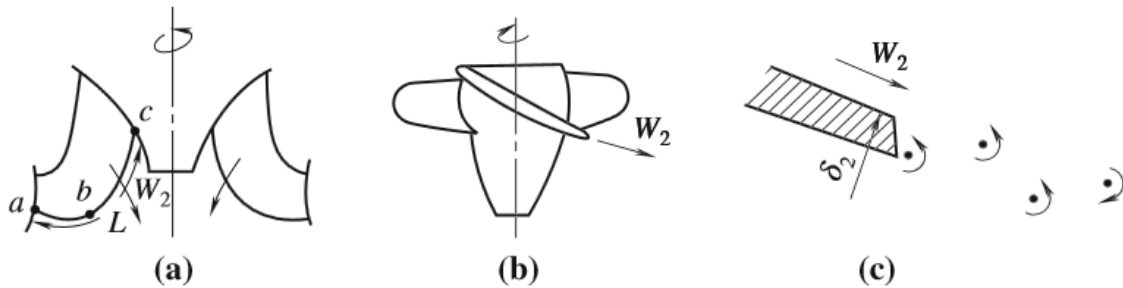


Figure 3.13: **a)** Francis turbine blade. **b)** Kaplan turbine blade. **c)** vortex street behind the blade. [50]

3.2.4 Turbulence And Cavitation

Turbulence and cavitation play essential roles in the flow regime in a hydropower plant.

One effect of turbulence is that it mixes the flow, smearing out differences in the stream [51]. The latter is apparent when we compare RSI effects in high head Francis turbines with low head Francis turbines. The increased distance between the guide vanes and the runner blades on the low head machines increases turbulent mixing in this region, which results in a smoother pressure distribution, which again dampens the RSI effect.

Cavitation as a phenomenon happens when water transfers between liquid and gas state, which is a consequence of pressure differences in the flow. Previous sections in this chapter present

and discuss sources of pressure differences. Cavitation results in noise when gas bubbles burst. The event may deteriorate the turbine structure if it happens close to solid surfaces [9].

Dörfler et al. also addresses that vibrations arising from cavitating effects may travel throughout the system [9]. Since the frequencies related to cavitation are of a wide range, they may excite natural frequencies of many components. The pressure pulses created by the cavitating vortex rope has been measured far upstream in the penstock in several cases [50] [9] [10].

3.2.5 Summary of the Frequencies Related to Flow Features

Table 3.1 is taken from [9] and contains the frequencies related to flow features discussed in the previous subsections.

Exiter	Draft tube vortex	Runner unbalance	Runner passage	Guide vane passage	Stay vanes Karman	Guide vane Karman	Runner blade Karman
<i>Frequency</i>	$0.2n - 5n$	n	nZ_B	nZ_{gv}	$St \frac{W}{\delta_2 + \delta_v}$	$St \frac{W}{\delta_2 + \delta_v}$	$St \frac{W_2}{\delta_2}$
<i>Waterconduit</i>	X						
<i>Shaftbending</i>		X					
<i>Generator</i>	X						
<i>Stayvanes</i>			X		X		
<i>Guidevanes</i>			X			X	
<i>Runner</i>				X			X

Table 3.1: Main resonance conditions in a Francis turbine, recreated from [9].

3.3 Fatigue and Structural Natural Frequencies

3.3.1 Fatigue in metals

Fatigue in metal structures is widely studied and thoroughly described in literature such as [7] [27]. The interaction between the fluid and the structure in a hydropower plant results in stress induced on the structure by the fluid. The number of times a material can withstand stress with a given amplitude before it fails was first described by Wöhler in the mid-1800s. The classical representation is the SN-diagram seen in Figure 3.14. Wöhler's work intended to predict the fatigue life of metals in industrial applications, mainly rail-car axles and steam engines. The number of cycles these machines were subjected to was relatively low, resulting in the fatigue limit in terms of number of cycles to be between 10^6 and 10^7 [6].

The SN curve or fatigue curve, such as the one drawn in figure 3.14, is usually concerning carbon steel. The curve is typically limited to 10^7 cycles, and it is common to draw a horizontal line between 10^6 and 10^7 , which determines the fatigue limit. For carbon steel alloys the standard assumes that the fatigue life is infinite beyond 10^7 cycles. Since many modern applications such as high-speed rail cars, airplane jet engines and hydro turbines experience more than 10^9

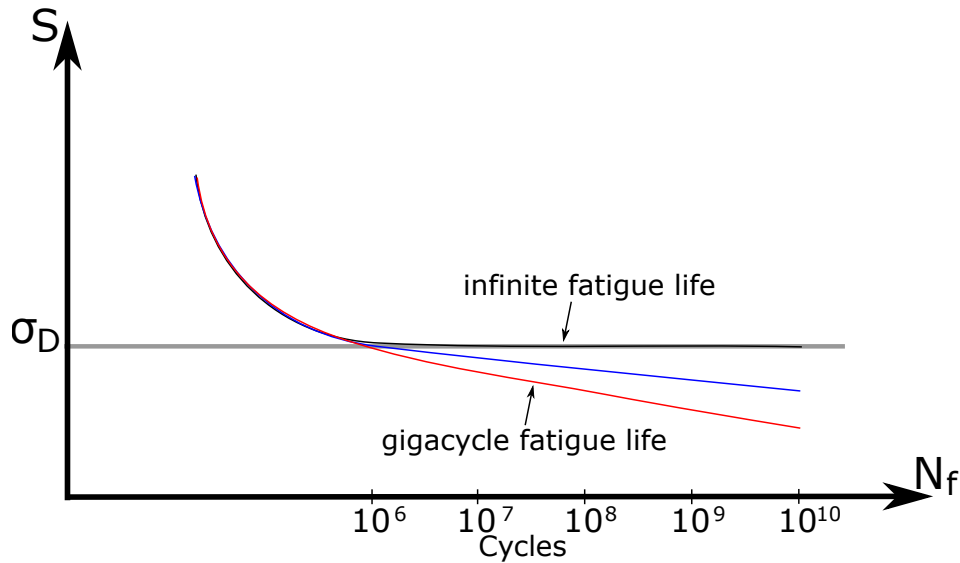


Figure 3.14: SN curve, S is the stress amplitude, N_f is the number of cycles. Redrawn from [6]

cycles, additional techniques are taken into consideration resulting in the gigacycle fatigue life curve seen in figure 3.14 [6].

For turbines in a hydropower plant, it is vital that, over the lifetime of the turbines, the accumulated load cycles remain below the SN-curve. If pressure pulsations generated by the turbine causes resonance in any part of the power plant, increased stresses results in a lower number of cycles before fatigue failure. This statement is one of the primary motivations for this thesis.

Liu et al. and Zhang et al. presents reviews of fatigue damage in hydro turbines and turbomachinery in [28] and [52]. Both articles conclude that fatigue is the primary failure mode. Cracks from fatigue on high head Francis runners often occur on the trailing edge or leading edge of the impeller blades. These areas experience the highest stresses [50]. The statement matches the history of turbine 3 at Kvittdal.

3.3.2 Structural Natural Frequencies

Mechanical movement such as a turbine spinning or pressure fluctuations induced by flow features in a turbine causes vibration in the surrounding structure, i.e., the turbine or pipes. If the vibrations match a natural frequency of the structure, the consequences might be severe, resulting in fatigue failure.

The natural frequencies of a runner are challenging to predict since it is dependent on several factors. However, the first natural frequency usually occurs between 70 – 300 Hz [45]. Vibrations in this range are therefore essential to avoid. Factors influencing the runner's natural frequency are listed below as described by Trivedi and Cervantes in [45].

- The structure of the runner has a natural frequency in air, which can be measured.

- Added mass effect in water reduces the natural frequency with up to 60%. Studies suggesting this do, however, not include the effect of the surrounding structure, flowing water, and cavitation.
- The rotating structure generates acoustic waves that interact with the surroundings and additional natural frequencies in the runner are expected to appear.
- Transient operating conditions alters the structural behavior of the runner.

Resonance frequencies in the pipe structure are dependent on the diameter, thickness, and material of the pipe. Generally, the first natural frequency is expected to be higher than the pressure fluctuations generated by a turbine, and the pressure fluctuations in the pipe system [35] [12]. Standing pressure waves are a concern in the pipe system since they increase the pressure fluctuations in certain regions. Figure 3.15 illustrates a standing wave and how it increases the stress in some areas of the pipe. As an example, a standing wave with a frequency of 5 Hz produces 1800 cycles each hour and might lead to fatigue failure even with a relatively low wave load amplitude [36].

3.4 Transients and Resonance in Waterways

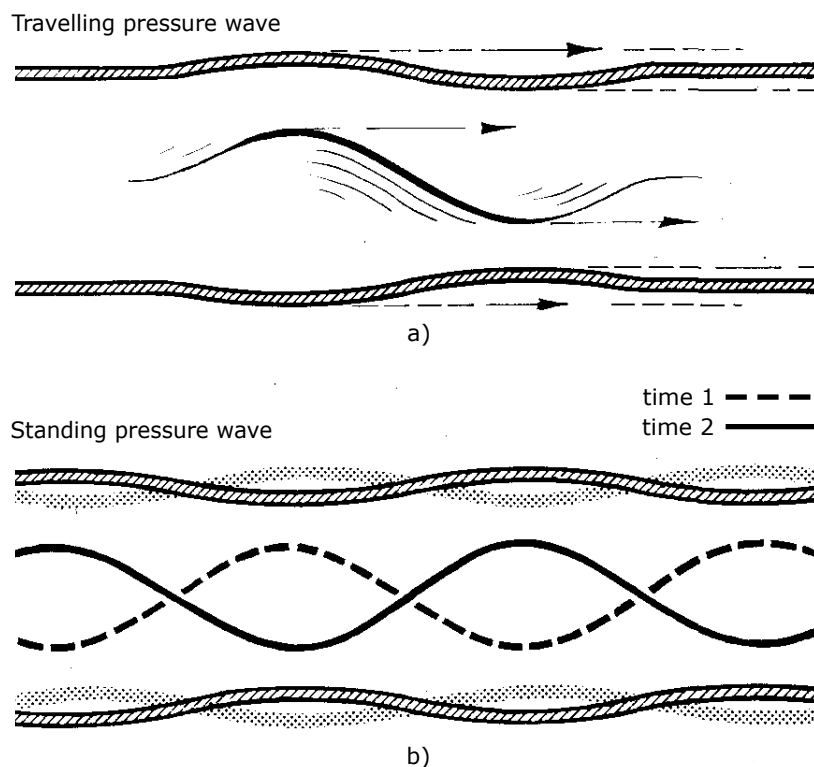


Figure 3.15: Traveling and standing pressure wave. Taken from [36]

The water-hammer effect describes how transients develop in a system and arise as water flowing in a completely filled tunnel, or pipe is disturbed. The phenomenon can be visualized with the following scenario. A large upstream water reservoir with constant head supplies a

fully developed pipe flow with a valve downstream. The valve is then closed completely, instantaneously leading to pressure and flow fluctuations propagating between the reservoir and the valve, which are reflection points. Thorough derivation of the water-hammer effect can be found in [11] and [4]. An important result from the case described above is the fundamental time, T_f , which is described by equation 3.16. The fundamental time of a pipe is dependent on the length, L , and the wave speed, a . The fundamental time of a system of pipes connected in series is obtained by adding the individual times together [23].

$$T_f = \frac{4L}{a} \quad (3.16)$$

The fundamental frequency, f_f , of a system is given by equation 3.17. This frequency can be excited by cyclic pressure fluctuations, which leads to resonance. The governing parameters are the length of the waterways and the propagation velocity. The propagation velocity and how it can be detected is discussed in the following subsection.

$$f_f = \frac{1}{T_f} \quad (3.17)$$

The main reflection points at Kvilldal power plant are the junctions where the penstocks are connected, the blind tunnel, the turbines, and the air cushion chamber. The points are illustrated in Figure 4.1. Closing a bulb valve moves the reflection point from the turbine to the valve, which also is a stronger reflection point. As mentioned in the introduction, the experiments at Kvilldal includes different closed valve configurations. The effect of altering reflection points and other transient governing factors are investigated with the numerical model and observed in the experimental results.

Resonance condition implies that disturbances in the system amplify with time and are associated with pressure and flow fluctuations [4]. An exciter of the disturbances with enough energy and a frequency matching an odd harmonic of the fundamental frequency of the waterway causes resonance [23]. Exciters with high frequencies are unlikely to cause resonance in long waterways where the pressure is high [43]. The results from measurements in this thesis strengthen the conclusion.

3.4.1 The Propagation Velocity

The propagation velocity is the velocity that pressure waves have in a fluid. It is also often referred to as the speed of sound in the fluid. The flow in hydropower plants as Kvilldal is pressure flow where the pipes are filled with fluid. The propagation velocity in a homogeneous fluid can be expressed by Equation 3.18 as in [41].

$$a = \frac{\sqrt{K/\rho}}{\sqrt{1 + [(K/A)(\Delta A/\Delta p)]}} \quad (3.18)$$

a is the propagation velocity, K is the bulk modulus of elasticity of the fluid, ρ is the density of the fluid, A is the cross sectional area, ΔA is the change in cross sectional area, Δp is the change in pressure.

Equation 3.18 shows that the propagation velocity is dependent on both the fluid and the waterway structure. For rigid structures, the term $(\Delta A/\Delta p)$ becomes very small, and the structural factors are negligible. For elastic structures, such as thin-walled pipes, the propagation velocity also depends on the pipe material and how the attachment. More details on these effects are given in [11] [4] [46]. The propagation velocity in water at ordinary temperatures is approximately $\sqrt{K/\rho} = 1440\text{m/s}$, Wave speeds in large steel pipes may be around 1000m/s , while pressurized flow in small pipes vary between 1200m/s to 1400m/s [11].

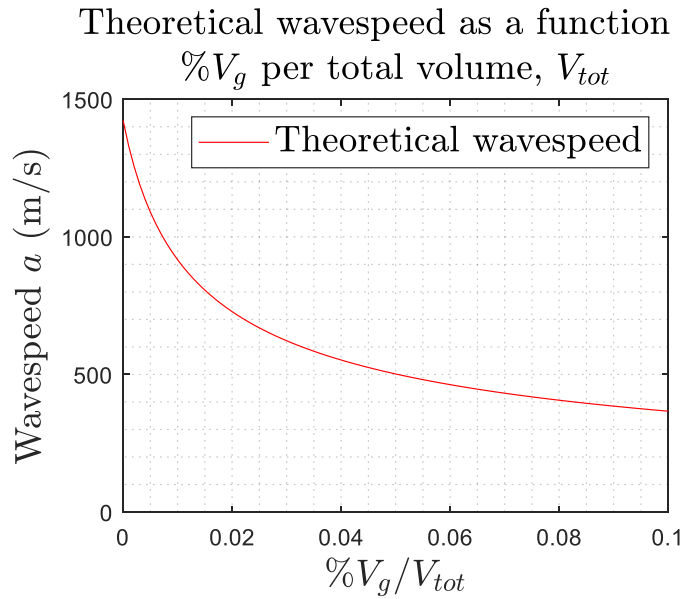


Figure 3.16: Propagation velocity in a mixture of water and air as a function of the volume percentage of air in the mix. Reconstructed from [11].

The examples of velocities given above are based on the assumption that the fluid is homogeneous, as discussed in [11] the velocity is highly sensitive to the presence of air. Figure 3.16 is recreated from [11] where the case is validated against experimental results. The propagation velocity is expressed as $a = \sqrt{K_{mix}/\rho_{mix}}$ where K_{mix} is an expression for the bulk modulus of elasticity for the mixture of water and air. ρ_{mix} is also a function of the density of water and air and the volume percentage of each. Subscript *liq*, implies liquid while *g* implies gas. Note that the propagation velocity in the waterways at Kvilldal is less sensitive to air entrainment compared to the Hydropower laboratory at NTNU. The air molecules at Kvilldal are more compressed since the pressure is much higher.

$$K_{mix} = \frac{K_{liq}}{1 + (V_g/V_{tot})(K_{liq}/K_g - 1)} \quad (3.19)$$

$$\rho_{mix} = \rho_g \frac{V_g}{V_{tot}} + \rho_{liq} \frac{V_{liq}}{V_{tot}} \quad (3.20)$$

It is necessary to calculate each waterway section independently to predict the fundamental frequency of the waterways at Kvilldal. The reasons are altering cross-sections and differences in

material properties between tunnel sections [5]. The calculations are, however, tricky to conduct precisely since the propagation velocity is unknown in the different sections.

3.5 Seismic Interferometry

Seismic interferometry and deconvolution interferometry are post-processing techniques which have been applied to investigate the propagation velocity in the penstock at Kvittdal and in the Hydropower Laboratory. The methods are based on comparing two measured signals treating one as a source and the other as the response to the source.

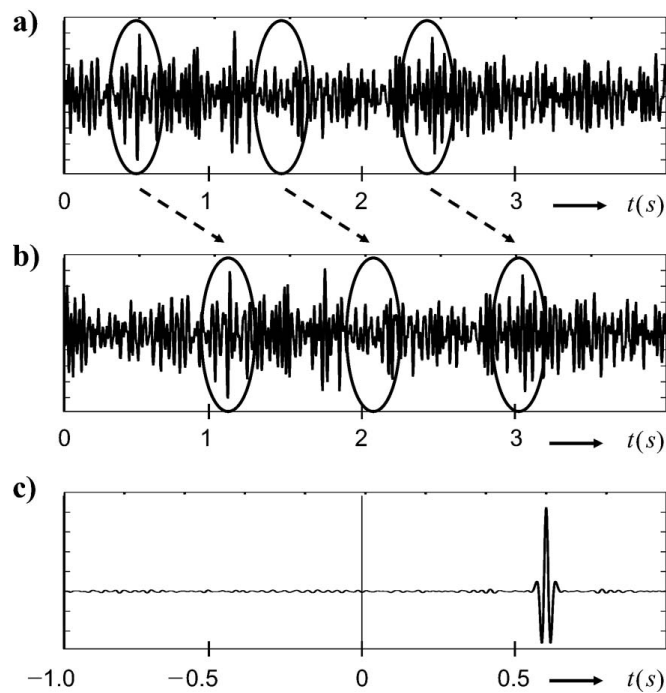


Figure 3.17: Seismic interferometry infinitely long pipe. Taken from [49]

Figure 3.17 shows the measured signal from a case where plane pressure waves generated by a source are traveling from left to right in an infinitely long pipe with a noise field. Figure 3.17 **a)** and **b)** illustrates measured pressure data from two locations where signal **a)** is closest to the source. Figure 3.17 **c)** is the result of cross-correlating signal **b)** with signal **a)** when signal **a)** is considered as the reference signal. The response in figure 3.17 **c)** unveils the time it takes for a plane pressure wave to travel between the two sensors. The propagation velocity is easy to calculate if the distance between the sensors is known. Note that the technique does not require that the distance to the actual source is known [49].

In a hydropower plant, the penstock is not infinitely long. A consequence is that the plane-waves generated by the turbine reflect. The response obtained by cross-correlating two signals in a penstock will, therefore, have two peaks. One peak is in the positive time domain and the other in the negative time domain since plane-waves are traveling both directions. Figure 3.18 **c)** displays such an example.

The two post-processing techniques require that at least two pressure transducers, with known locations, are distributed in the lengthwise direction of the investigated pipe section. Seismic

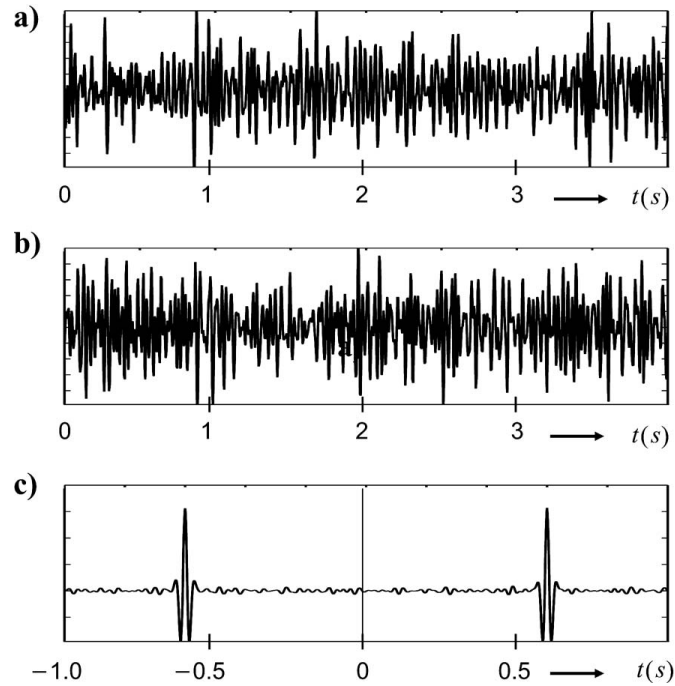


Figure 3.18: Seismic interferometry pipe with reflection. Taken from [49]

interferometry is also known as Greens function retrieval since the method is based on obtaining the Greens function between the two signals. Deconvolution interferometry is a modified version of seismic interferometry which can be used to gain better results in cases where the excitation force creating disturbances is complex, e.g., a turbine [47]. Further description of the methods can be found in the paper available in Appendix F or [49] [8] [18].

One Dimensional Numerical Models

Numerical models of the waterways at Kvittdal and the Hydropower Laboratory were developed to investigate system parameters, which govern transients. The models also provided the possibility to compare measurements with a known controllable system.

4.1 Kvittdal

A one dimensional model of the waterways at Kvittdal has been developed to investigate the effects of different parameters governing the flow in the complicated pipe system. Figure 4.1 illustrates the pipe system consisting of 13 pipe sections, 4 junctions, 4 turbines, a blind tunnel, and an upper reservoir. The theory and assumptions needed to create and implement the model are presented later in this chapter.

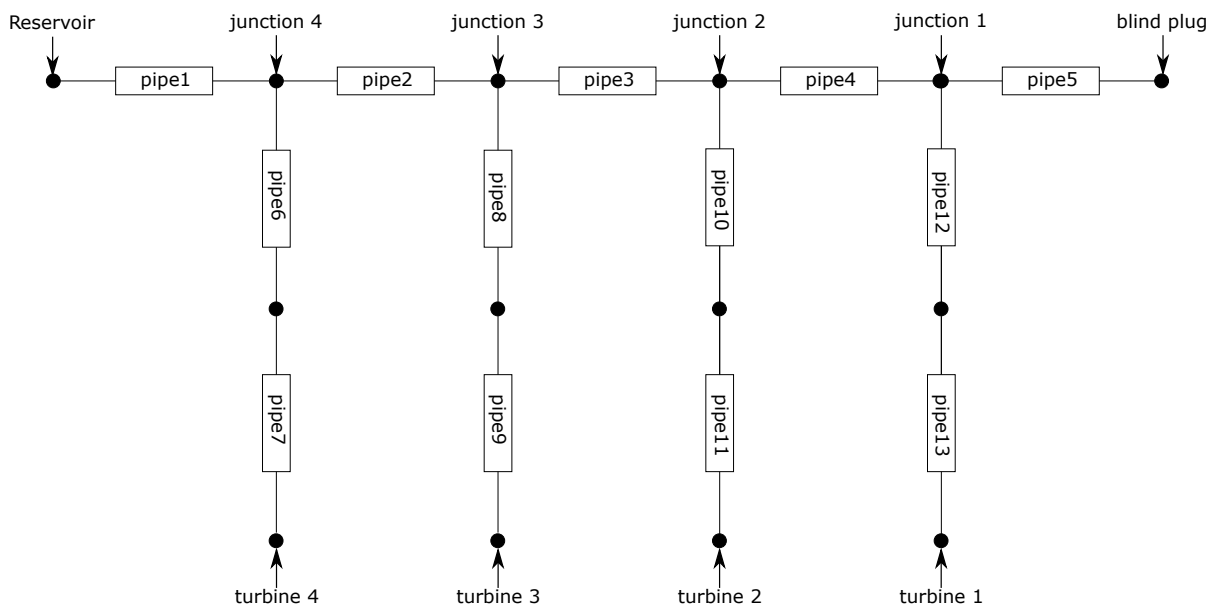


Figure 4.1: Elements in model used to simulate Kvittdal.

Low frequencies are the main focus in the spectral analysis of the simulated data. Mathematical models describing the waterways response to high-frequency phenomena are unlikely to be accurate since the relative uncertainty of the wavelengths is in the same order of magnitude as the uncertainty of the wave speed. The basic theory chapter describes why the propagation velocity is uncertain, as it alters between tunnels and pipe sections. Low-frequency phenomena, such as draft tube surges, have wavelengths in the same order of magnitude as the penstock or even shorter. The dynamic response of the system to these frequencies is, therefore, more likely to be accurate [9]. The friction and reflection points are also challenging to predict in the rock bored tunnels where geometrical discontinuities are present, and the exact lengths of the tunnels are questionable. Reflection points related to geometrical features in branch junctions and series junctions are also challenging to model precisely. The numerical model is, therefore intended as a tool to investigate trends and not represent any specific events.

4.2 Hydropower Laboratory

Figure 4.2 illustrates the one dimensional model of the hydropower Laboratory, together with a two-dimensional drawing of the investigated part of the Francis rig at the Hydropower Laboratory. The model consists of two pipe sections representing the penstock, a constant head reservoir upstream. A valve downstream excites pressure fluctuations in the penstock. Two pipe sections make it possible to have two cross-sections and implement a reflection point for transients where the flow meter is located.

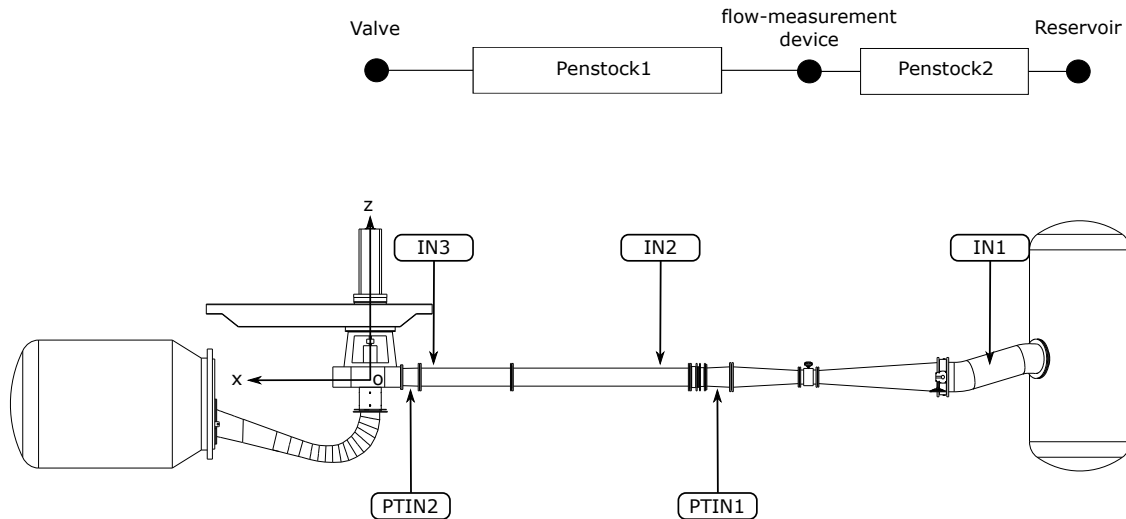


Figure 4.2: Simulation elements used to simulate the Hydropower Laboratory together with a 2D drawing of the Francis rig in the hydropower laboratory.

The model was mainly used to produce reference data to compare with the measured data while investigating seismic interferometry as a post-processing technique. The pressure was recorded and stored from five points in the modeled penstock to recreate the actual experimental setup illustrated in figure 4.2.

4.3 Theory

4.3.1 Fundamental Equations Transient Pipe Flow

The two fundamental equations governing transient pipe flow in the axial direction are the continuity and momentum equation. Long pipes can be treated as one dimensional since the forces acting in the lengthwise direction exceed the radial forces by far [34] [4].

$$V \frac{\partial H}{\partial x} + \frac{\partial H}{\partial t} + \frac{a^2}{g} \frac{\partial V}{\partial x} = 0 \quad (4.1)$$

$$g \frac{\partial H}{\partial x} + V \frac{\partial V}{\partial x} + \frac{\partial V}{\partial t} + \frac{fV|V|}{2D} = 0 \quad (4.2)$$

Equation 4.1 and equation 4.2 describe continuity and momentum balance in a one dimensional pipe. The pressure head H and flow velocity V are dependent variables, while the position and time variables x and t are independent. The other terms in the equations are g = gravitational constant, a = pressure propagation velocity, D = pipe diameter and f = friction coefficient. The equations are quasi-linear, hyperbolic partial differential equations. They can not be solved directly. One solution is to apply the characteristics method.

4.3.2 Characteristics Method and Finite Differences

The characteristics method solves the fundamental equations by transforming them into a set of linear ordinary differential equations. The transformation involves no simplifications so that the solution of the characteristics C^+ and C^- are exact [11]. The method requires known pressure and flow conditions at all locations in the pipe system, at each time step before it continues to the next.

$$C^+ \begin{cases} +\frac{g}{a} \frac{dH}{dt} + \frac{dV}{dt} + \frac{fV|V|}{2D} = 0 & (4.3) \\ \frac{dx}{dt} = +a & (4.4) \end{cases}$$

$$C^- \begin{cases} -\frac{g}{a} \frac{dH}{dt} + \frac{dV}{dt} + \frac{fV|V|}{2D} = 0 & (4.5) \\ \frac{dx}{dt} = -a & (4.6) \end{cases}$$

Equation set C^+ and C^- can be solved using finite differences. Figure 4.3 illustrates the calculation domain related to a pipe section. A, B, and P are points for calculation and storing of pressure and flow. H_P is the pressure at point P etc. The characteristics method is applied as listed below.

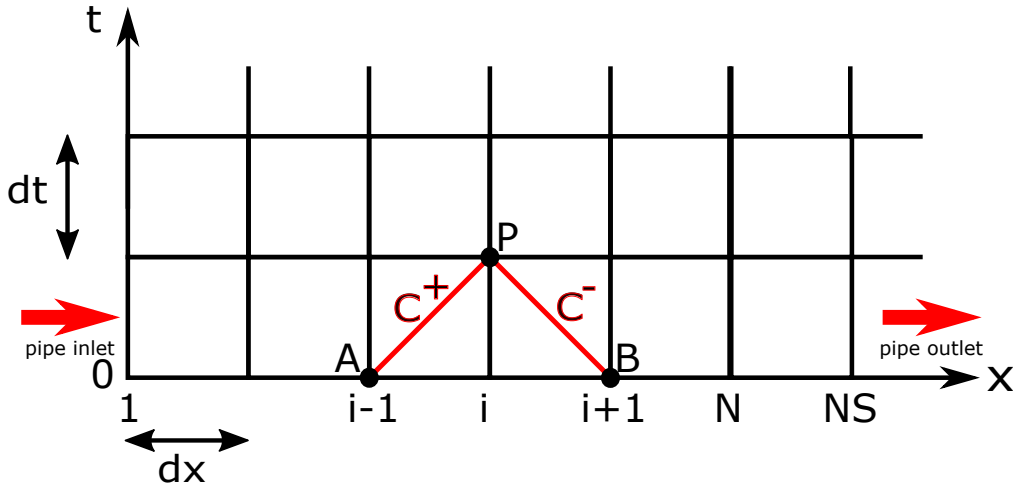


Figure 4.3: Method of Characteristics computational domain.

1. Pipe constants are set. a = wave speed, g = gravitational constant, L = length, D = diameter, f = friction coefficient.
2. The pipe is divided into N sections with thickness dx in the lengthwise direction. Resulting in $N + 1$ points to calculate.
3. Time increment dt is set. **NOTE:** Courant condition should be obtained, $C_r = a(dt/dx) \leq 1$ [15].
4. For $dx/dt > 0$, equation 4.4 is satisfied on the line between points **A** and **P**. H_A and V_A are known at **A**. Equation 4.3 can be integrated between **A** and **P**. Values H_P and V_P at **P** are obtained. In similar fashion the values at point **P** are obtained with the values known at point **B** for $dx/dt < 0$ by applying equation 4.5 and 4.6.

The steps above allows equation set C^+ and C^- to be transformed into equations 4.7 and 4.8.

$$H_P - H_A + \frac{a(Q_P - Q_A)}{gA} + \frac{f\Delta x Q_A |Q_A|}{2gDA^2} = 0 \quad (4.7)$$

$$H_P - H_B + \frac{a(Q_P - Q_B)}{gA} - \frac{f\Delta x Q_B |Q_B|}{2gDA^2} = 0 \quad (4.8)$$

The following relations are common to introduce. B and R are constant through a pipe section with constant friction and diameter.

$$B = \frac{a}{gA} \quad R = \frac{f\Delta x}{2gDA^2} \quad (4.9)$$

Introducing the relations results in equation 4.10 and 4.11

$$C^+ : H_P = H_A - B(Q_P - Q_A) - RQ_A |Q_A| \quad (4.10)$$

$$C^- : H_P = H_B + B(Q_P - Q_B) + RQ_B|Q_B| \quad (4.11)$$

The equations must hold for steady flow i.e. $Q_A = Q_B = Q_P$ which means that $RQ_A|Q_A|$ is the steady friction term. Exponential friction can be implemented by changing the last term in the equations to $RQ_i|Q_i|^{n-1}$. In the numerical model of Kvilldal, CM and CP are introduced to ease the implementation. For a general internal point P_i the following equations are applied to obtain the Head, H_{P_i} , and flow, Q_{P_i} .

$$CP_i = H_{i-1} + BQ_{i-1} - RQ_{i-1}|Q_{i-1}| \quad (4.12)$$

$$CM_i = H_{i+1} - BQ_{i+1} + RQ_{i+1}|Q_{i+1}| \quad (4.13)$$

The characteristics

$$C^+ : H_{P_i} = CP - BQ_{P_i} \quad (4.14)$$

$$C^- : H_{P_i} = CM + BQ_{P_i} \quad (4.15)$$

By combining Equations 4.14 and 4.15, Q_{P_i} can be eliminated, a final Equation for H_{P_i} is obtained:

$$H_{P_i} = \frac{CP + CM}{2} \quad (4.16)$$

After obtaining H_{P_i} it is easy to calculate Q_{P_i} directly from either equation 4.14 or 4.15. The equations are applicable for all internal points, i.e. not node 1 and NS in the computational domain which are the boundary conditions.

As mentioned earlier, the calculations of the characteristic method by finite differences are dependent on knowing all values at a present time step before continuing to the next. It is, therefore, necessary to address initial conditions and boundary conditions.

4.3.3 Assumptions and Boundary Conditions

dx, dt and the wave speed a

Applying the method of characteristics on a fixed grid induces some challenges. Initial conditions include the wave speed and length of pipe sections. It is **crucial** that dt is the same in all pipe sections since the method depends on calculating a time step for the entire system before continuing to the next.

There are a couple of methods to adjust the variables, but for a rigid pipe system, the following method is recommended by [11]. The time is divided by the following relation for a system with j pipe sections where L_j is the length, N_j is the number of elements, and a is the propagation velocity.

$$dt = \frac{L_j}{aN_j} \quad (4.17)$$

For a system with a lot of sections it is unlikely that Equation 4.17 will hold for all the sections. Since N_j is an integer, L_j is known and a_j is approximated with some uncertainty it is advised to introduce a parameter, Ψ to soften a_j as described by equation 4.18.

$$dt = \frac{L_j}{a_j(1 + \Psi_j)N_j} \quad (4.18)$$

In the model of Kvilldal an iterative process is used in the initiation phase. By adjusting N_j and L_j together with ψ_j small changes to a_j is ensured. The process start with setting dx for all pipe sections which provides an initial N_j . The following steps are listed below.

1. dt is set to be the smallest of 1/5000 and the outcome of equation 4.17 when applied to all pipe sections. 1/5000 is chosen to produce a fft similar to the one in the measured data where the sampling rate is 5000 Hz.
2. a is set for each pipe section and the first estimation of dx_j is found with equation 4.4.
3. The number of elements in each section is found by rounding $N_j = L_j/dx_j$ to the closest integer i.e Nr_j . Multiplying Nr_j with dx_j may result in a larger or smaller pipe length.
4. If the difference between the new length and the original is larger then a set residual, a new a is calculated based on the old length and the new amount of sections N_j . Step 2 until 4 is repeated until the difference in length is smaller than the control factor.

Friction

The friction term used in the numerical model comes from the Darcy-Weisbach equation 4.19. Numerous friction models for pipe flow exist, all trying to describe the wall shear stress. Conventional friction models, such as the Darcy-Weisbach and Hazen-Williams formula are used in transient analysis. The models are based on the average velocity during steady state flow, assuming that the friction coefficient does not change during unsteady conditions. To improve accuracy in transient simulations a time-dependent friction term can be added [15] [11]. However, the goal of this thesis is to investigate the dynamics in the waterways at Kvilldal. Higher friction does not alter the frequency of peaks in the spectral analysis, but certain amplitudes decrease. Based on this goal, the Darcy-Weisbach friction model is assumed adequate.

$$\tau_0 = \frac{\rho f V |V|}{8} \quad (4.19)$$

Tunnel Cross Section

Most of the pipe sections at Kvilldal are rock tunnels with a noncircular cross-section. The model uses the correct cross-sectional area but assumes that the tunnels are circular. The friction in these cross sections is smaller, due to the reduction in the area of the walls, where

frictional forces act. However, the assumption does not affect the propagation speed of the pressure waves and is therefore considered tolerable.

Pipeline Junction

Kvilldal hydropower plant has four turbines and one blind tunnel which results in four bifurcations in the piping system. Figure 4.4 illustrates junction 4 closest to the headrace tunnel in Kvilldal. The equations used to solve the fundamental equations in the junction are presented below.

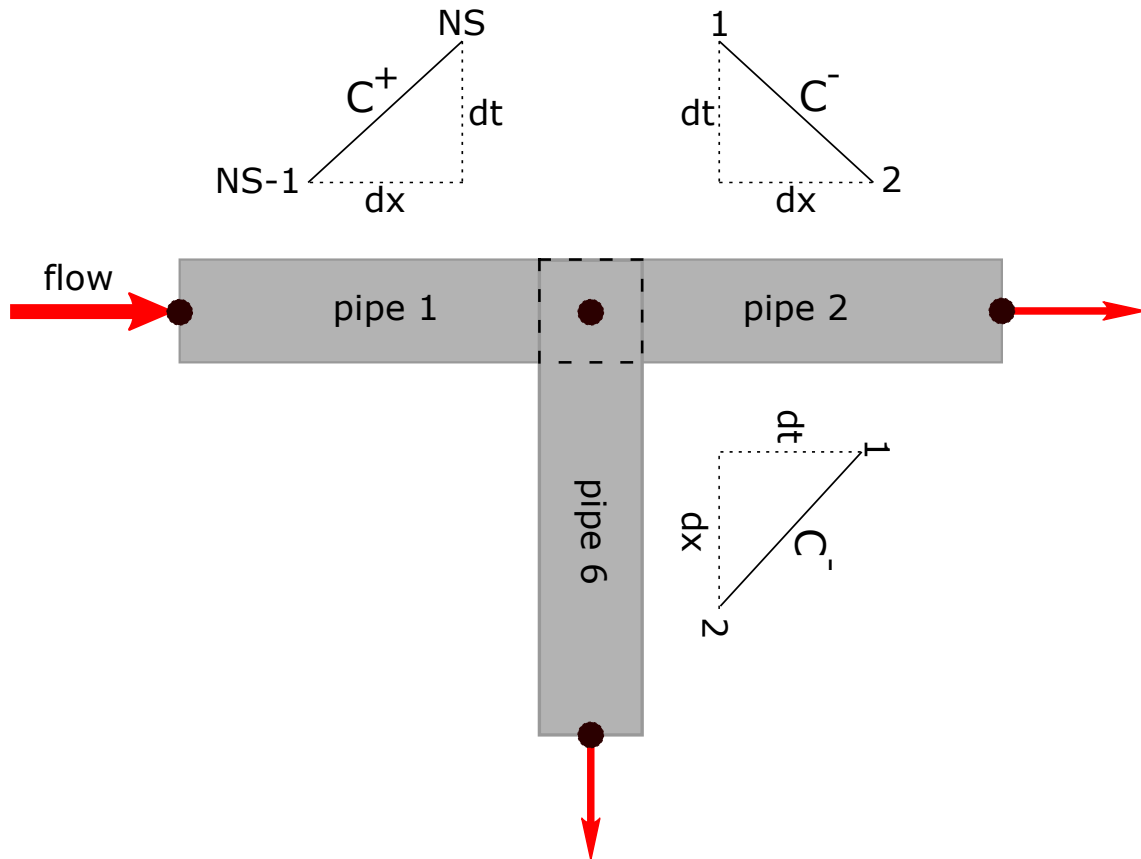


Figure 4.4: Representation of the computational domain related to junction 4 in the 1D model of Kvilldal. The center of the junction is the common point $pipe1.NS$, $pipe2.1$ and $pipe6.1$

Common head:

$$H_{junction} = H_{pipe1.NS} = H_{pipe2.1} = H_{pipe6.1} \quad (4.20)$$

Continuity:

$$Q_{pipe1.NS} = -\frac{H_{pipe1.NS}}{B_{pipe1}} + \frac{CP_{pipe1.NS}}{B_{pipe1}} \quad (4.21)$$

$$Q_{pipe2.1} = \frac{H_{pipe2.1}}{B_{pipe2}} - \frac{CM_{pipe2.1}}{B_{pipe2}} \quad (4.22)$$

$$Q_{pipe6.1} = \frac{H_{pipe6.1}}{B_{pipe6}} - \frac{CM_{pipe6.1}}{B_{pipe6}} \quad (4.23)$$

The flow into the junction need to be equal to the flow going out. Equation 4.21 4.22 and 4.23 can be combined to form equation 4.24.

$$H_{junction} = \frac{CP_{pipe1.NS}/B_{pipe1} + CM_{pipe2.1}/B_{pipe2} + CM_{pipe6.1}/B_{pipe6}}{1/B_{pipe1} + 1/B_{pipe2} + 1/B_{pipe6}} \quad (4.24)$$

Series Junction

The tunnel system between each pipeline junction and turbine consists of a rock tunnel leading into a steel penstock. The sections have different propagation velocities, friction factors, and cross sections. A series junction is therefore introduced in order to create two pipe sections with different properties.

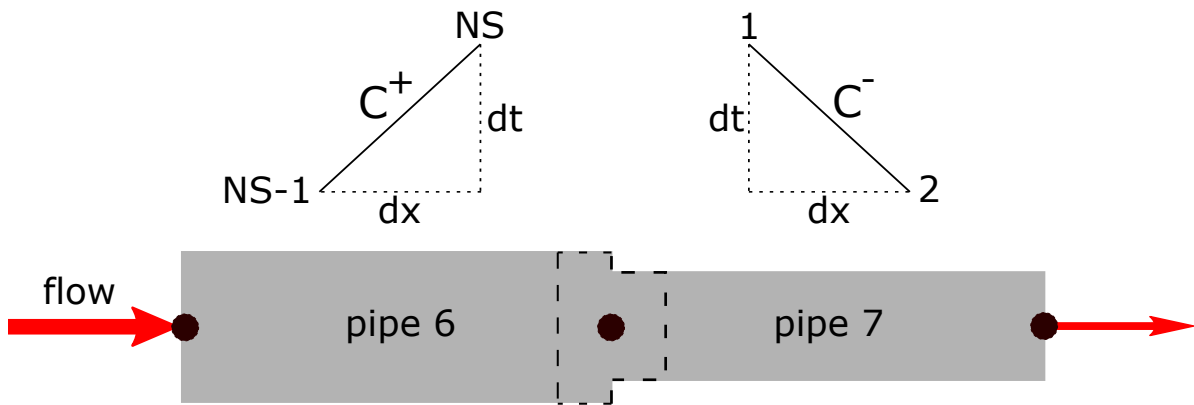


Figure 4.5: Representation of the computational domain related to the series junction between pipe 6 and pipe 7 in the 1D model of Kvilldal.

Figure 4.5 illustrates the sections between junction 4 and turbine 4 in the numerical model of Kvilldal. The following equations solve the fundamental equations in the series junction between the rock tunnel and penstock.

$$Q_{pipe6.NS} = Q_{pipe7.1} \quad (4.25)$$

$$H_{pipe6.NS} = H_{pipe7.1} \quad (4.26)$$

Solving Equations 4.25 and 4.26 simultaneously yields:

$$Q_{pipe7.1} = \frac{CP_{pipe6.NS} - CM_{pipe7.1}}{B_{pipe6} + B_{pipe7}} \quad (4.27)$$

The parameters in Equation 4.27 are all available from the previous time step.

Reservoir Boundary

The boundary at the air cushion chamber is assumed to be constant since the frequencies related to pressure fluctuations in the chamber are lower than the frequencies under investigation. Equation 4.28 sets constant head as boundary condition at the first point in pipe 1 in the numerical model.

$$H_{pipe1.1} = H_{reservoir} \quad (4.28)$$

Equation 4.15 can be applied directly to obtain the flow, $Q_{pipe.1}$.

Blind Tunnel boundary

For the blind tunnel at Kvilldal the following boundary condition is used.

$$Q_{pipe5.NS} = 0; \quad (4.29)$$

$H_{pipe5.NS}$ is obtained directly from equation 4.14

Turbine Boundary

The turbines in the one-dimensional simulation are modeled as valves. This gives the opportunity to shut down turbines and also implement a sinusoidal discharge function. Some constants need to be defined to enable the final expression for the flow rate at the boundary. Using turbine 4 at the end of *pipe7* as an example, Q_{0T4} and H_{0T4} are the initial flow and head at the turbine. Q_{0T4} is set and H_{0T4} is calculated from the initial conditions. τ is defined as the valve closure relationship and is described by equation 4.30. $\tau = 0$ resembles a closed valve, $\tau = 1$ describes a fixed orifice.

$$\tau = \left(1 - \frac{t}{t_c}\right)^{E_m} \quad (4.30)$$

Equation 4.30 is used when $t > t_c$ simulating a turbine closing. t is the current time in the simulation while t_c is a set constant describing the time it takes to close the valve. E_m governs the shape of $\tau(t)$, $E_m = 1.5$ is used in the simulations of Kvilldal as in an example by Wylie and Streeter in [11].

Equation 4.31 is introduced to simplify the final expression for $Q_{pipe7,NS}$ at turbine 4 given by equation 4.32. A sinusoidal boundary can be implemented by changing τ to a sinusoidal function.

$$C_v = \frac{(Q_{0T4}\tau)^2}{2H_{0T4}} \quad (4.31)$$

$$Q_{pipe7.NS} = -B_{pipe7}C_v + \sqrt{(B_{pipe7}C_v)^2 + 2C_vCP_{pipe7.NS}} \quad (4.32)$$

$H_{pipe7.NS}$ can be found by applying equation 4.14.

4.4 Validation and Verification

The characteristic method is a well established method, which means that verification and validation exists in multiple articles and books such as [15] [11] [4]. Previous sections discuss the limitations of the method. The main purpose of this section is to present the steps made to ensure that the characteristics method is implemented correctly, in the numerical models of Kvilldal and the Hydropower Laboratory.

- First, a one-dimensional model of a pipe with a reservoir upstream and valve downstream was created, and validated against an example by Streeter et al. in [11].
- Validating the full pipe system seen in Figure 4.1 was more challenging. The main concern was the calculations through the branching junctions. (Calculation of the internal points in the full model are identical to the internal points in the example above.)

The solution was to simulate the entire system with the following parameters: **wave speed $a = 1000m/s$ in all pipe sections.** $pipe1 = 1000m$, **all other pipes equal to 100m.** The initial head and flow was also set. The valve at each turbine boundary was closed at $t = 0s$, which resulted in pressure waves propagating from each turbine. Figure 4.6 illustrates the flow at the reservoir during the simulation. The flow changes when the propagating pressure waves reach the reservoir.

The time instances where the flow alters in figure 4.6, coincides with the expected times which are found by dividing the length between the reservoir and each turbine with the propagation velocity. ($turbine1 \rightarrow reservoir = 1.2s$, $turbine2 \rightarrow reservoir = 1.3s$, $turbine3 \rightarrow reservoir = 1.4s$, $turbine4 \rightarrow reservoir = 1.5s$).

- How long to simulate each instance was a concern. An independence study was carried out to investigate whether the maximum time of simulation, T_{max} would alter the spectral analysis on the turbine boundaries. Figure 4.7 shows the spectral analysis at turbine boundary 3 & 4 from closing turbine 1 at $t = 0s$. The peaks change as T_{max} changes. $T_{max} = 30$ is chosen to be sufficient for simulations where the pressure waves are excited by the closing of turbines.

Cases simulated with cyclic flow fluctuations at the turbine boundaries are chosen to have $T_{max} = 100s$, to ensure that the spectral analysis represents the cyclic transient events in the system.

- An independence study of dx is not conducted, since the initial dx is optimized in the simulations as described earlier.

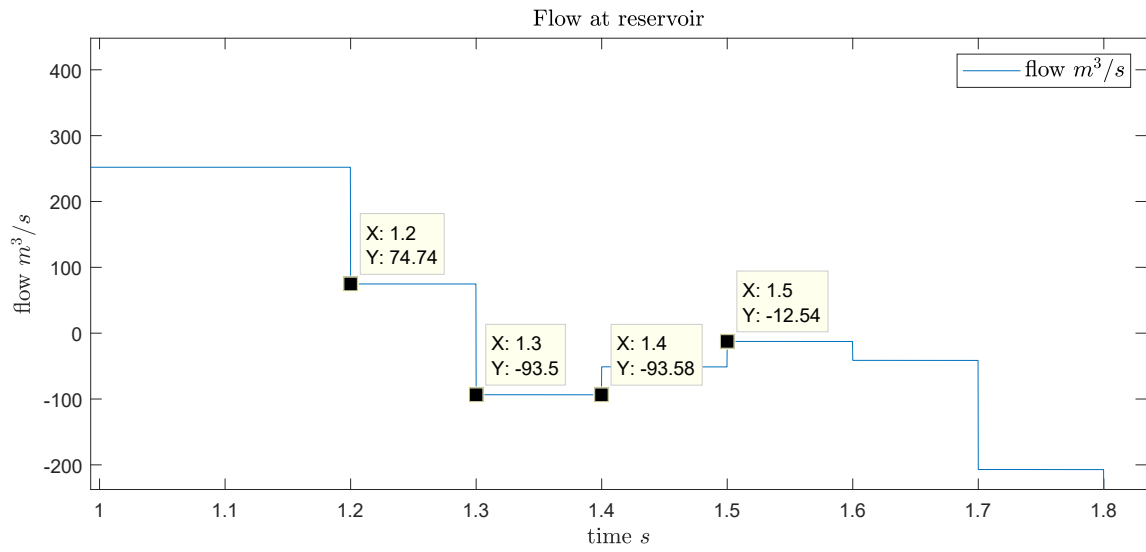


Figure 4.6: Flow at reservoir in the beginning of a simulation used to verify the simulation model.

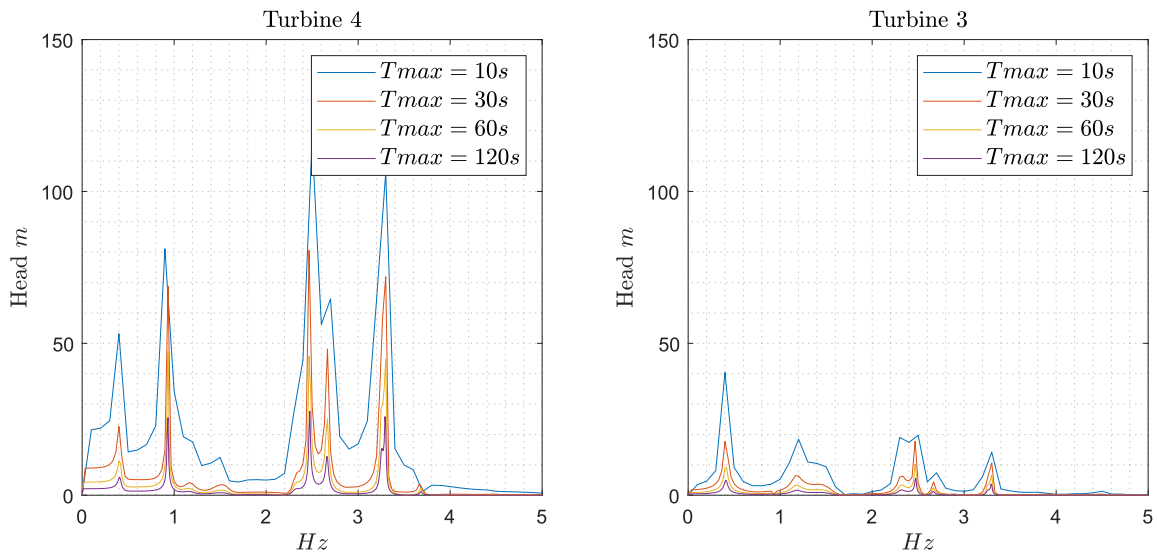


Figure 4.7: Independence study of simulation length, T_{max} .

4.5 Running a Simulation

This section describes the steps a user encounters during a simulation of the numerical code in MATLAB.

- Before starting a simulation, the following parameters should be set: Boundary conditions at each turbine, friction coefficient and propagation velocity in the rock tunnels, friction coefficient and wave velocity in the steel penstocks.
- As the simulation starts a note about the simulation and T_{max} are required as inputs. The simulation calculates the duration of the simulation. The user can set a T_{max} or continue.
- The user then chooses if a transient plot of the pressure development in the pipe sections should be illustrated. Figure 4.8 is a picture of the transient plot at $t = 0.06s$. The transient plot runs a number of iterations before the user chooses to continue with or without the transient plot. Running the plot slows down the calculations.
- Pressure values at the boundaries are stored for every time step and plotted when the simulation ends. The spectral analysis of the pressure at the turbine boundaries are plotted.
- The user can choose to store the spectral analysis from each turbine boundary in a matrix. Storing enables the possibility to compare several simulations with different parameters against each other. Figure 4.7 is one example of comparing four simulations.
- Lastly, the script prints out the fundamental frequencies related to pipe sections and several distances in the system.

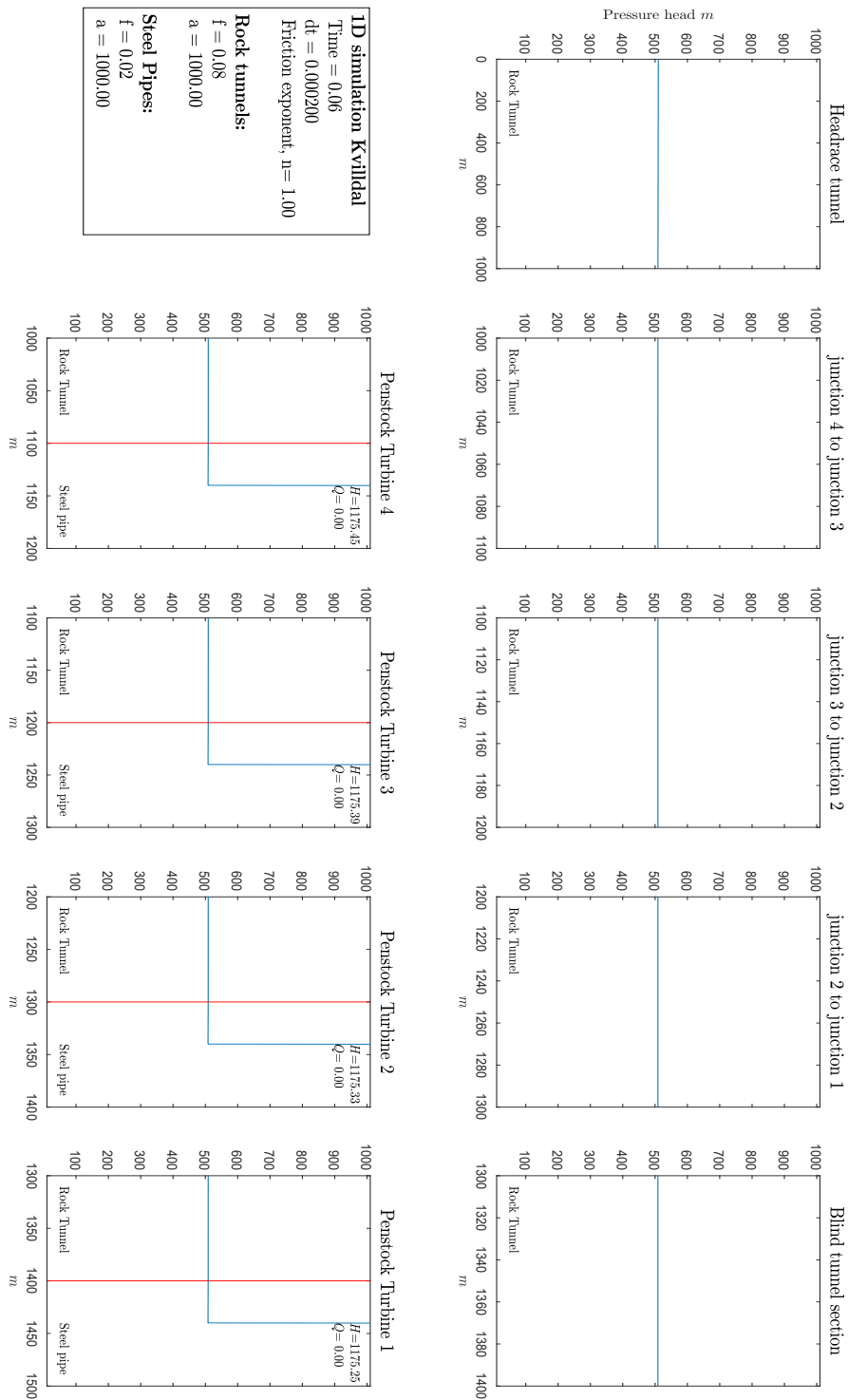


Figure 4.8: Transient plot of pressure in the conduit at Kvilldal. The flow at all turbines is set to zero at $t = 0$

Measurement Setup and Equipment

This chapter focuses on the measurement equipment, and setup used at the Hydropower Laboratory and Kvittdal hydropower plant.

5.1 Pressure Transducers

The devices used to measure the pressure in the laboratory and at Kvittdal are pressure transducers. The transducers convert mechanical effects produced by pressure into electrical signals.



(a) Kuhlite 365. Sensor PTIN2 in Figure 5.3



(b) UNIK 5000. Sensor IN3 in Figure 5.3

Figure 5.1: Pressure transducers in the Hydropower laboratory at NTNU.

For the measurements at Kvittdal all transducers are of the type UNIK 5000, the datasheet is found in [14]. Appendix C holds the serial number for four of the sensors used at Kvittdal together with the calibration certificates. The measurements conducted at the Hydropower laboratory at NTNU involves a mix of sensors, consisting of UNIK 5000 sensors and Kulite HKM 375 sensors, as shown in figure 5.1. The datasheet for the Kulite sensors is found in [26]. All the transducers are absolute pressure transducers connected to a data acquisition system, DAQ,

which converted the signals from the sensors to digital signals. A full list of the sensors are given in tables (5.1) and (5.2).

Sensors used in measurements at the Hydropower laboratory			
# of sensors and type	Location	Mounting	Mean H
3 * UNIK 5000	penstock	recessed	12.5 m
2 * Kulite HKM 375	penstock	flush	12.5 m

Table 5.1: Pressure transducers at the Hydropower Laboratory at NTNU

Sensors used in measurements at the Hydropower laboratory			
# of sensors and sensor type	Location	Mounting	Mean H
4*Unik 5000	penstock upstream bulb valve	recessed	535 m
4*Unik 5000	penstock downstream bulb valve	recessed	535 m
4*Unik 5000	draft tube cone	recessed	10-20 m

Table 5.2: Pressure Transducers at Kvittdal

5.2 Experimental setup

5.2.1 Hydropower Laboratory

Measurements were conducted at the Francis test rig in the Hydropower Laboratory at NTNU. Figure 5.2 shows, a 3D-model of the rig where the main components are labeled. The numbers follow the path of the water as the rig operates in an open loop configuration with a constant head of approximately 12.5 m.

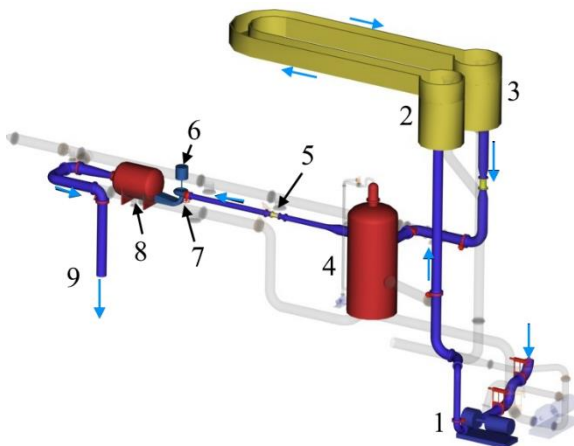


Figure 5.2: **Francis rig at NTNU in open loop configuration.** (1) centrifugal pump, (2) and (3) open water channel, (4) upstream pressure tank, (5) flowmeter, (6) generator, (7) Francis turbine, (8) downstream pressure tank, (9) water outlet to basement.

The pressure transducers in the Hydropower laboratory were placed as illustrated in figure 5.3, which is a 2D-drawing of components (4)-(8) in figure 5.2. The pressure transducers were connected to a DAQ and recorded by LabVIEW.

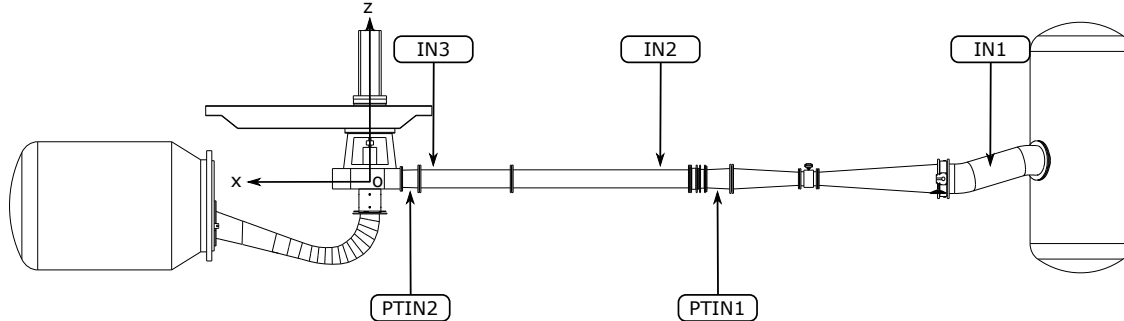


Figure 5.3: 2D illustration of location of pressure transducers in the Laboratory at NTNU

Placements and uncertainty <i>mm</i>				
Sensor	x	y	z	$\pm\mu$
PTIN2	-880	0	0	6
IN3	-1136	0	0	10
IN2	-6453	0	0	30
PTIN1	-7801	0	0	3
IN1	-13550	0	0	100

Table 5.3: Placement of the pressure transducers at the Hydropower Laboratory at NTNU

5.2.2 Kvilldal

Figure 5.4 and 5.5 illustrate the location of the pressure transducers at Kvilldal. The DAQ where all the sensors were connected, was placed on the concrete level over the spiral casing between turbine 2 and 3. The following chapter presents further information about the implementation of the measurements at Kvilldal.

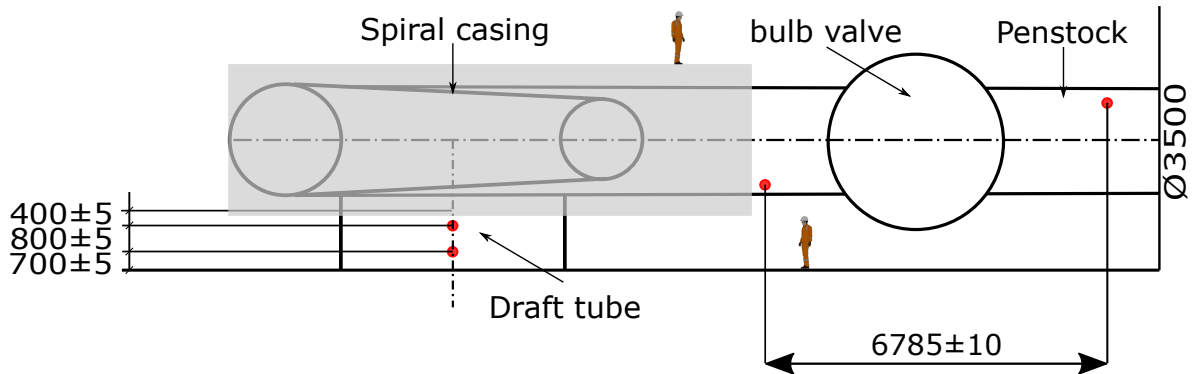


Figure 5.4: 2D sketch of the inlet, bulb valve, spiral casing and draft tube cone at Kvilldal. Measurements in *mm* with the uncertainty.

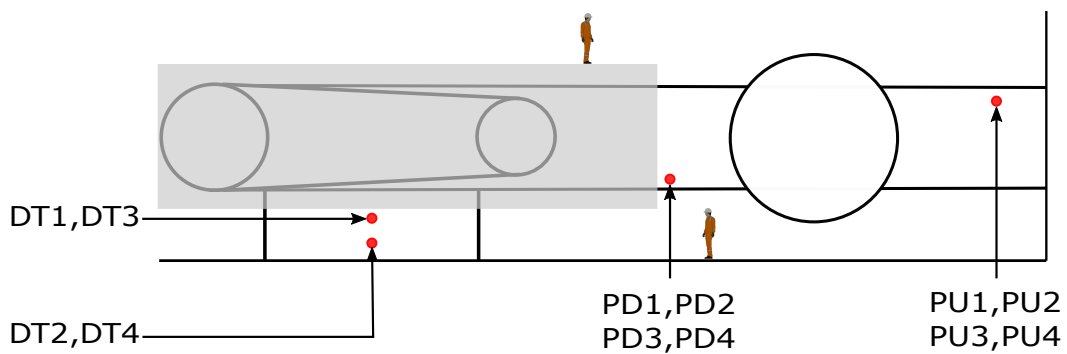


Figure 5.5: 2D sketch of where the different pressure transducers are located at Kvilldal.

Figure 5.5 shows where the pressure sensors are located on each turbine. PU = Penstock Upstream the bulb valve, PD = Penstock Downstream the bulb valve, and DT=Draft Tube. Numbers 1, 2, 3, 4 indicate which turbine the sensor is located on. This notation is used in the following chapters.

5.2.3 Uncertainties

The uncertainty of a measurement is a value that determines the quality of the measurement. The error in a measurement is the difference between the measured value and the actual value. All measurements of physical properties have some errors, and it is essential to identify and measure them. According to IEC 60193, the confidence interval of all uncertainties should be set to 95% [31].

Calibration of the UNIK 5000 pressure transducers, provided by NTNU, follows IEC 60193 [31]. The calibration provides an uncertainty related to the static pressure measurements given in the calibration certificates in Appendix C. Dynamic calibration methods are challenging to conduct as documented in [44]. Therefore, documentation of dynamic uncertainty does not exist. However, evaluation of the uncertainties related to dynamic properties is performed. The frequency response of the unik 5000 sensors is much higher than the frequencies investigated, (3500 Hz [14]). The response related to identical sensors, which are mounted identically, are assumed to be comparable, since factors determining the response are equal [2] [37]. The statement implies that the magnitudes of amplitudes in the spectral analysis from sensors with different mounting are incomparable.

Evaluation of the separate measurements is also necessary. After analyzing the results from Kvilldal, the spectral analysis related to some sensors uncovered much noise at higher frequencies, ($f > 50Hz$). The latter is a concern when analyzing RSI phenomenon. However, the level of noise detected in the range of the Rheingans frequency was low. As seen in figure 10.7, PU sensors have substantial cavities between the pipe flow and the transducer. The first natural frequency of the water string between the pipe and the flow is much higher than the frequencies related to pressure fluctuations caused by the turbine. Therefore, resonance in the water string is not the source of the noise. It is suspected, that discontinuities exist around the edges of the drilled holes for the transducers in the penstock. If there are metal fragments on the edges, these might cause noise. The holes are initially drilled for static pressure measurements which are not affected by the noise.

There are also uncertainties related to the measured distances both in the Hydropower laboratory and at Kvilldal. The uncertainties in the Hydropower and at Kvilldal can be found in table 5.3 and in figure 5.4.

Experimental Method

6.1 Hydropower Laboratory

The starting point for the analysis of the pressure measurements conducted in the Hydropower laboratory was the information in the basic theory chapter together with a one dimensional model of the laboratory. The following steps were conducted in order to investigate the dynamics in the turbine and the attached system.

- The pressure transducers were calibrated and mounted as described in the previous chapter.
- The turbine was operated with maximum guide vane opening to maximize the pressure pulses related to RSI. The speed of the turbine was changed between 200 *rpm* and 500 *rpm* with an increment of 10 *rpm* trying to provoke resonance in the penstock.
- LabVIEW was used to acquire the data. The sampling rate was 5000 *Hz* and each recording lasted 30 seconds.
- Post-processing of the data was performed in MATLAB. **Plots of pressure versus time** worked as a first inspection of the signal. **Spectral analysis** with MATLAB's `fft` function was used to investigate the amplitudes related to separate frequencies in the signal. The peaks in the spectral analysis were related to the phenomena discussed in the basic theory chapter, and to noise sources. **Seismic interferometry** and deconvolution interferometry was applied to find the wave speed in the penstock. A bandpass filter was applied to remove noise from the signal before using the functions `xcorr` and `deconv` in MATLAB. The next subsection describes the presentation of the results.
- **seismic interferometry** were applied to data from the numerical model of the penstock, in order to compare the measured results from the laboratory with a known system. The pressure in the numerical model was recorded and stored at five locations as in the experimental results. The location is not exactly the same, since this requires interpolation of the points in the numerical model. The shift in placement is taken into consideration in the post-processing by shifting the vertical lines on the x-axis in the plots which are described in the next subsection.

6.1.1 Seismic Interferometry Plots

The pressure propagation velocity can be found by applying seismic interferometry and deconvolution interferometry to experimental and simulated data. The results are obtained as described in the basic theory chapter and plotted with the **wiggle** function in MATLAB. Figure 6.1 shows how the results are plotted. The x- and y-axis represents distance and time. The response from Figure 3.18 in the basic theory chapter is added to illustrate that the responses are plotted vertically.

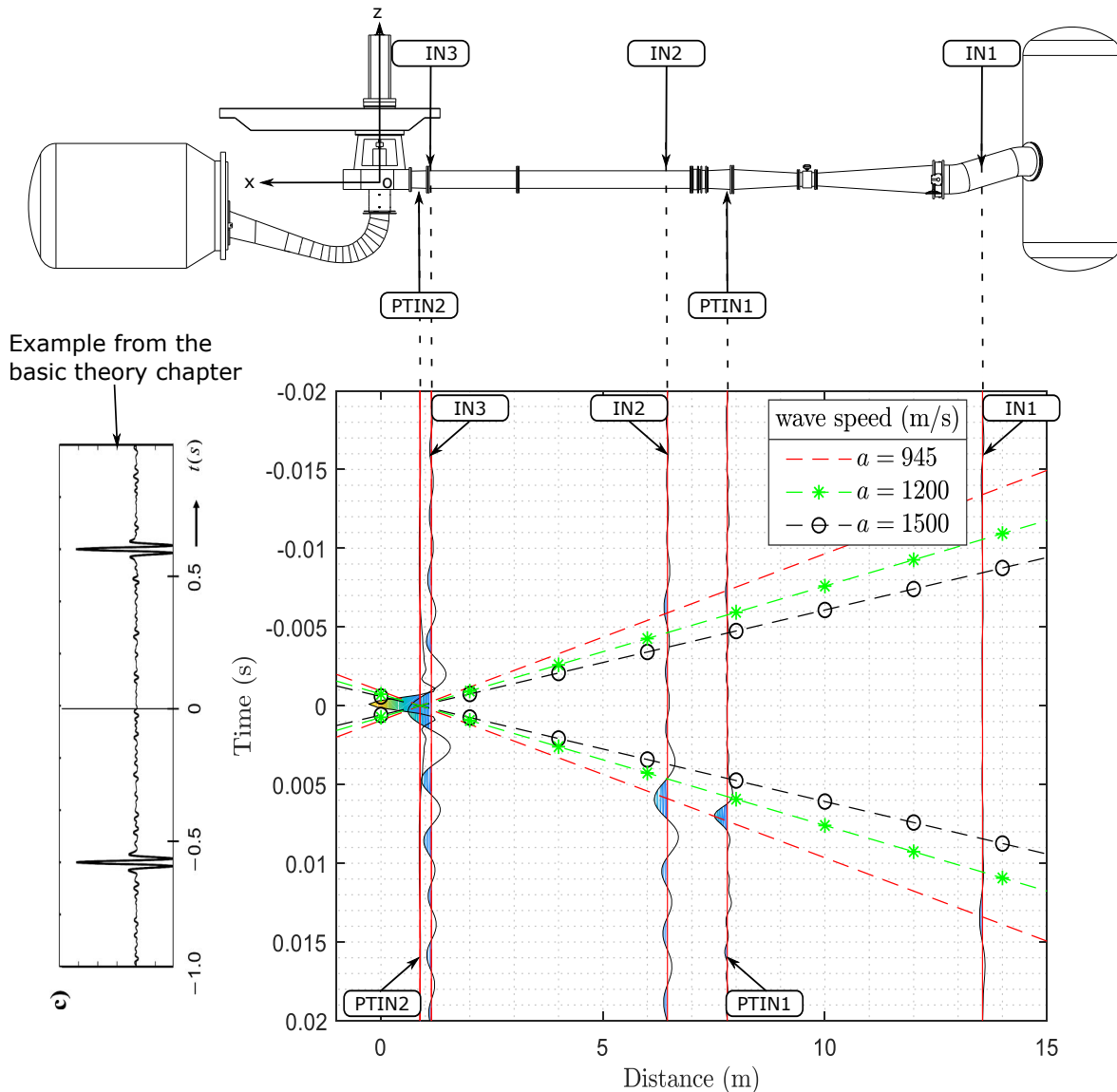


Figure 6.1: Seismic interferometry plot explained.

The vertical line closest to the turbine is chosen to be the reference signal, which is treated as the source. The responses to the source are obtained by cross-correlating each signal with the source. The responses, one for each sensor, are plotted vertically with a distance distribution equal to the distribution in the experimental setup or simulation. A wave speed is illustrated by plotting the trajectory of a response peak as it travels along the x-axis. The real wave speed

is found by fitting a line to the most significant peaks in the wiggle plot. The dotted gradient lines in Figure 6.1 represent the location of the response peaks with wave speeds as stated in the legend. The slopes of the trajectories are inversely proportional to the wave speeds.

6.2 Kvilldal

The measurements at Kvilldal hydropower station were conducted 7th of May 2019 10AM-5PM. NTNU, Flow Design Bureau AS, FDB, and Statkraft performed 111 measurement series at 34 operational points as presented in table 6.3. FDB specializes in flow measurements and provided eight of the pressure transducers and the DAQ system. Statkraft is the owner of Kvilldal power station and has had an essential role in the planning before, and assistance during the experiment.

- The power production from the power plant was restricted during the measurements. The ideal power production in terms of operational flexibility during the measurements was found before the experiment. The final hourly plan for total produced power from the four Francis turbines was given by Statkraft, trying to match the ideal scenario.
- 6th of May: Pressure transducers were mounted by Statkraft employees as illustrated in the previous chapter, and in appendix D. FDB set up the DAQ system and connected the transducers. A test sample was recorded, and a post-processing script was developed in MATLAB to control that all sensors were connected correctly.
- 7th of May: An operation plan for the individual turbines was produced based on the final power production plan. The operation plan consisted of the power output from each of the machines, varying the operational point every 12 minutes. The exact planned output from each machine was challenging to obtain, due to the manual operation. Actual output was, therefore, observed and noted. Figure 6.2 illustrates the power output from the turbines during the measurements. The turbines were operated in pairs for as many points as possible to compare turbines under the same circumstances. Turbine 3 was limited to 290 MW, which made the task difficult for some operational points. Statkraft also restricted the part load operation to a minimum of 50 % of best point efficiency (280 MW).
- Each operational point involved, 3 steady state measurement series with a 5000 Hz sampling rate lasting for 30. The post-processing script from the day before was used to control the quality of random samples. A live view of the pressure signals was also observed the entire time, and recordings of dynamic events were conducted when the pressure change was substantial. The dynamic measurement series vary between 60-180 seconds. Typical events measured were opening and closing of bulb valves.
- Turbine 3 and turbine 4 were closed during several of the operating points. This enabled measurement of transients upstream the closed bulb valves generated by the other turbines. It also gave the opportunity to conduct transient measurements related to closing and opening of the valves.
- Statkraft provided Supervisory Control And Data Acquisition data from the time the experiment was conducted. This was used to validate the observed power output performed in the power plant.
- FDB provided the measured data as tdms files. Scripts were made in MATLAB to convert the files and store them according to the measurement number. All post-processing scripts were then made to take in a selected amount of measurement series e.g., spectral analysis

of several measurements can be plotted in the same plot illustrating how the dynamics change in the power plant.

- The basic applied post-processing techniques used are spectral analysis, plotting of raw- and filtered-data, and seismic interferometry. The results also include plots investigating the relationship between load and pressure fluctuation frequencies. The main focus is to uncover the existence of transients in the penstocks.
- The results chapter presents two main cases. **Case 1. Different waterway configurations:** The measurements comprise 6 waterway configurations presented in table 6.1. The configurations are chosen based on the theory in chapter 3, and the results from the numerical model. Table 6.1 only includes the steady state measurement series.

Waterway configurations		
configuration nr.	Description	measurement series nr.
1	Turbine 4 spin no load	1-6
2	All Turbines loaded	7-24 & 40-57
3	Turbine 2 spin no load	27-38
4	Turbine 4 closed bulb valve	60-92
5	Turbine 4 & 3 closed bulb valve	96-98
6	Turbine 3 closed bulb valve	100-111

Table 6.1: Waterway configuration cases investigated.

Case 2. Transient events: As stated above some measurement series were conducted due to the observation of substantial pressure fluctuation. Table 6.2 presents the dynamic measurement series.

Transient events		
Event nr nr.	Description	measurement series nr.
1	Bringing Turbine 2 to spin no load	25-26
2	Turbine 2 & 3 at part load	39
3	Closing bulb valve Turbine 4	58-59
4	Closing bulb valve turbine 3	93-95
5	Opening bulb valve Turbine 4	99

Table 6.2: Transient events and measurement series numbers.

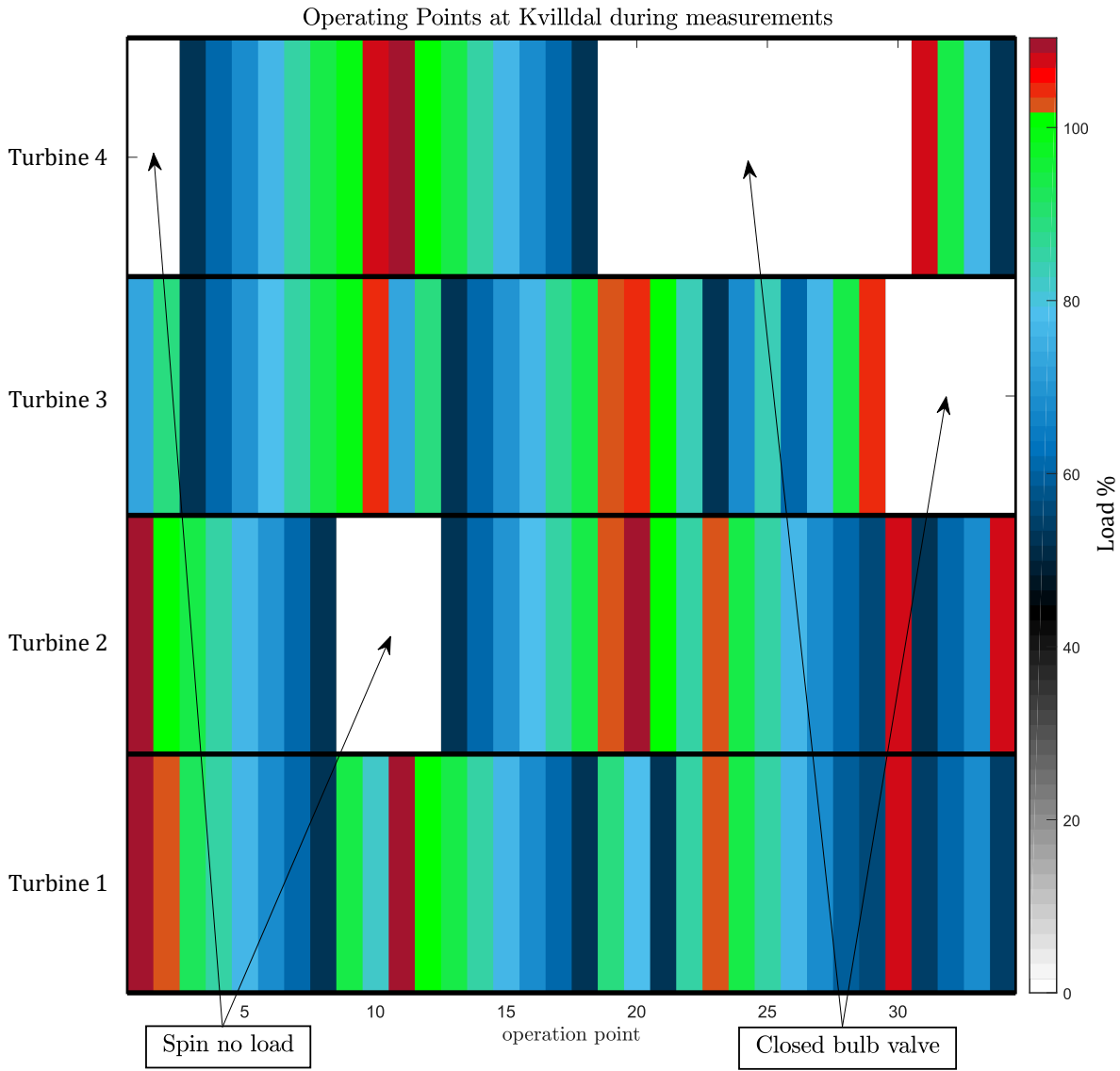


Figure 6.2: Power output for each turbine during the measurements.

Power <i>MW</i> as observed in the power station					
Operation point	Turbine 1	Turbine 2	Turbine 3	Turbine 4	measurement nr.
1	308	308	204	0	1-3
2	285	284	249	0	4-6
3	260	262	148	148	7-9
4	239	241	172	169	10-12
5	216	215	195	193	13-15
6	193	194	218	216	16-18
7	171	170	239	241	19-21
8	147	147	262	263	22-24
9	265	0	279	276	25-29
10	230	0	290	300	30-32
11	307	0	204	308	33-35
12	284	0	251	284	36-38
13	261	148	148	261	39-42
14	239	172	170	240	43-45
15	216	194	195	216	46-48
16	193	219	217	193	49-51
17	170	240	242	169	52-54
18	146	263	264	148	55-57
19	249	285	285	0	58-62
20	222	309	290	0	63-65
21	148	282	281	0	66-68
22	241	238	233	0	69-71
23	285	286	145	0	72-74
24	263	261	191	0	75-77
25	238	239	236	0	78-80
26	216	214	170	0	81-83
27	193	192	214	0	84-86
28	168	170	261	0	87-89
29	155	155	290	0	90-92
30	301	301	0	0	93-98
31	150	149	0	300	99-102
32	170	172	0	261	103-105
33	193	193	0	214	106-108
34	151	300	0	149	109-111

Table 6.3: Operating points, Turbine power output and measurement series numbers related to each operation point.

6.3 Simulation of Kvilldal

The development of the numerical one dimensional model of Kvilldal is described in chapter 4. The model was used to investigate how system parameters such as pipe lengths, wave speeds, and excitation forces affect the transients in the system. As stated in chapter 4, the model does not intend to replicate specific events at Kvilldal due to the simplicity of the model and the complexity of the actual physical system. The model does, however, provide an exact representation of the transient behavior in the modeled system, which can be used to investigate trends in the actual system.

The investigation of transients was performed by running several simulations with different settings and comparing the spectral analysis obtained at the turbine boundaries. Some cases tested are listed below.

- With a sin function controlling the flow at turbine 1, different frequencies were investigated. The length of some pipe sections were altered to see if they were the sections which induced resonance.
- Four simulations with each turbine closing. Closing turbine 1 at $t = 0$ in the first simulation, turbine 2 in the second, etc. Each simulation creates a pressure wave which originates from the turbine boundary of the closing turbine..
- The propagation velocity in the rock tunnels was investigated with the following values $a_{RockTunnel} = [600m/s, 800m/s, 1000m/s, 1200m/s]$ while closing turbine 1 at $t = 0$ to provoke transients
- The propagation velocity in the steel pipes was investigated with the following values $a_{SteelPipe} = [900m/s, 1100m/s, 1300m/s, 1500m/s]$ while closing turbine 1 at $t = 0$ to provoke transients.
- The length of each pipe section was altered. Resulting in a total of 13 cases trying $L = [1m, 50m, 100m, 500m]$. Closing turbine 1 at $t = 0$
- The friction factor was altered. Closing turbine 1 at $t = 0$.
- Eventful measurement series from Kvilldal inspired some simulations, which were compared. Sinusoidal flow control and zero flow were used to simulate pressure fluctuations and closed bulb valves at the turbine boundaries.

Some of the examples listed are presented in the results chapter.

Results

7.1 Hydropower Laboratory

The main results from the experiments in the Hydropower Laboratory were obtained by applying seismic interferometry to simulated and measured pressure data. The results are plotted as described in chapter 6.

7.1.1 Seismic Interferometry and Deconvolution interferometry on Simulated Data

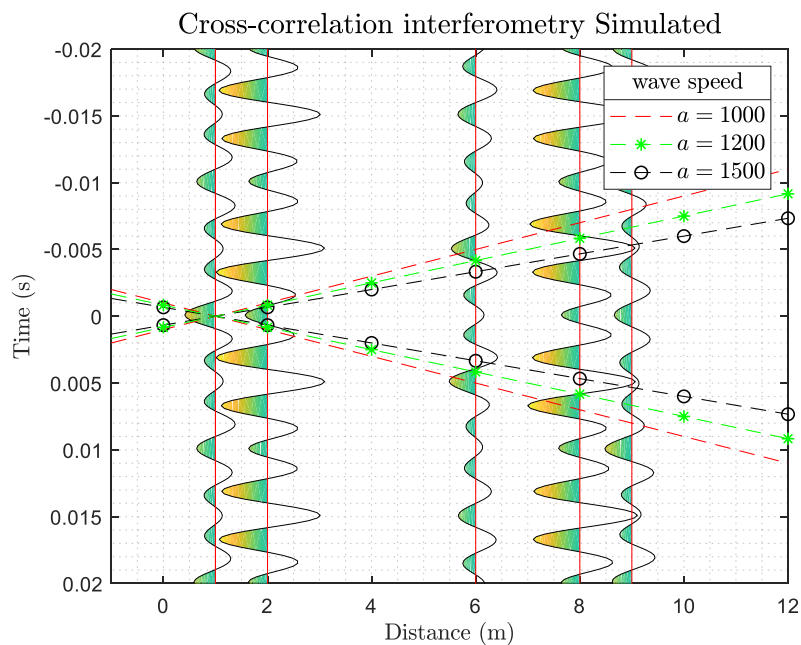


Figure 7.1: Seismic interferometry applied to simulated data.

Figure 7.1 shows the results from applying seismic interferometry to data obtained from the numerical model of the Hydropower Laboratory. The wave speed is set to be 1000 m/s and

the pressure fluctuations in the penstock are excited by a complex function located at $x=0$. It is difficult to conclude from figure 7.1 to what is the wave speed.

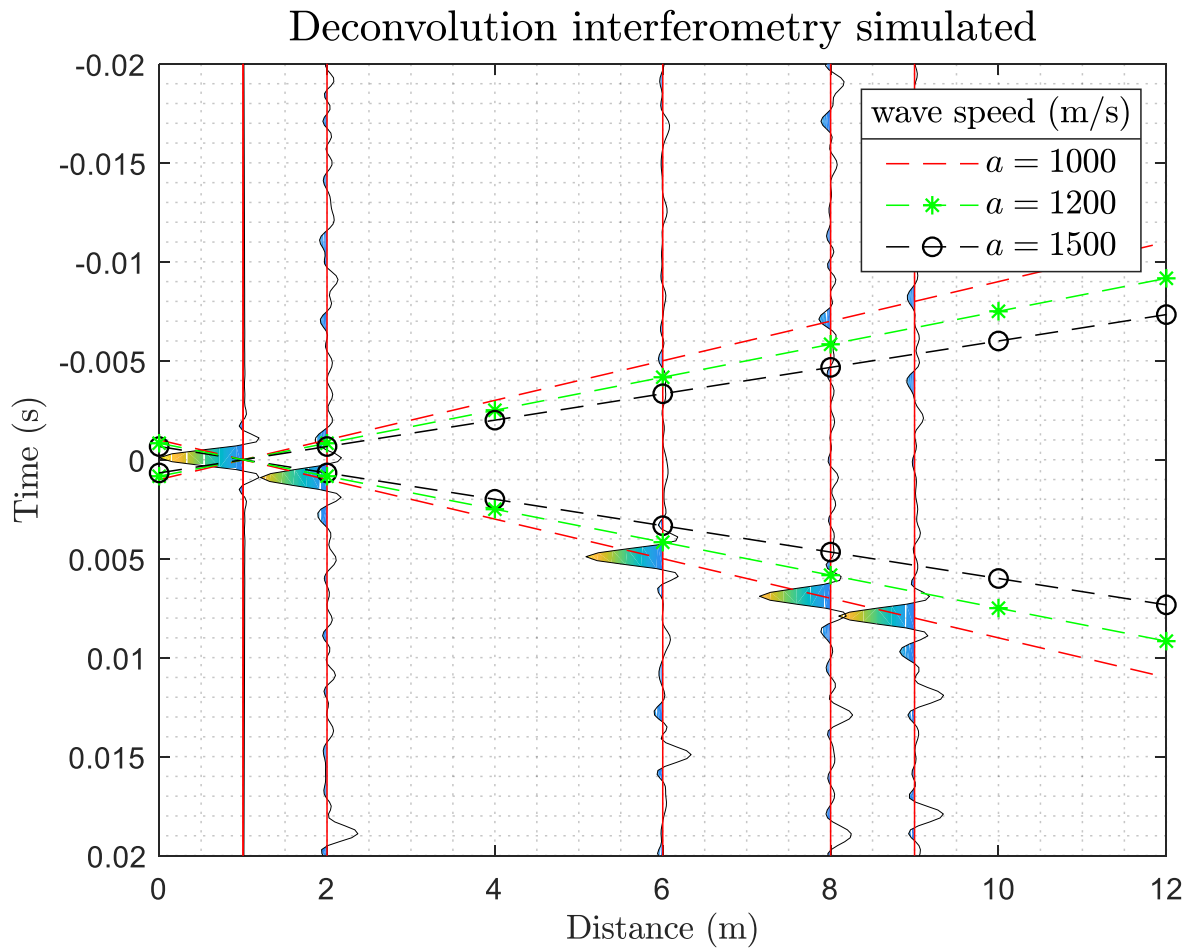


Figure 7.2: Deconvolution interferometry applied to simulated data.

Figure 7.2 shows the result of applying deconvolution interferometry to the same simulated data as in Figure 7.1. The most significant response peaks align on the red dashed gradient representing a propagation velocity of 1000 m/s . The information describing the response in the negative time domain is lost in the deconvolution process [47].

7.1.2 Seismic Interferometry and Deconvolution interferometry on Experimental Data

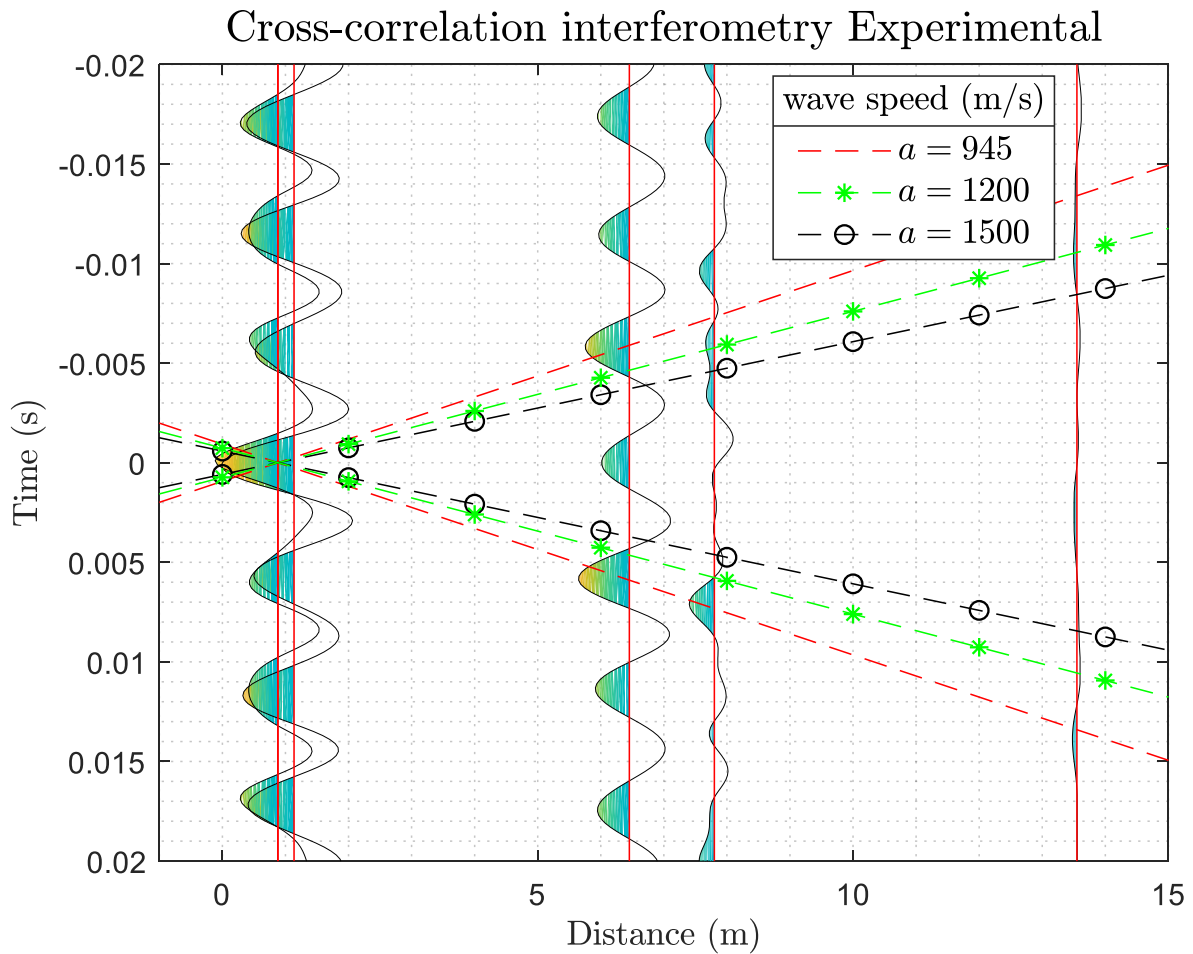


Figure 7.3: Seismic interferometry applied to measurements from the Hydropower Laboratory.

Figure 7.3 shows cross-correlation applied to the measured data in the hydropower laboratory. The sensor placement is found in table 5.3. The seemingly largest responses follow the dashed line representing a wave speed of approximately 945 m/s . The line is fitted by trial and error. It is, however, difficult to conclude to what is the wave-speed from the figure due to the presence of other peaks.

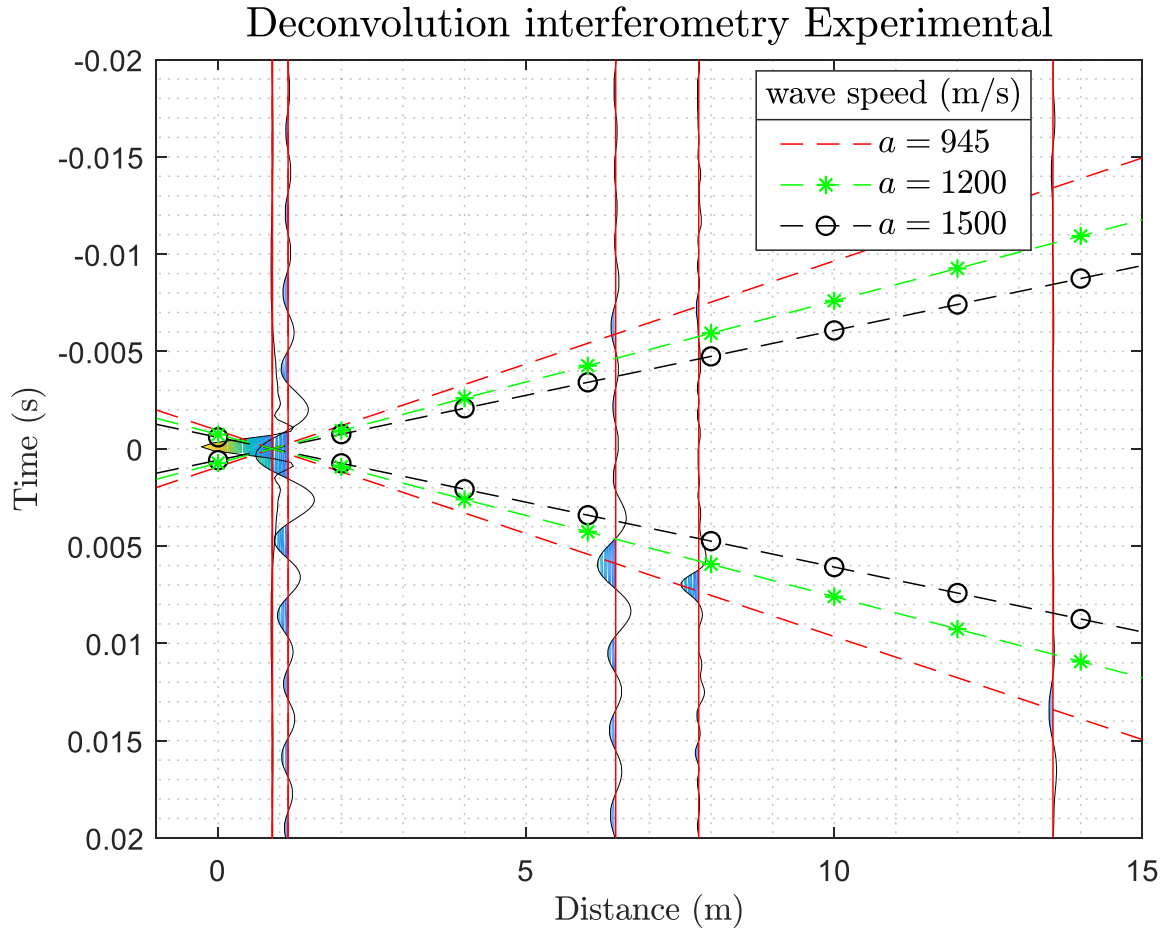


Figure 7.4: Deconvolution interferometry applied to measurements from the Hydropower Laboratory.

Figure 7.4 displays the result of applying deconvolution interferometry to the same measured data as in Figure 7.3. The peaks of the responses follow the dashed red line indicating a propagation velocity of approximately 945 m/s .

7.2 Kvilldal One Dimensional Model

Some cases described in chapter 6 are presented in this section to highlight how the dynamics in the complex waterway system at Kvilldal depend on different parameters.

7.2.1 Changing Blind Tunnel

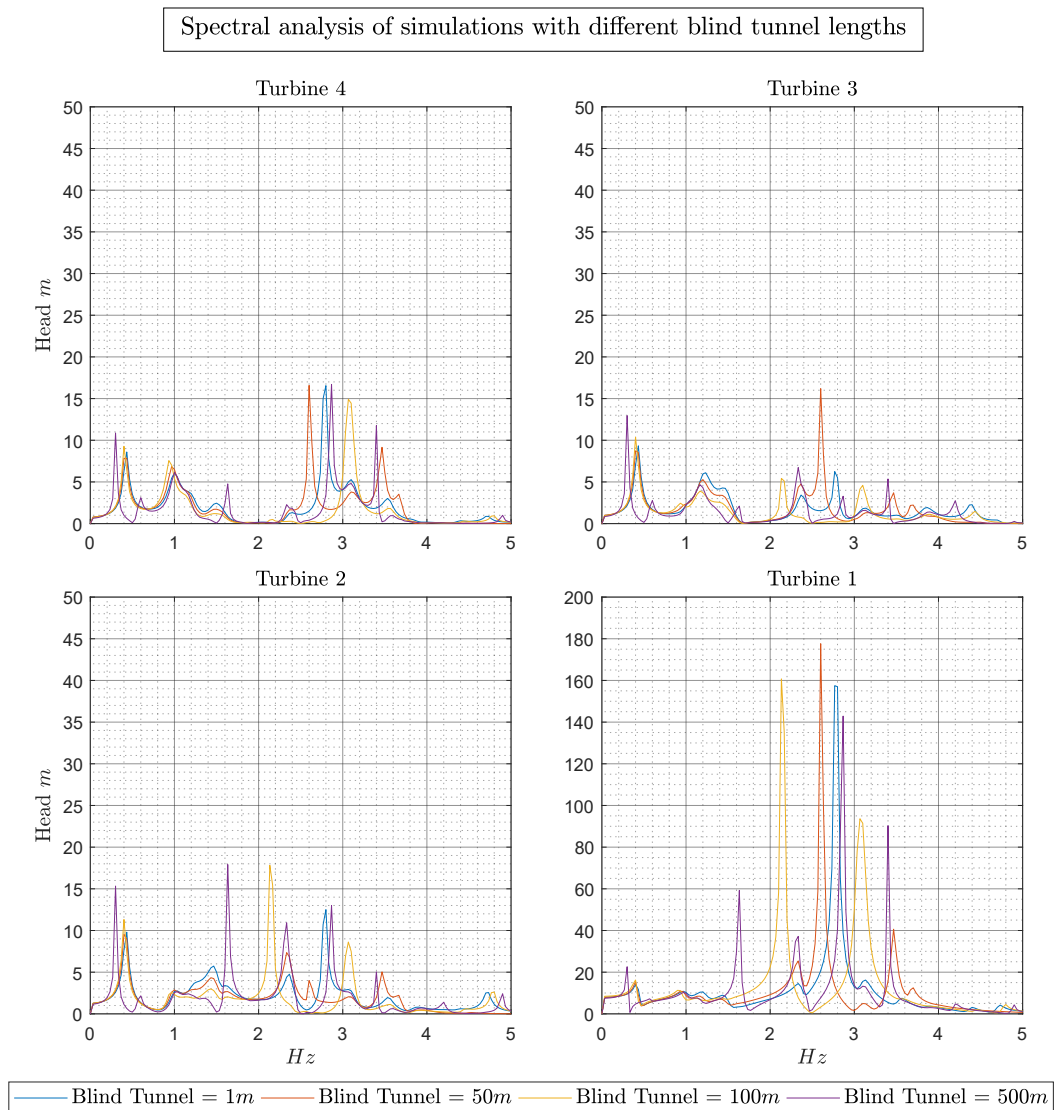


Figure 7.5: 4 cases simulated, spectral analysis from changing blind tunnel lengths.

Figure 7.5 shows how peaks in the spectral analysis from the turbine boundary in the simulated model change when altering the blind tunnel's length. The flow at all turbines are initially set to $63 \text{ m}^3/\text{s}$, turbine 1 is closed, i.e. $Q = 0 \text{ m}^3/\text{s}$ at $t = 0\text{s}$ which provokes transients.

7.2.2 Closing Different Turbines

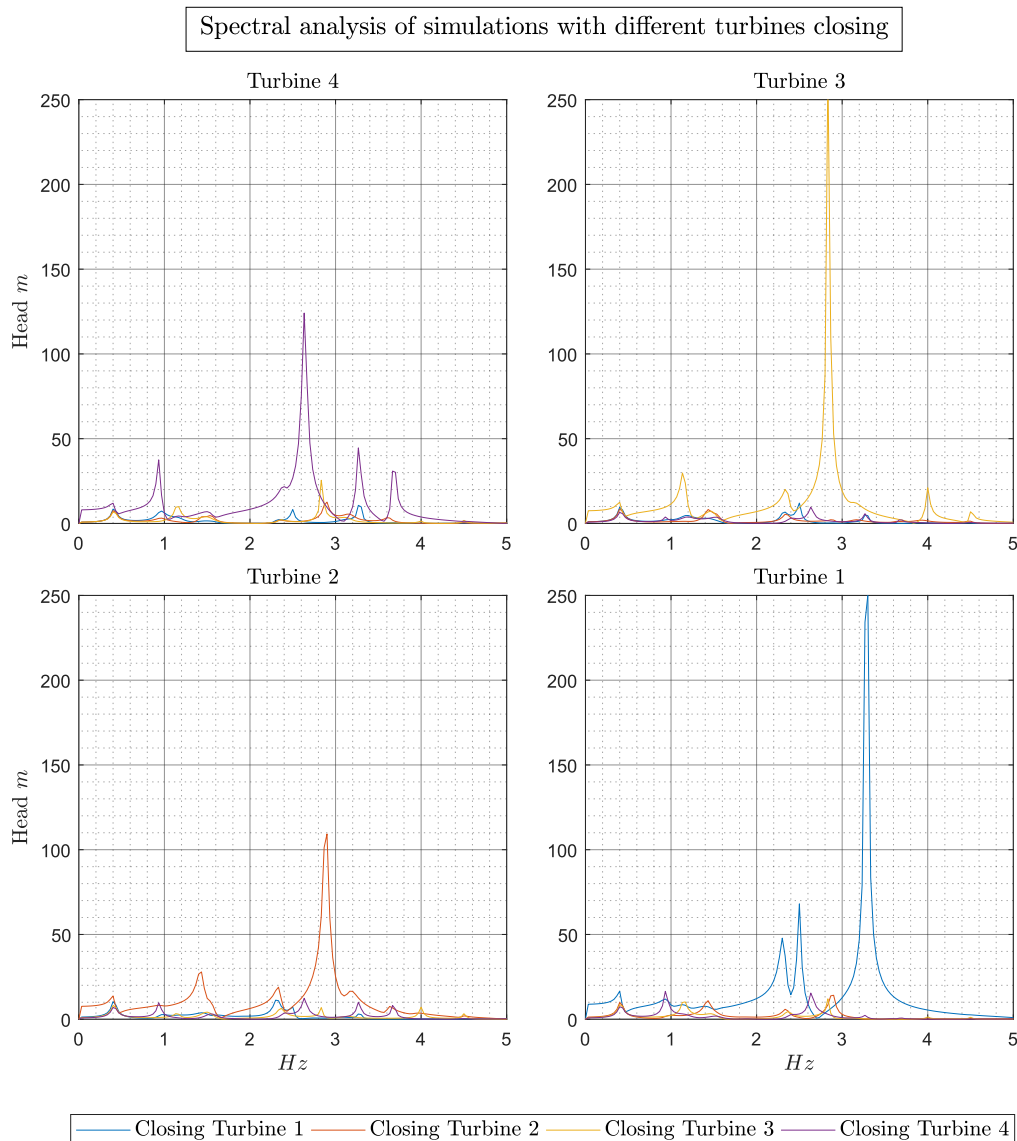


Figure 7.6: 4 cases simulated, spectral analysis from closing different turbines.

Figure 7.6 illustrates how the spectral analysis at each turbine boundary change when closing each turbine separately. The initial flow at all turbines is set to $63 \text{ m}^3/\text{s}$. Closing each turbine at $t = 0 \text{ s}$, generates transients in the four cases, i.e., case 1: turbine 1 is closing, case 2: turbine 2 is closing, etc. Closing a turbine results in creating a new reflection point which alters the waterway system, which leads to a different result in the spectral analysis.

Figure 7.5 and figure 7.6 are two of many attempts to understand what affects the transients at Kvilldal. The first approach was to look at the fundamental frequencies related to each pipe section and distances between reflection points such as the blind tunnel, junctions, turbines, and the air cushion chamber. The frequencies with the highest amplitudes in the spectral analysis were often close to some of the calculated frequencies but did in general not match them exactly.

In some cases, the fundamental frequency of the steel penstock did show up, and so did the frequency of the blind tunnel. Certain frequency areas in the spectral analysis seem to be more dependent on specific parameters, and some observations are listed below.

- Amplitudes related to low frequencies ($f < 0.5 \text{ Hz}$) are more affected by altering the headrace and the propagation velocity in the rock tunnels. They are not affected by closing different turbines and are seemingly most affected by the upper most part of the pipe system, i.e. the pipe sections 1-5 in the numerical model which can be found in figure 4.1.
- The peaks around 1 Hz in figure 7.5 are seemingly less sensitive to the change in the blind tunnel length, and are likely to be related to other pipe sections.
- The blind tunnel length affects the amplitudes in the entire frequency range displayed in figure 7.5. The changes around 0.5 Hz and $2\text{-}3.5 \text{ Hz}$ are most significant in the first three cases where the tunnel length range is $1\text{-}100 \text{ m}$. The change to 500 m creates an additional amplitude peak with a frequency of around 1.5 Hz . The latter amplitude is highest on turbine boundary 1 but is visible at all the other turbine boundaries as well.

Comparing the highest amplitude in figure 7.5 with figure 7.6 shows that the actual length of the blind tunnel at Kvilddal cause higher amplitudes than the other cases tested. In figure 7.6 the blind tunnel length is set from construction drawings, and in case 1, the excitation force is identical to all cases in figure 7.5. It is difficult to conclude if the actual system at Kvilddal would behave in the same manner. The propagation velocity is uncertain and plays an essential role, as documented in chapter 3. However, the propagation velocities in case 1 are in the expected range, (1000m/s in rock tunnels, 1300m/s in steel pipes), meaning that the blind tunnel at Kvilddal might have an unfortunate length.

7.2.3 Waterway Configurations

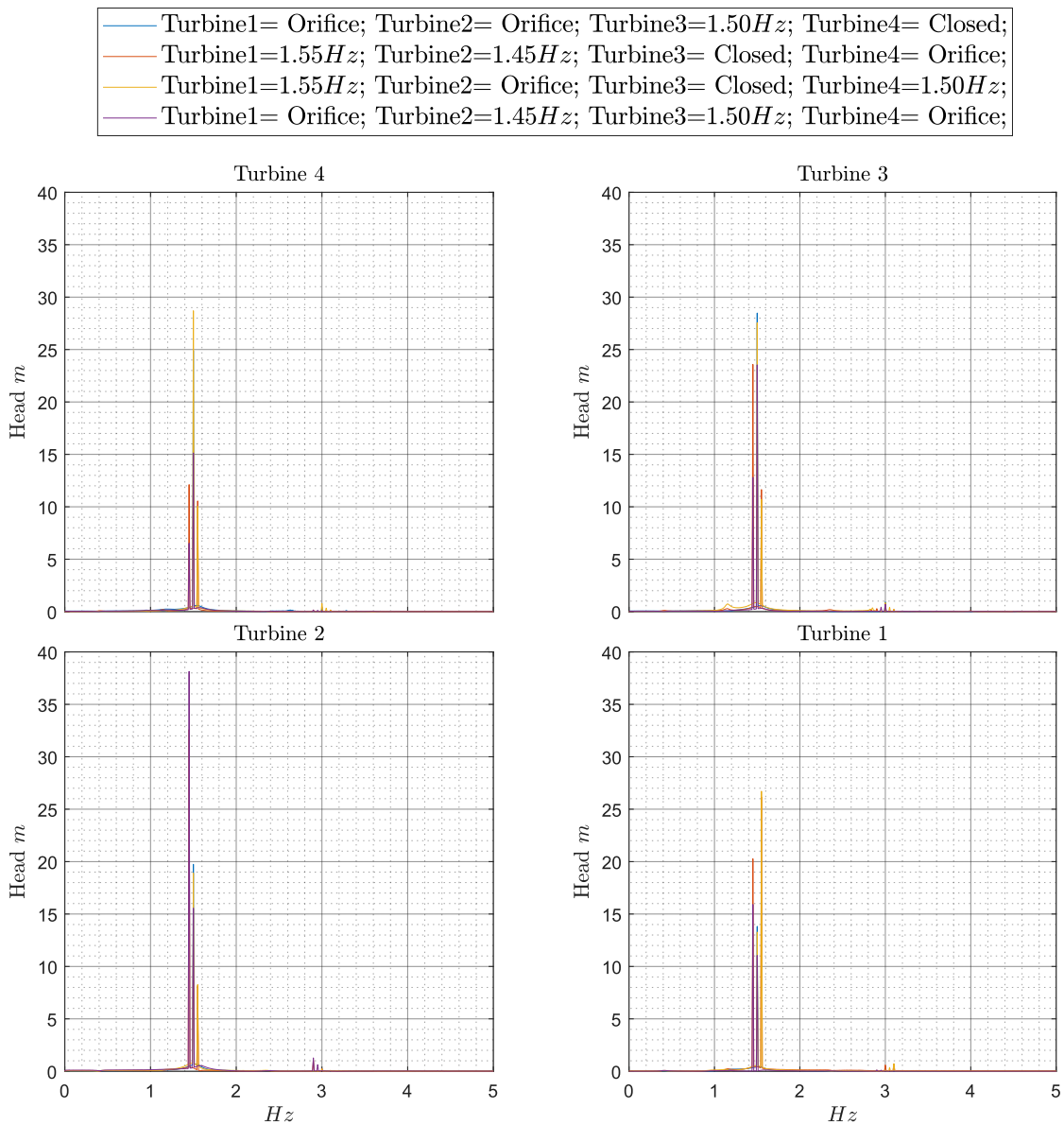


Figure 7.7: 4 cases simulated with a combination of closed bulb valves and excitation forces. Spectral analysis with high amplitudes.

Figure 7.7 shows how the highest amplitudes in the spectral analysis always have the same frequency as an exciting cyclic force if such an exciter is present. The spectral analysis is conducted at the four turbine boundaries during the four cases described in the figure. Valves on the turbine boundaries govern the flow with a sine function with a constant amplitude, which excites cyclic flow and pressure fluctuations in the system. Turbine 2 is experiencing the largest amplitude, and this happens during case 4. Amplitudes related to the second harmonic of the excitation frequency are also visible with frequencies around 3 Hz. The fact that the excitation force governs the frequencies related to the highest amplitudes in the spectral analysis is in agreement with all the part load measurements conducted at Kvilldal where the highest ampli-

tudes both upstream and downstream the turbines were related to the Rheingans frequency.

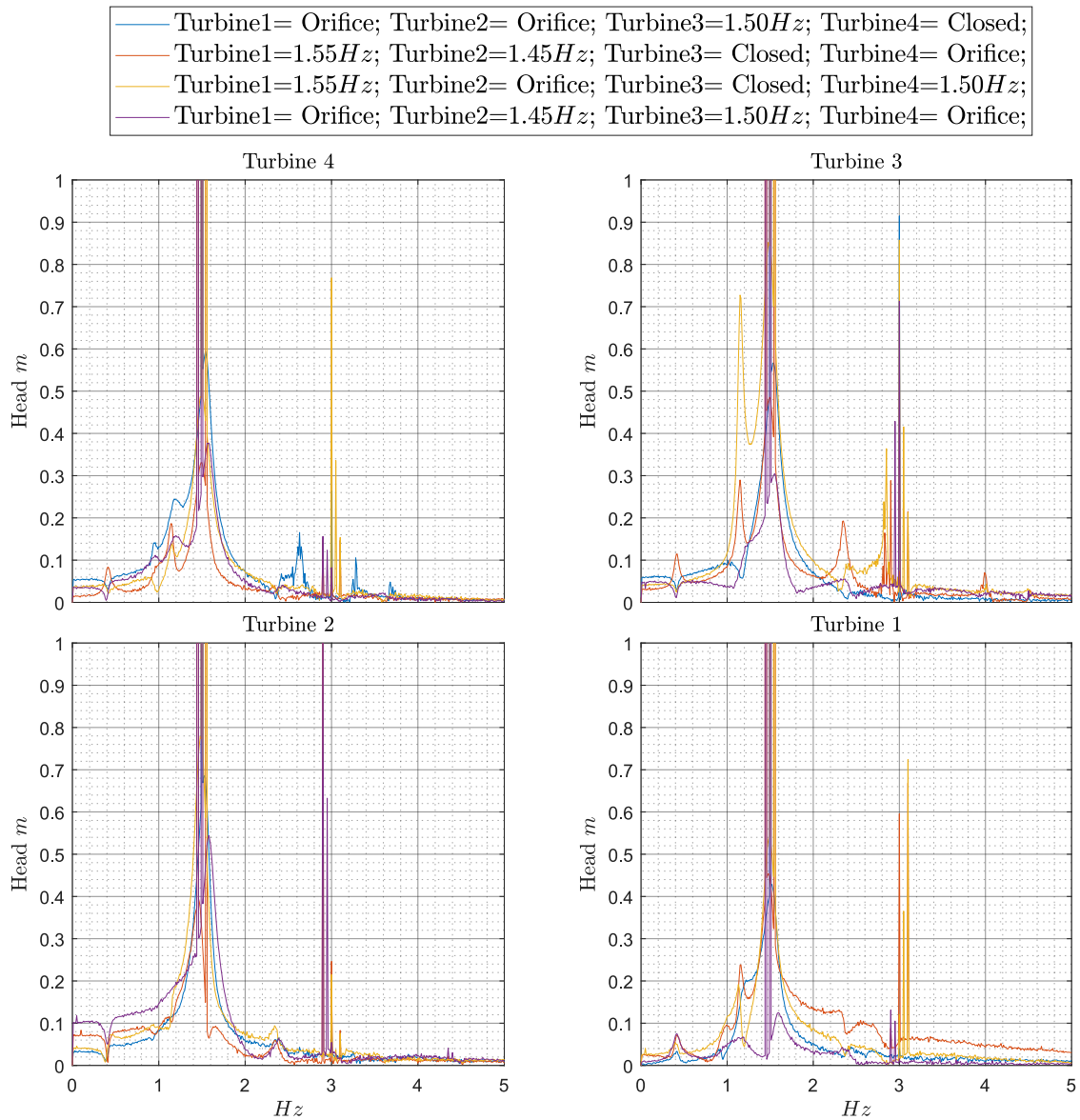


Figure 7.8: 4 cases simulated with a combination of closed bulb valves and excitation forces. Spectral analysis with low amplitudes

Figure 7.8 shows the same simulations as in Figure 7.7, but the y-axis is scaled down. Amplitudes related to frequencies around the first and second harmonic of the excitation force frequency dominate, but peaks related to other frequencies are also present. Turbine 1, 3, and 4 have a distinct peak around 1.2 Hz. Note that the peak has the same frequency for case 2 and 3 where turbine 3 is closed. The peaks are seemingly related to reflections at the turbine boundary. Figure 7.8 illustrates the complexity of the transients at the turbine boundaries and how amplitudes related to a wide range of frequencies occur.

7.2.4 Simulating With Different Wave-Speeds

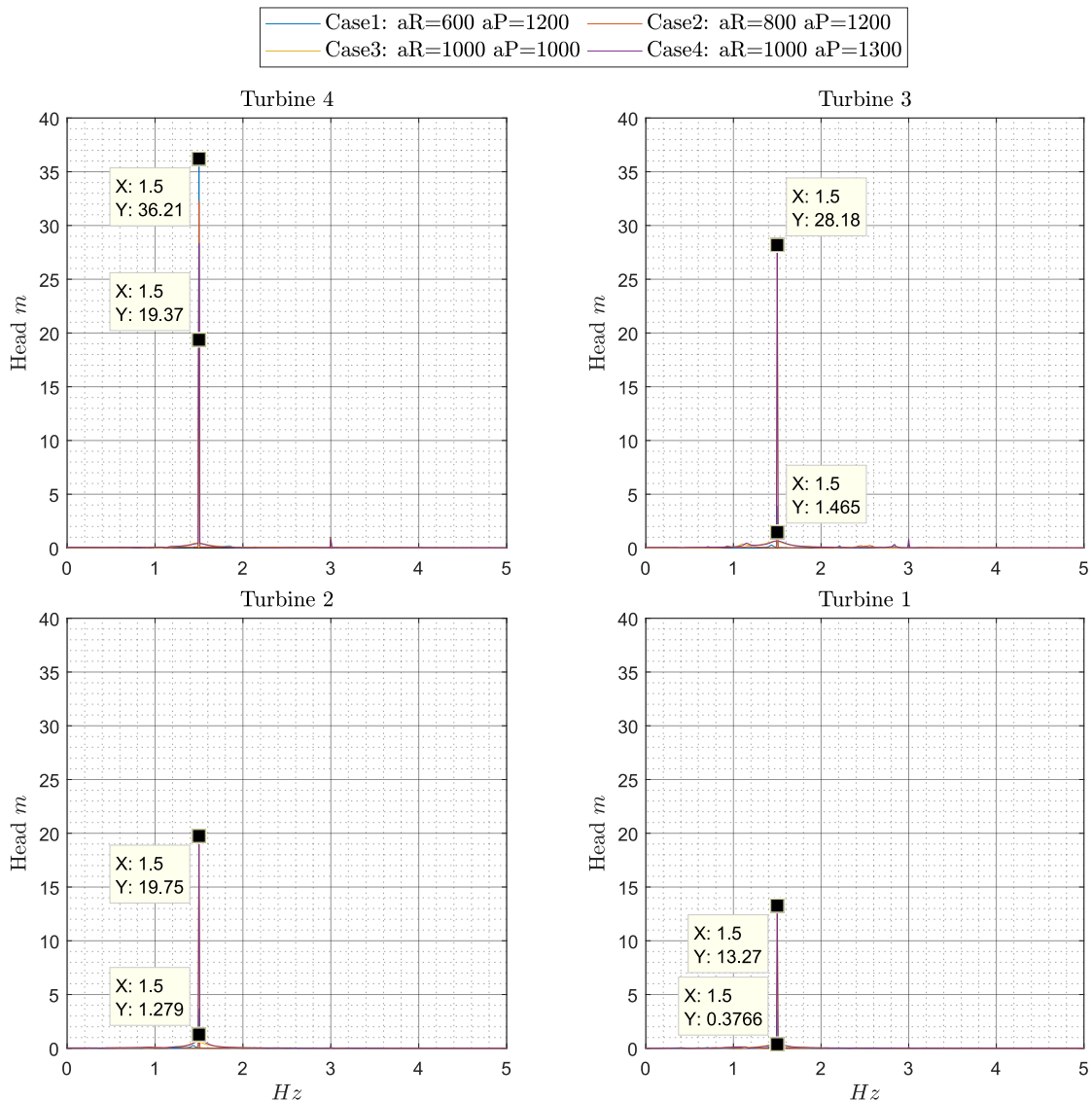


Figure 7.9: Spectral analysis of the simulation of measurement series 72-74 in the experimental results focusing on large amplitudes.

Figure 7.9 illustrates simulations where the wave-speeds are changed for every case. aR is the wave speed in all rock tunnel while aP is the wave speed in the steel penstocks. The configuration of aR and aP is found in the figure. All four simulations had the following turbine boundary conditions controlling the flow: **Turbine1=Orifice, Turbine2=Orifice, Turbine3=Closed and Turbine4=valve with sine function with a frequency of $1.5Hz$.**

Figure 7.9 shows that the amplitudes experienced at the turbine boundaries vary a lot with the propagation velocity. The frequency related to the highest amplitudes is constant and equal to the excitation force frequency at turbine boundary 4.

Case 4 is compelling since the largest amplitude in the spectral analysis at turbine boundary 3 is the same as the largest amplitude at turbine boundary 4. The amplitudes at the other turbines are also considerable and may indicate that resonance is occurring in parts of the system. It is natural to think that resonance occurs somewhere between turbine 3 and 4 since the magnitude of the peaks in the spectral analysis at these locations are almost identical.

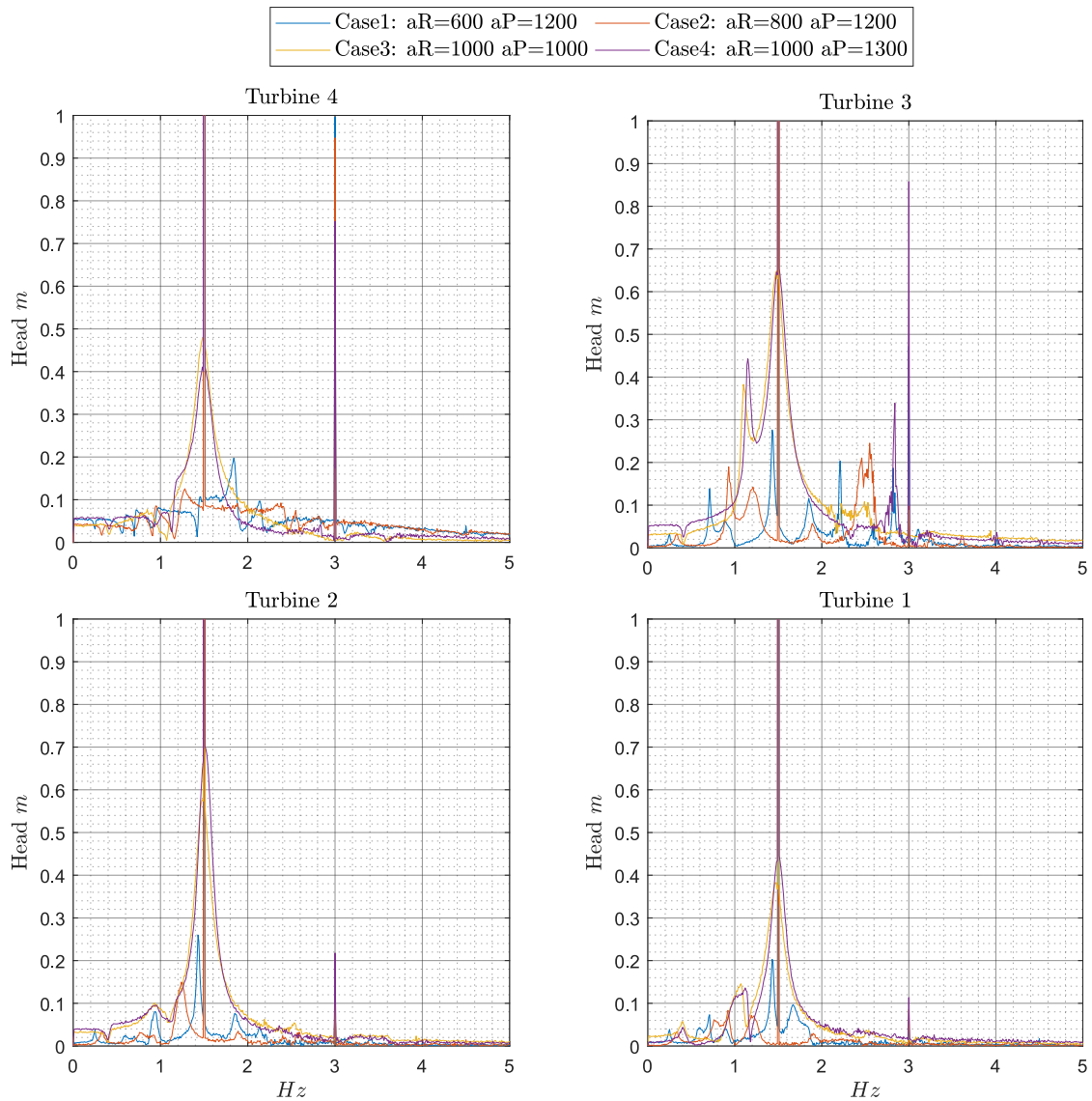


Figure 7.10: Spectral analysis of the simulation of measurement series 72-74 in the experimental results focusing on small amplitudes.

Figure 7.10 shows the same simulation as in figure 7.9 with a smaller range on the y-axis. Note that case 3 and 4, which yield the largest amplitudes for turbine 1, 2, and 3, have a relatively smooth transition from the surrounding amplitudes to the largest peak. Note also that case 3 and 4 have the same wave speed in the rock tunnels. The minor peaks in the spectral analysis vary a lot with the different wave-speed configurations. Note further that case 1 and 2 have the same

wave speed in the steel penstock. Based on the nature of the peaks in the plot, the peaks around the fundamental frequency of the penstock are most affected by the wave speed in the penstock. The wave speed in the rock tunnels seemingly governs the peaks around the excitation force frequency.

The fundamental frequency of the steel penstocks can be seen in figure 7.10 at turbine boundary 3 in case 4. The fundamental frequency with $aP = 1300 \text{ m/s}$ is 2.895 Hz .

7.3 Kvittdal hydropower plant

Chapter 5 illustrates and describes the experimental setup used during the experiments. Pictures of the pressure transducers are found in appendix D.

7.3.1 Seismic Interferometry

Seismic interferometry was applied to the measured data at Kvittdal. However, the results were inconclusive due to the noise level in the signals. The results are therefore not added.

7.3.2 Turbine Data and Pulsation Frequencies

Turbine data		
Runner blades	30	
Guide vanes	24	
Runner speed	333.33	<i>rpm</i>
Power	310	<i>MW</i>
Flow	62.2	<i>m³/s</i>

Table 7.1: Turbine data at Kvittdal from Giskehaug [16].

Pressure pulsation frequencies		
Rheinegans	1.4 – 1.88	<i>Hz</i>
Upper draft tube vortex	1.4 – 7.75	<i>Hz</i>
Runner unbalance	5.56	<i>Hz</i>
RSI	166.67	<i>Hz</i>
Guide vane passage	133.33	<i>Hz</i>
Splitter blade	83.35	<i>Hz</i>

Table 7.2: Approximations of the expected frequencies related to flow features in the turbines at Kvittdal.

Table 7.1 shows some of the main parameters governing pressure pulsating phenomena in the turbines at Kvittdal. Table 7.2 displays some of the frequencies related to phenomena discussed in the basic theory chapter. Vertical lines representing the frequencies have been plotted in spectral analysis plots together with the post-processed measured data. Examples of such plots are displayed later in this section and in appendix E.

7.3.3 Operational Loads and Waterway Configurations

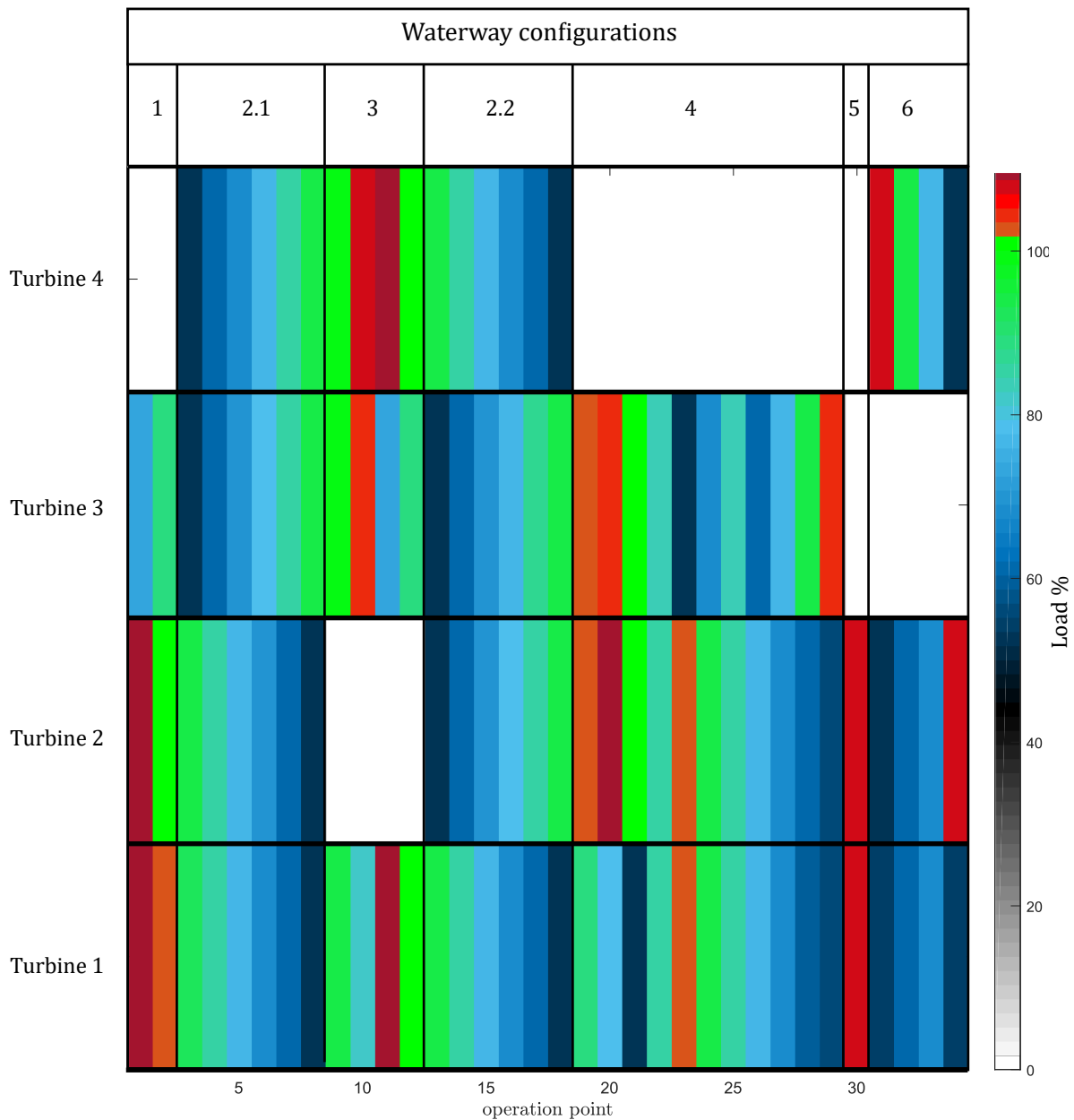


Figure 7.11: Operation points with different waterway configuration.

figure 7.11 shows the load related to each operation point together with the waterway configurations mentioned in chapter 6. The intention of the figure is to be used together with figure 7.12 and 7.14 to compare the spectral analysis in each measurement series with the load. Note that in waterway configuration 2.1 Turbine 1 & 2 and 3 & 4 are operated in pairs. In configuration 2.2 Turbine 1 & 4 and 2 & 3 are operated in pairs. Turbines operated under the same circumstances are comparable and will more likely uncover differences related to transients in the waterways if they exist.

7.3.4 RSI

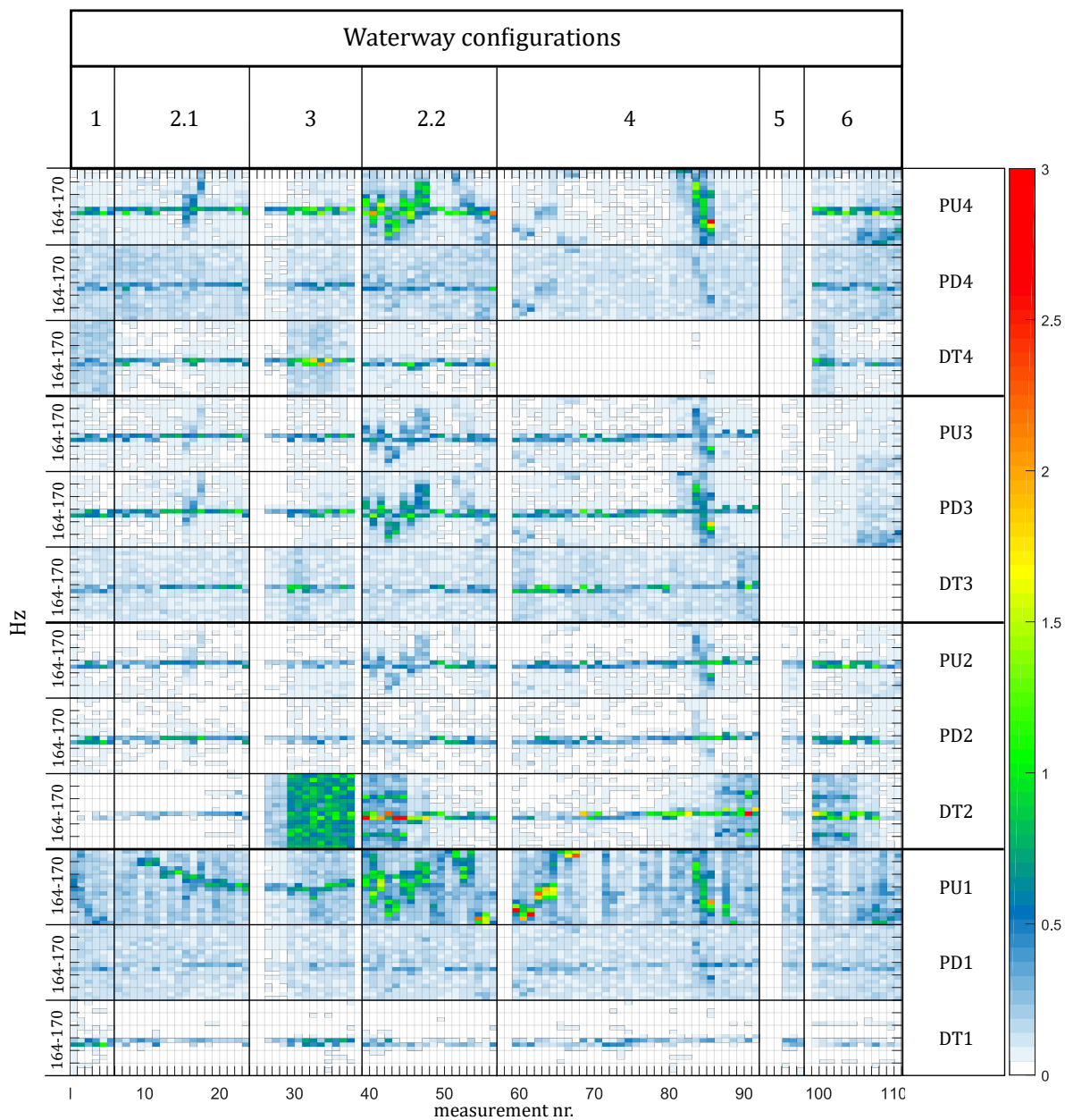


Figure 7.12: Spectral analysis in the range 164-170 Hz from all steady state measurements.

Figure 7.12 shows the maximum amplitudes in the spectral analysis with a frequency range of 164-170 Hz for all sensors during steady-state operation. The dynamic measurement series are set to zero and seen as vertical white lines. The amplitude scale is in kPa . Figure 7.11 can be used to compare the operation point load with the amplitudes.

The RSI frequency at Kvilldal is 166.67 Hz . In figure 7.12 all turbines show a distinct line around this frequency at some operation points, but the magnitude is small for measurements upstream the turbines. The RSI frequency is not noticeable upstream the closed bulb valves of Turbine 3 and 4, i.e., PU4 shows no distinct lines at the RSI frequency for waterway configuration 4 & 5, PU3 shows no distinct line for waterway configuration 5 & 6. High amplitudes are seemingly detected by sensor PU4 and PU1 several times. The amplitudes are, however, not coinciding with the amplitudes measured at PD1 and PD4 and therefore considered as noise. Increasing or decreasing the load does not affect the pressure pulsations related to RSI upstream the turbine. Pressure fluctuations related to RSI are expected to increase as a direct effect of decreasing the distance between the guide vanes and the impeller, as discussed in chapter 5.

7.3.5 Operation Load and Rheingans Frequency

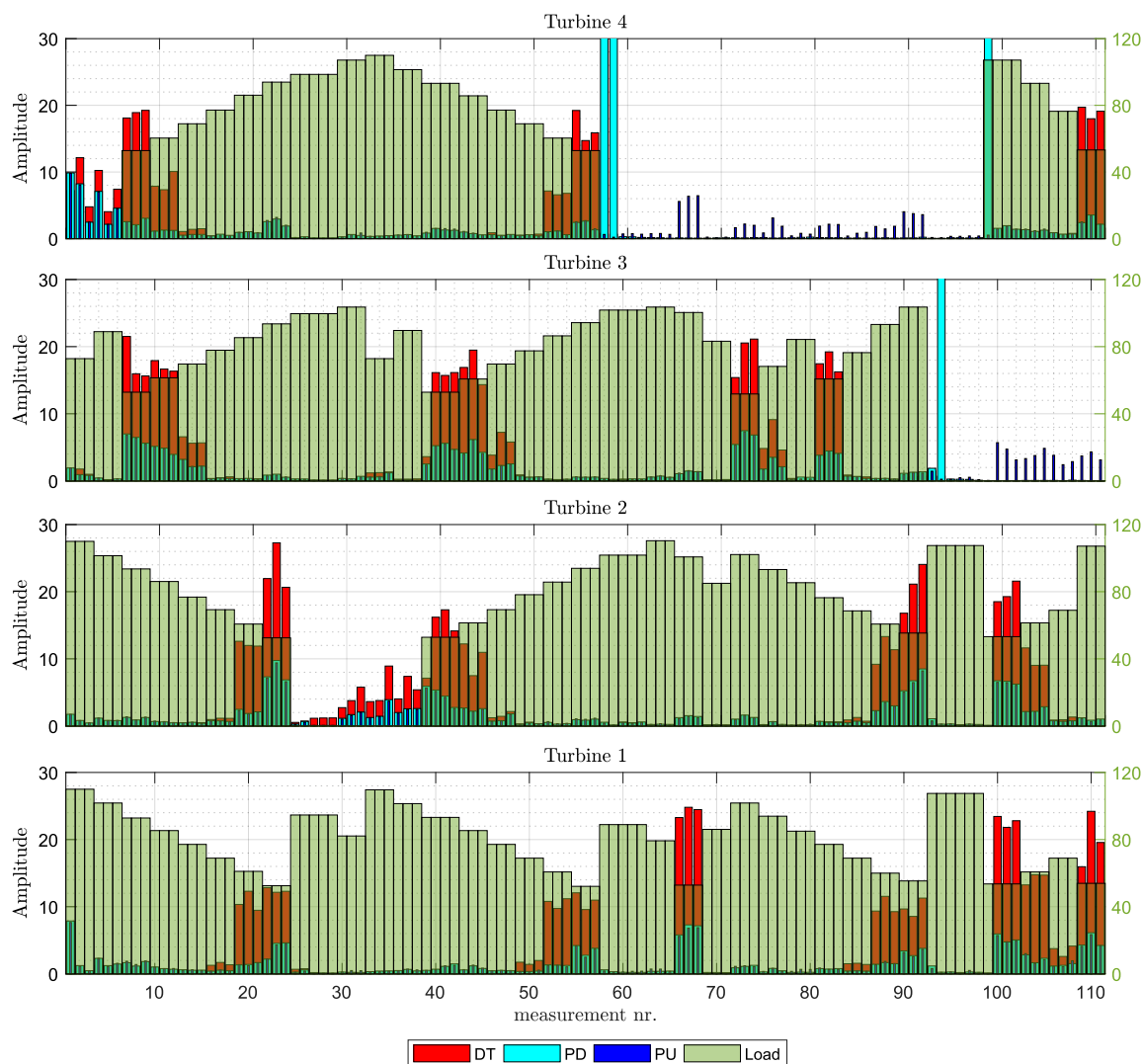


Figure 7.13: Max amplitude in the Rheingans frequency range, 1.45-1.55 Hz , together with the load for each measurement.

Figure 7.13 displays the maximum amplitudes from the spectral analysis, in the frequency range 1.45-1.55 Hz , for each measurement series. The range covers the expected Rheingans frequency [38]. The figure also include the loads from table 6.3 which is illustrated as a percentage of best point efficiency, 280 MW .

Note that PU3 and PU4 are showing substantial amplitudes even when the bulb valves are closed in front of turbine 3 and turbine 4. DT3 in measurement series nr. 76 show the highest amplitudes for a load larger than 60 %. The high PD peaks at measurement series nr. 58, 59, 94 and 99, are related to closing and opening of bulb valves.

Turbine 3 has the largest amplitudes when operated on 60 % and 70 % load. This can be seen in measurement series 10-15 and 43-48. The amplitudes at turbine 3 are comparable to, turbine

4 in series 10-15, and Turbine 2 in series 43-48, as they are operated with the same load.

Note that PU3 and all transducers at turbine 1 are measuring substantial amplitudes in measurement series 106-108. The magnitude of PU3 is surprising when compared to the operation points before and after where turbine 1, 2, and 4 are generating stronger pressure fluctuations. It is therefore suspected that resonance in relation to the penstock leading to turbine 3 is the cause of the large amplitudes recorded by PU3. Measurement series 84-86 have the same load distribution over three turbines as series 106-108 and seem to provoke less transients in the frequency range under examination.

7.3.6 Case 1. Waterway Configuration

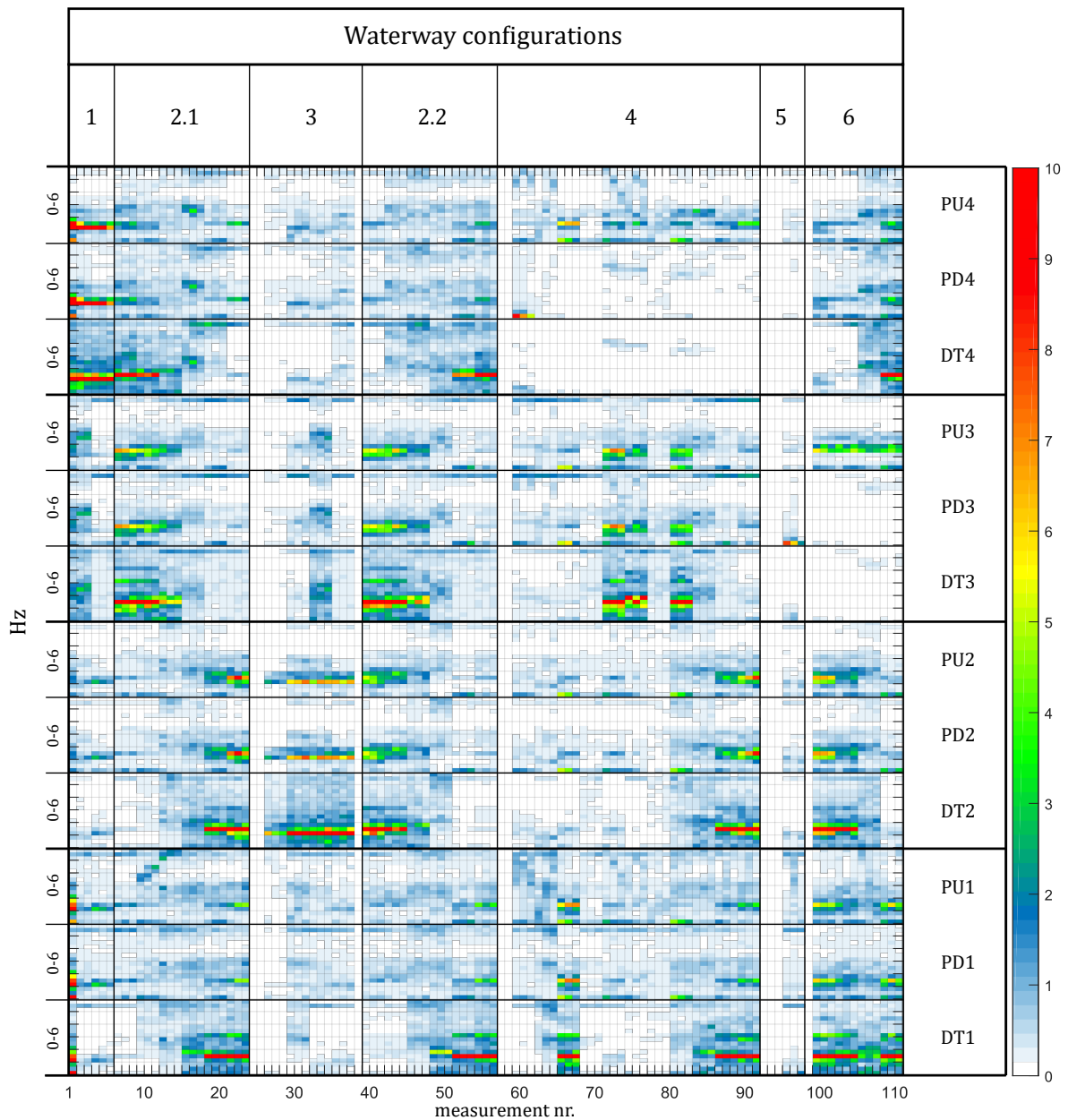


Figure 7.14: Case 1. Waterway configurations as described in table 6.1. Spectral analysis amplitudes of all sensors 0-6 Hz .

Figure 7.14 shows the spectral analysis from the steady-state measurements. It shows the magnitude of the maximum amplitudes in the frequency range 0-6 Hz for all the sensors. The resolution in the spectral analysis is 30 points per hertz, but the figure has a resolution of 3 points per hertz. Each point displays the maximum of the 10 point range it covers. The exact magnitude of the amplitudes are not the scope in these results but note that the magnitude is more than three times as high as in figure 7.12 where the RSI range was displayed. The axis of the colorbar is limited to 10 kPa , meaning that the red points can exceed this limit.

Observations Related to Waterway Configurations	
1	<p>Turbine 4: spin no load. The high amplitudes measured at turbine 4 are conducted while the turbine is in spin no load. In Measurement series 1 low-frequency amplitudes are present. Bringing turbine 4 to spin no load affects the dynamics of the system. It is interesting to note that turbine 1, 2, and 4 are experiencing significantly larger amplitudes than 3 in series 1.</p> <p>Figure 7.15 reveals the numbers related to each of the large amplitudes described over. The data points for PU1 and PD1 are not included in the figure, but the amplitude, (named index), in the figure is 3.218 kPa for PU1, 3.165 kPa for PD1, 2.758 kPa for PU2 and 2.746 kPa for PD2. X represents the measurement series nr. in figure 7.15.</p> <p>The frequency of the pressure fluctuations generated by turbine 4 during spin no load is lower than the frequency of the fluctuations caused by the part load surge in later measurement series.</p>
2.1	<p>Turbine 3 & 4 are operated from part load to full load while turbine 1 & 2 are operated from full load to part load. All the turbine experience pressure fluctuations with large amplitudes related to the part load surges. Turbine 3 has substantially larger amplitudes in the penstock for measurements 7-12, when compared with turbine 4. The large amplitudes may indicate that turbine 3 experiences higher stresses due to transients during the operation points. The same is true for turbine 2 when compared to turbine 1 in measurement series 19-24.</p>
3	<p>Turbine 2 spin no load: The operation of the other turbines while holding turbine 2 at spin no load are not below 80 % of best point efficiency. PU2, PD2 and DT2 measure high amplitudes related to slightly lower frequencies than the ones occurring during part load, (The red line moves down one increment in the figure). The behavior is the same as what turbine 4 experiences in waterway configuration 1.</p> <p>Measurement series 32 is added to give numbers to the amplitudes in figure 7.15. Comparing the amplitude magnitudes is questionable due to uncertainties which are mentioned in chapter 5, but from figure 7.14 and figure 7.15 it seems to be better to operate turbine 2 at spin no load rather than turbine 4.</p>

Observations Related to Waterway Configurations	
2.2	<p>Turbine 3 & 2 are operated from part load to full load while turbine 1 & 4 are operated with the opposite trend. The behavior of the two first turbines are almost identical, but PU3 and PD3 measure slightly higher amplitudes in all the measurements. The frequencies of the amplitudes in the penstock connected to turbine 3 also seem to be more constant while the frequencies related to the highest amplitudes in penstock 2 are smeared out. Transients in the system might cause these differences. DT3 shows higher amplitudes for measurement series 43-48, which might indicate that the draft tube surges occur in a broader load range in turbine 3 compared to turbine 2.</p> <p>Turbine 4 & 1 are operated from full load to part load. It is interesting to note that the highest amplitudes measured by DT1 experience a frequency shift as turbine 1 approach part load. The phenomenon happens between measurement series 18-19, 51-52, and 86-87. The higher frequency might be due to the upper part load vortex phenomena, which have a higher frequency than the part load vortex.</p>
4	<p>Turbine 4. closed bulb valve: Note that PU1 and PD1 are experiencing the highest amplitudes during measurement series nr. 66-68. During these series, the trend of the measurements at PU4 is identical to PU1 and PD1. Based on the latter, transients traveling between the bulb valve at turbine 4 and turbine 1 seem likely. Surprisingly, the amplitudes at PU4 decrease in measurement series 72-74 where turbine 3 and 1 switch the operational load. Turbine 3 is closer to turbine 4, so frictional losses should be smaller. Figure 7.15 presents measurement series 68 and 73 to show the actual difference in magnitude of the amplitudes in the spectral analysis. The data point for PU4 during measurement 73 lacks in the figure, but the index is 2.193 kPa for $X = 72$ & $Y = 14$.</p>
5	<p>Turbine 4 & 3. closed Bulb valves: The measurements conducted at this operation point have very small amplitudes and show that the turbines cause little pressure fluctuations while operated close to best point.</p>
6	<p>Turbine 3. closed bulb valve: The amplitudes in the measurements at PU3 show that transients from turbine 1, 2 and 4 affect the pressure fluctuations in the penstock of turbine 3. PU and PD at turbine 2 show larger amplitudes than the ones measured at turbine 4 & 1.</p> <p>Note again that PU3 shows surprisingly high amplitudes for measurements 106-108. This was also addressed in the results related to figure 7.13.</p>

Table 7.3: Notes related to different waterway configurations in figure 7.14.

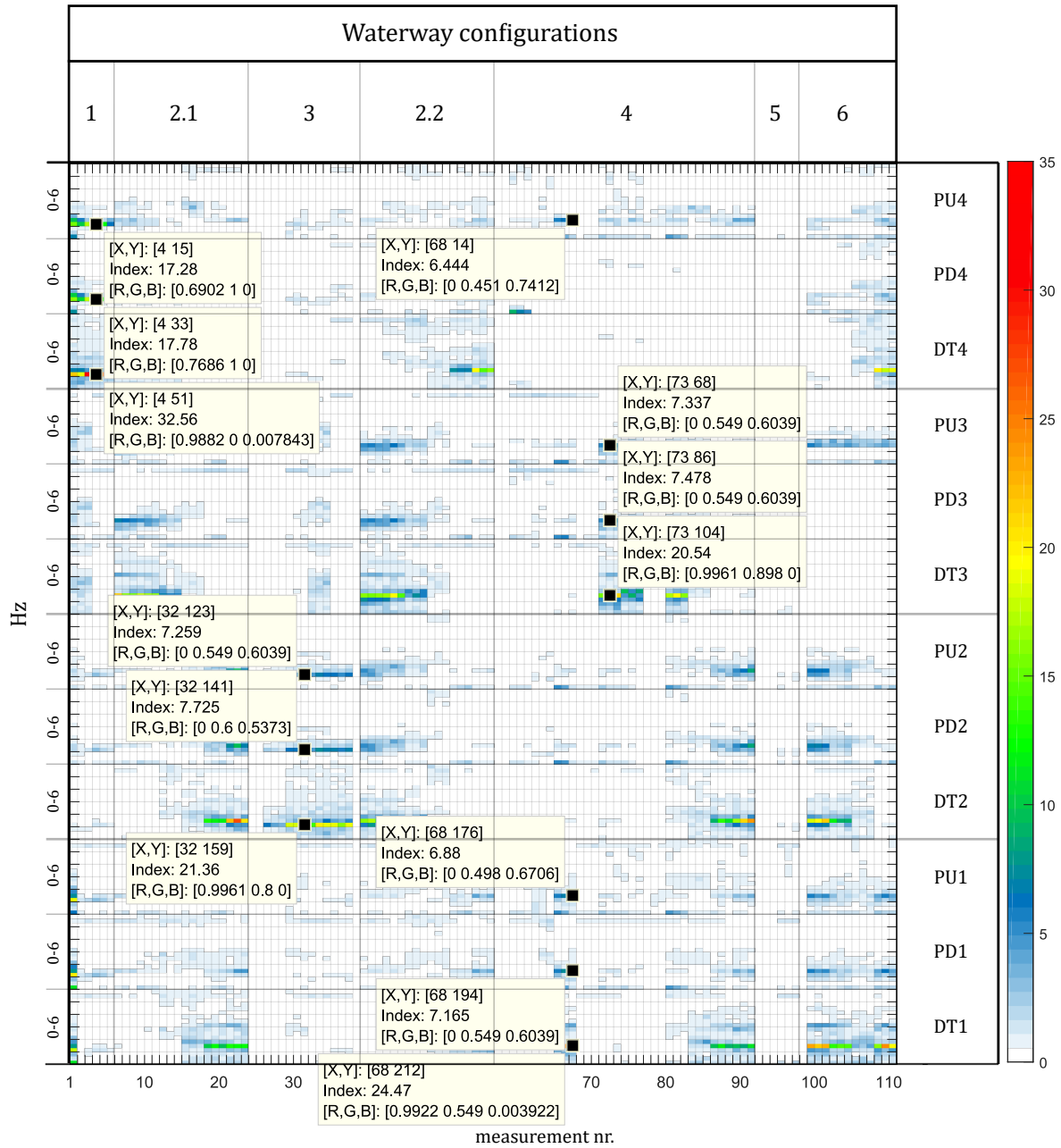


Figure 7.15: Case 1. Some highlighted measurement series from Case 1.

7.3.7 Case 2. Transient Events

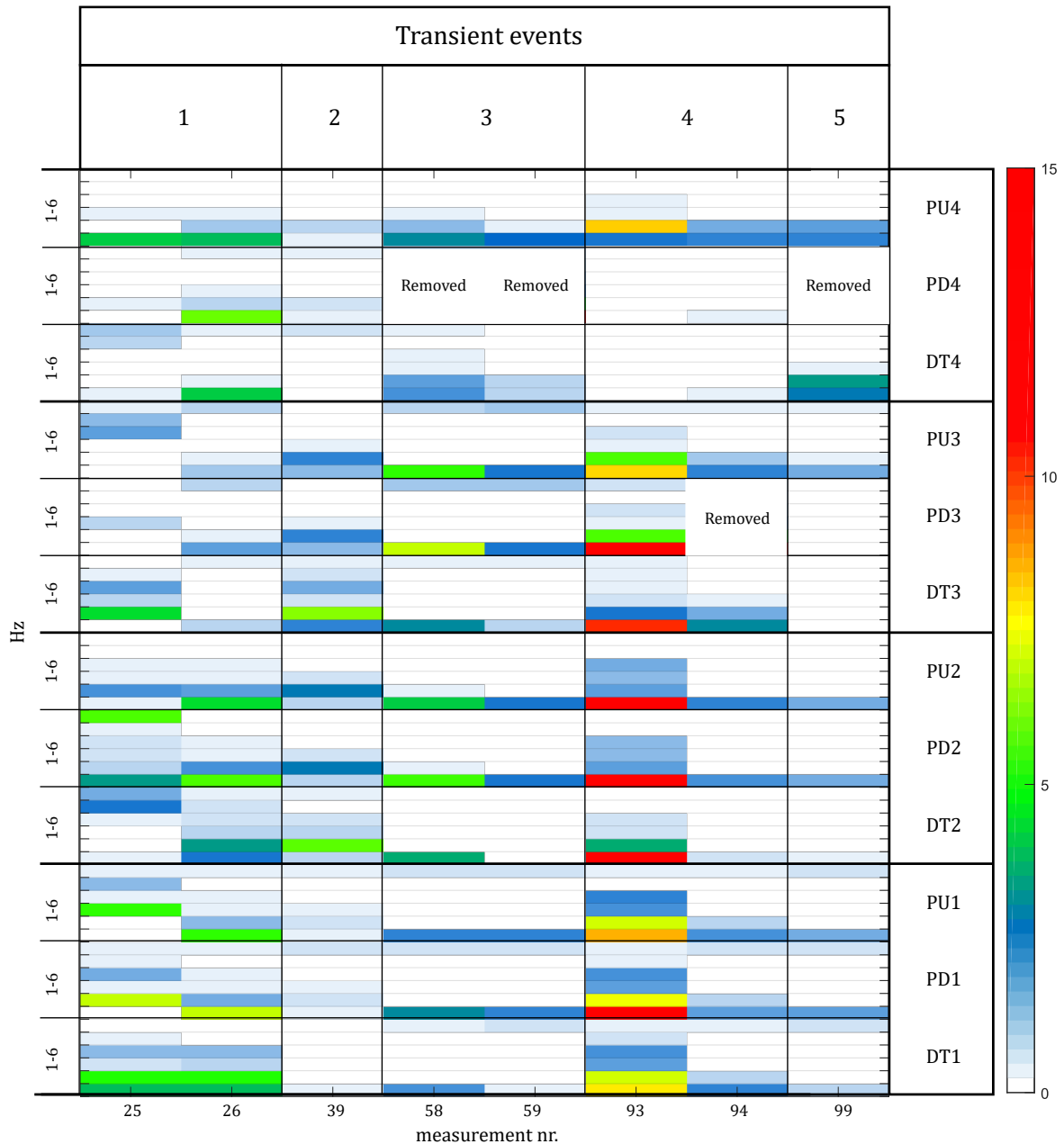


Figure 7.16: Case 2. Transient measurements. Spectral analysis of of transient measurements for all sensors in the range 0-6 Hz .

Figure 7.16 compares results from the spectral analysis conducted at all the sensors during dynamic events such as closing and opening of bulb valves. The results show the maximum amplitudes in the 0-6 Hz frequency range with a resolution of 1 Hz . Each 1 Hz range represents the maximum from a spectral analysis with a much higher resolution. From the 8 measurement series, nr. 93 stands out by showing large amplitudes in both the 0-1 and 1-2 Hz range. PU4, PU1, and PD1 show the largest amplitudes in the 1-2 Hz range, which indicates that there are transients in the system. Measurement nr. 93 was chosen to be investigated further based on the latter statement.

Measurement 93

Measurement series 93 took place while transferring from operation point 29 to 30, found in table 6.3. The load on Turbine 1 and 2 increased from part load to full load while the load on turbine 3 decreased from full load to part load. As mentioned in chapter 6, only two turbines could change the load at the same time. Turbine 1 and 3 changed load simultaneously, before turbine 2. A lot of noise and vibrations were present in the power plant during the measurements, as also seen in the data.

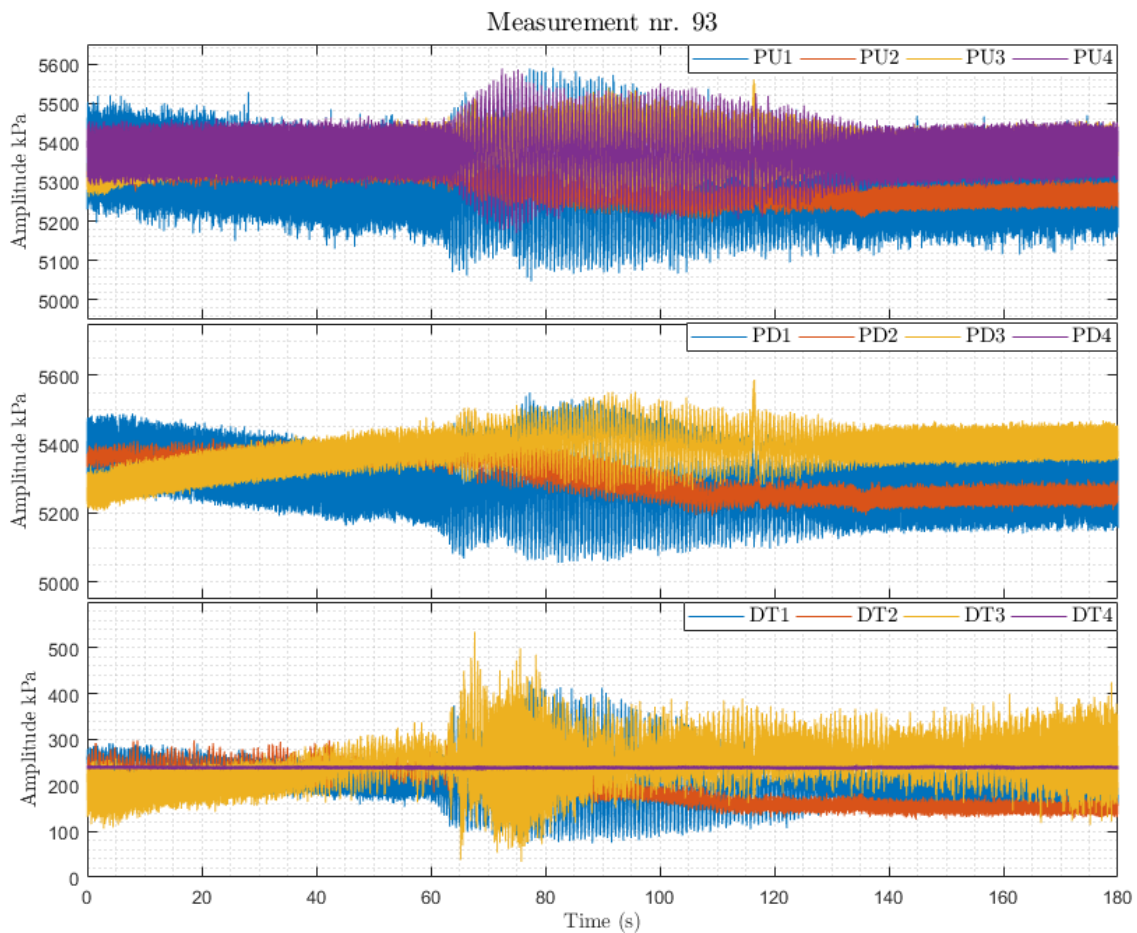


Figure 7.17: Measurement series 93.

Figure 7.17 shows the plotted raw data from the measurement. The sensors from all four turbines are plotted together for each sensor position for comparison. The measurements include much noise, which resulted in the application of a low pass filter to clarify the information in the signal. PD4 is not present since the bulb valve is closed in front of turbine 4 and the pressure is outside the range in the plot.

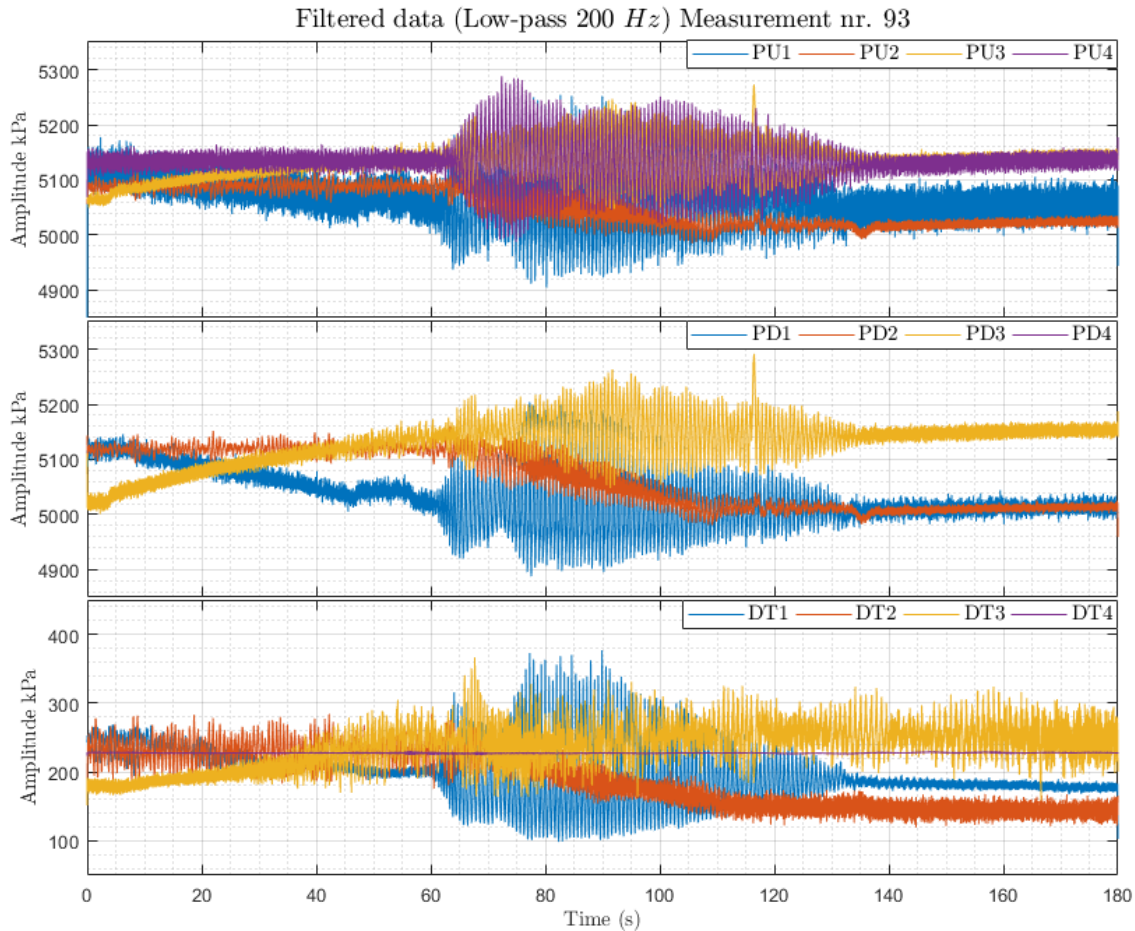


Figure 7.18: Measurement series 93 filtered.

Figure 7.18 shows the same data as previously shown in figure 7.17 with a low pass filter. The plot clearly shows how the pressure in front of turbine 1 and 3 responds to the load change first, followed by a pressure drop in front of turbine 2 as the load increases.

In figure 7.18 it seems that resonance in the waterway system is first provoked by turbine 3 in the draft tube as it approaches part load. Around $t = 40s$ DT3 shows increased pressure fluctuations, which propagate and seem to excite fluctuations at turbine 1 where the largest amplitudes start at around $t = 62.5s$. Fluctuations in the draft tube of turbine 2 are present before the excitation of DT3 and might be a contributing factor. The large fluctuations at turbine 4 and 3, (PU4 & PU3), seem to start increasing at approximately the same time ($t = 65s$), but turbine 3 decreases again after a couple of seconds while the fluctuations at the bulb valve continue to increase until $t = 73s$. Turbine 2 is also experiencing fluctuations, seen at (PU2 & PD2), but not nearly as violent as the other three turbines. After turbine 4 has reached its maximum amplitude at $t = 73s$, the amplitude decreases slowly while the amplitude of the fluctuations at turbine 1 increase again. PU1, PD1 and DT1 measure the largest fluctuations between $t = 77s$ and $t = 90s$. The amplitude of the fluctuations measured at turbine 3 shows maximum values around $t = 90s$. Note also that there is a large spike measured in front of turbine 3 after approximately $t = 117$, (PU3 & PD3). Turbine 2 also alters behavior around the same time, (PU2 & PD2).

The difference between the mounting of pressure sensors in the draft tubes should be kept in mind while analyzing the data. Pictures of the sensors are found in appendix D. In general the sensors upstream the turbines are considered more comparable since they have almost identical mounting, this is also true for DT1 and DT3 in the draft tubes.

Further investigation of measurement 93 is performed through spectral analysis of the entire signal. The spectral analysis of all the sensors is illustrated in figure 7.19 and 7.20. The dashed blue line at 1.5 Hz represent the expected Rheingans frequency.

Figure 7.19 shows the spectral analysis of turbine 4 & 3 during measurement 93. Turbine 4 has a closed bulb valve and amplitudes only occur at PU4. The fft shows two peaks close to each other, one at 1.5 Hz , the other is slightly under. PU3 and PD3 show the same two peaks, but with smaller amplitudes.

Figure 7.20 shows the spectral analysis of turbine 2 & 1 during measurement 93. PU2 and PD2 show amplitudes slightly over 1.5 Hz and slightly under. DT2 has a distinct peak slightly over 1.5 Hz . PU1, PD1 and DT1 have peaks in at the same frequencies with almost identical amplitudes. The frequencies related to the largest peaks are the same as for turbine 4 & 3, and differ slightly from the peaks observed at turbine 2.

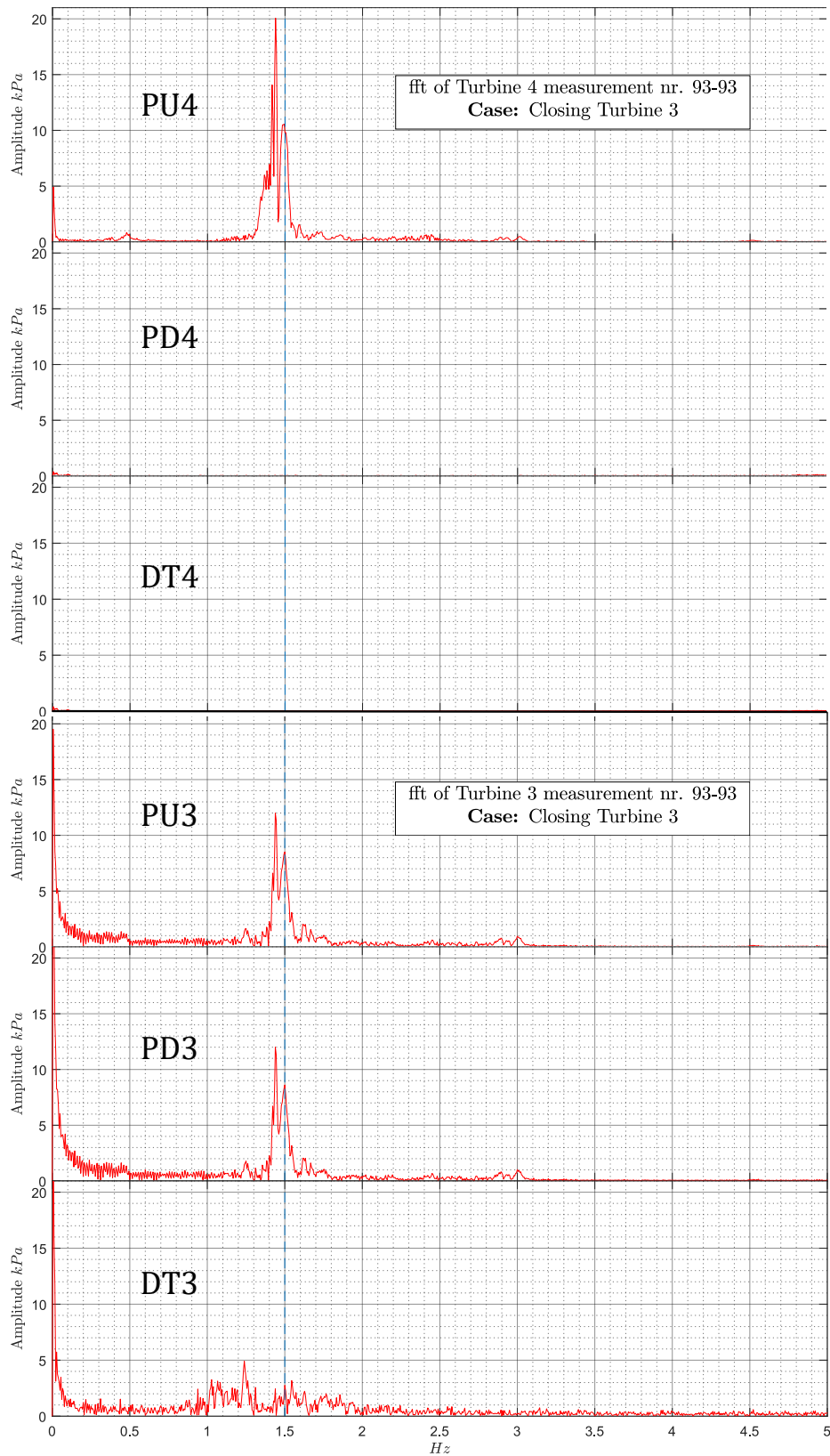


Figure 7.19: Spectral analysis of measurement 93, Turbine 4 & 3

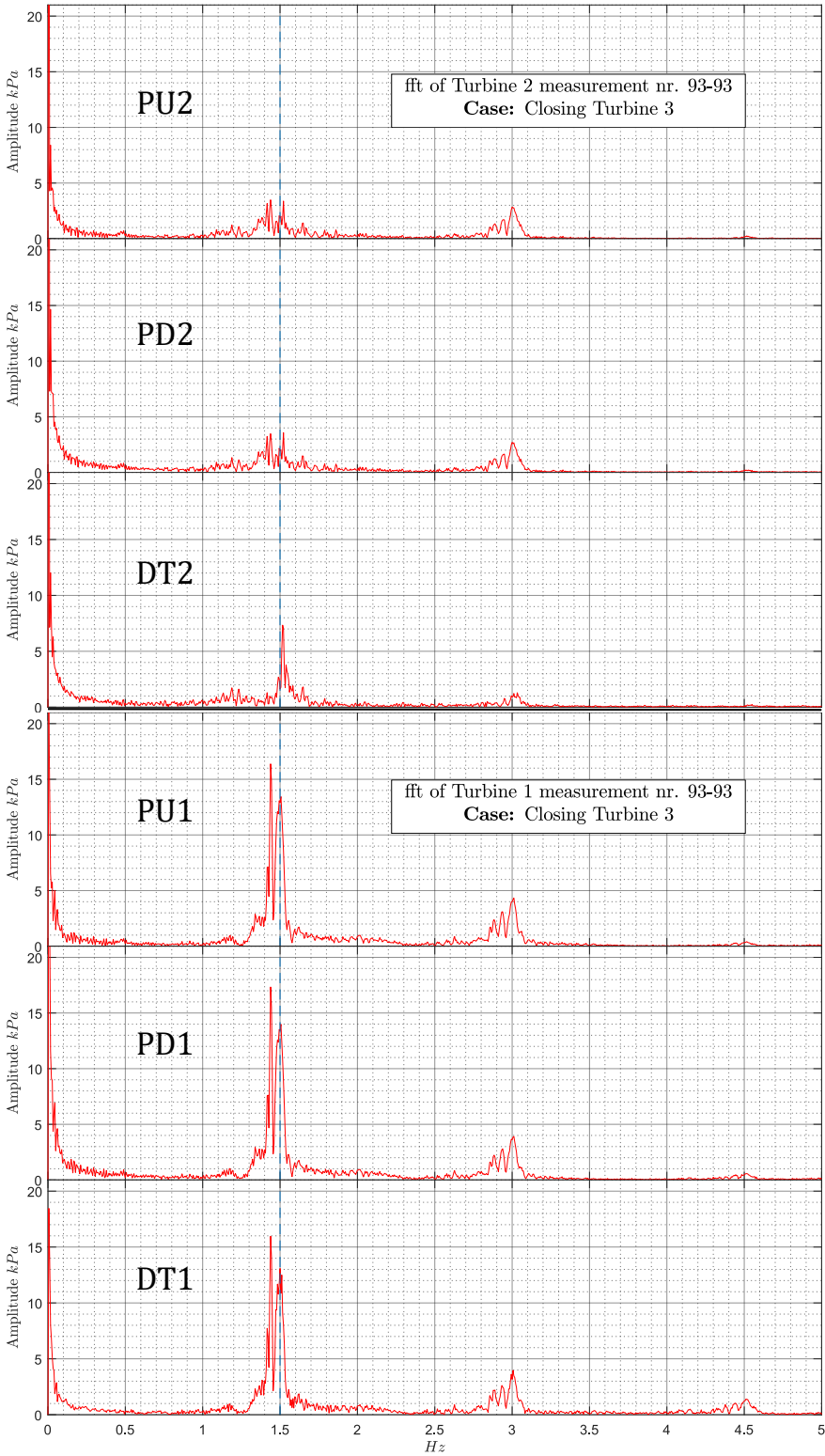


Figure 7.20: Spectral analysis of measurement 93, Turbine 2 & 1.

Discussion

8.1 Hydropower Laboratory Seismic Interferometry and Deconvolution Interferometry

8.1.1 Simulated Data

Figure 7.1 illustrates seismic interferometry also called cross-correlation interferometry applied to simulated data with a known propagation velocity of 1000 m/s. The figure shows that it is difficult to draw certain conclusions about the wave speed when the elastic waves are excited by a complex function. Figure 7.2 represents deconvolution interferometry applied to the same data. The most significant response peaks align on the dotted gradient line representing a wave speed of 1000 m/s. As presented in the basic theory chapter, deconvolution interferometry may be a better post-processing technique for complex excitation forces. Note also that the peaks in the negative time domain disappear when the technique is applied.

8.1.2 Measured Data

Figure 7.3 and figure 7.4 show the result of applying cross-correlation interferometry and deconvolution interferometry to the same measured data. The results have many similarities with the simulated data. The largest response peaks align on the dotted red line which is fitted manually by trial and error. The fitted line corresponds to a wave speed of 945 m/s. The wave speed is substantially lower than the expected theoretical wave speed, which is stated in chapter 3 to be 1200-1400 m/s. As presented in the paper in appendix F, a possible explanation for the reduction in speed is the presence of a small amount of air. As seen in figure 3.16, the velocity is highly dependent on the amount of air in the system. The penstock in the Hydropower Laboratory should be more sensitive to the presence of air since the pressure is relatively low.

It should also be mentioned that the spectral analysis of the recessed transducers (IN1-IN3) gave unnaturally high amplitudes for high frequencies, ($f > 50Hz$), when compared to the flush mounted sensors. Post-processing of the data from the recessed sensors was, therefore, done with a band-pass filter with a lower upper band than the flush mounted sensors. Limiting the upper band increases the possibility for merging peaks, which alter the results. As mentioned in chapter 5, a dynamic calibration of the sensors was challenging to conduct. In

general, flush mounted sensors are the best solution to avoid the problems mentioned above.

Further discussion regarding the Laboratory measurements is found in the paper in appendix F.

8.2 Kvilldal Hydropower Plant

Seismic Interferometry

Application of Seismic interferometry to post-process the measurements at Kvilldal showed inconclusive results. The level of noise vs. signal in the measurements is too high for the method to work in the same manner as in the hydropower laboratory. The method might work if the measured data are treated to remove the noise more efficiently. It could also be interesting to look at sensors in front of different turbines and investigate low-frequency amplitudes instead of higher amplitudes in the RSI range. The small distance between the sensors upstream the turbines at Kvilldal restricts the lower end of the frequency range since the wavelengths related to low frequencies are much longer than the distance between the transducers.

8.2.1 Simulations

One of the most surprising observations from the spectral analysis of the numerical simulations is that amplitudes at the exact fundamental frequency of pipe sections and sections between reflection points seldom occur. The spectral analysis also often shows the opposite of what one would expect, meaning that the amplitude is almost equal to zero for the fundamental frequency of pipe sections. One hypothesis for the low amplitudes is that traveling waves in the system with a lower fundamental frequency cancel out the standing waves in the separate pipe sections. However, this it is only a speculation based on observations from the transient plot.

The primary purpose of the simulation model is to find trends in how transients propagate in a complex conduit and which factors that affect them the most. The simulation of numerous cases has made it evident that the behavior of transients are difficult to understand intuitively.

Note also that the validation of the numerical model is not ideal, and it is advised to compare the model with other one dimensional tools such as LVtrans or SIMSEN before further use. However, the results from the model are considered viable for its primary purpose based on the following: **1)** The characteristics method is well established and validated against multiple examples, as mentioned in previous chapters. **2)** Some validation and verification of the model is conducted, as presented in chapter 4.

8.2.2 Measurements

RSI

The magnitude of the amplitudes related to RSI in the spectral analysis is small compared to low-frequency phenomena such as the ones related to the draft tube surges. Small amplitudes

combined with long tunnels and high pressure are most likely the reasons why transients generated by RSI are undetected upstream the closed bulb valves of turbine 3 and 4. However, the RSI frequency is much higher than the draft tube surges, and high cycle frequency loads may cause fatigue, even with a smaller amplitude, as discussed in chapter 3. Nevertheless, the notion in this thesis is that transients in the penstocks related to RSI are unlikely to contribute to fatigue at Kvilldal since the amplitudes are hardly noticeable.

Note, RSI is likely to be the reason for the cracks on runner 3 at Kvilldal, but transients in the penstock caused by RSI are seemingly not a contributing factor, based on the results from the measurements. It would be easier to conclude with certainty if the measurements were conducted with dynamic, flush mounted, pressure transducers, which are more suited for dynamic measurements.

Operation Load and Rheingans Frequency

From the results related to figure 7.13, it seems interesting to further investigate the highlighted measurement series. One option is to compare measurement series 106-108 where turbine 3 is closed, with 84-86 where turbine 4 is closed. The variety between the cases is not surprising since closing turbines results in various waterways. New reflection points alter the dynamics of the system as experienced in the simulated model. Further investigation can consist of plotting raw data and performing spectral analysis. Looking at the complete spectral analysis rather than just a range gives another dimension to the actual difference between the operation points.

Case 1. Waterway Configuration

Figure 7.14 gives much information, and only the parts mentioned in the result part are discussed in this subsection. These observations are what was found most interesting while examining the figure.

PU3 and PD3 measured the apparently highest pressure fluctuations with a frequency of around 5.56 Hz , which result in the line seen in figure 7.14. 5.56 Hz is the runner's rotational frequency, and the amplitude of these fluctuations are small. The penstock connected to turbine 3 is, however, where fluctuations with this frequency are most dominant. Runner unbalance often causes fluctuations in this range [9]. The peak in the spectral analysis seems to disappear when turbine 3 operates on part load, and low-frequency pressure fluctuations are present. A possible hypothesis for the latter is that the pressure fluctuations created by the draft tube surge interfere with the systematic unbalance in the runner.

When all turbines are running, it is recommended to rather operate turbine 1 or 4 at part load rather than turbine 2 or 3 based on maximum measured pressure fluctuations upstream the turbines in figure 7.14. However, further investigation of the amplitudes related to pressure fluctuations in the draft tubes is needed. The amplitudes in the spectral analysis obtained in the draft tubes during part load are higher than 10 kPa , which is the maximum limit in figure 7.14. Figure 7.15 shows one approach for how to investigate details concerning magnitudes of peaks with amplitudes above 10 kPa .

Based on figure 7.15 it is better to operate turbine 2 on spin no load compared to turbine 4. Turbine 2 seemingly generates fewer transients, which should result in less stress on structural components. Figure 7.15 also seemingly shows that it is better to operate turbine 3 on part load compared to turbine 1 when the bulb valve in front of turbine 4 is closed. Nonetheless, the events should be repeated before any conclusions can be made.

Turbine 3 should not be operated below 70 % of best efficiency load. The recommendation is based on the large amplitudes experienced in the draft tube below this load (Measurements 46-48, table 6.3).

Case 2. Transient Events

Figure 7.17 and 7.18 show how the pressure decreases in front of turbine 1 as the load increases while the pressure increases in front of turbine 3 as the load decreases. The pressure waves are expected to propagate from turbine 1 and 3 up to the junctions and then interact with each other and with the fluctuations from the part load surge at turbine 2. Adding in the reflection points at the closed bulb valve at turbine 4, the blind tunnel and the reservoir, together with the uncertainty of the propagation velocity, make this a complex scenario. Finding the exact location where resonance occurs and understanding how it originates are challenging.

Figure 7.19 and 7.20 show the spectral analysis of the entire signal obtained during measurement 93. The amplitudes in these plots show a relation between turbine 1, 3 and 4 as the largest amplitudes are related to a frequency slightly under 1.5 Hz. The amplitude is only present in the draft tube of turbine 1 which makes it likely to be excited there. Turbine 2 stands out by having small amplitudes in the penstock, a possible theory is that the part load surge in the draft tube of turbine 2 cancels out the transients in the penstock. Further investigation of the measurement should be conducted to conclude more precisely since the nature of events are changing during the 180s recording.

It is interesting that resonance seems to occur in the draft tube of turbine 1 as it approaches full load. Even if it is not likely, the large fluctuations might indicate that the less common event of a full load cavitating vortex is occurring in the draft tube of turbine 1 as described in chapter 3.

Figure 7.18 illustrates the filtered raw data of measurement series 93. It shows a significant spike in pressure measured by PU3 and PD3, around $t = 117s$. The spike is seemingly related to transients in the upstream water system since the spike is unnoticeable in the draft tube.

Lastly, it should be mentioned that the operation of the turbines during measurement 93 is not a recommended way to operate turbines in a hydropower plant with reaction turbines and a complex system. Statkraft has routines for how to shut down and start up the turbines at Kvitvold to avoid such scenarios.

Planning and Implementation of the Fieldwork

The general plan for how to distribute the loads at Kvilldal was developed weeks in advance. However, the final restrictions related to the total effect produced hourly from the four turbines were unknown before the day of the fieldwork. The final development of the plan happened on the day of the measurements in the hour prior to start. Some adjustments were also made during the fieldwork, based on observations in the acquired data. After analyzing the data, the general conception is that the measurements have provided much interesting information. The results could have been even better by testing the repeatability of the most eventful measurement series. It would also have been beneficial to run all turbines on part load, one at the time, while the same bulb valve was closed to compare the transients created in the penstocks. In waterway configuration 4, turbine 2 is the only turbine that is not operated on part load separately. Nevertheless, the main goal was to investigate transients related to RSI, so that is part of the reason why part load operation points had less importance in the planning.

As mentioned earlier, the measurement equipment and mounting of transducers were not ideal. However, the measurements of pressure fluctuations with lower frequencies are considered to be satisfactory. Dynamic, flush mounted pressure sensors would reduce the uncertainties related to the measurements of pressure fluctuations related to RSI, and is therefore recommended. This equipment would have been used at Kvilldal, but it was impossible to implement due to the circumstances.

Conclusion

The thesis aims to investigate transients in waterways connected to high head Francis turbines. The measurements conducted at Kvilldal hydropower plant gave valuable information about the behavior of transients in the intricate waterways connected to the four high head Francis turbines. The planning before the fieldwork mainly consisted of finding possible locations for pressure transducers and how to operate the individual turbines during the measurements. Two pressure transducers were placed upstream each turbine, and one on each draft tube cone. The operation of turbines during the measurements focused on producing proper reference measurements, while the combined effect from all turbines matched the required effect set by the power plant owner. By operating two turbines with the same load, the turbines should have the same operating conditions. Measurements from these turbines are, therefore, more comparable in terms of finding individual differences related to transients.

The post-processing techniques applied to the measurements at Kvilldal gave a good overview of pressure fluctuations occurring during different loads. The frequencies with the highest amplitudes were related to draft tube surges at part load. The surges created transients in the waterways which were detected by pressure sensors upstream closed bulb valves during several operational configurations. These observations made it safe to conclude that low-frequency surges generated at a turbine may propagate throughout the entire system and affect the inlet conditions of other turbines.

Measurements did unveil transients related to the RSI frequency in front of turbines in operation. However, the amplitudes of the peaks in the spectral analysis related to the phenomenon were small. No transients related to RSI were measured upstream the closed bulb valves. The conclusion is that RSI related transients generated by one turbine do not affect the inlet conditions of other turbines at Kvilldal.

A one dimensional model of the waterway system upstream the turbines at Kvilldal and the penstock in the Hydropower Laboratory at NTNU was developed, using the characteristics method. The models have limitations due to the assumptions and implementation. Using the method of characteristics for exact modeling of a complex system like the waterways at Kvilldal is questionable due to uncertainties such as the propagation velocity in rock tunnels, reflection points, and geometry. The model can, however, indicate trends and give helpful visualization of traveling and standing pressure waves in the system. The blind tunnel length at Kvilldal is found to

have a considerable effect in the spectral analysis conducted at turbine boundaries in the model. Peaks in the spectral analysis are also found sensitive to changes in the propagation velocity, the frequency and magnitude of excitation forces, and reflection points like closed bulb valves. The spectral analysis of the measured data should also be sensitive to these factors.

Resonance condition was observed at Kvilldal when the load on several turbines was changed. The measurement with the most significant pressure amplitudes came from the draft tube of a turbine whose operating point moved, from part load to full load. Some recommendations were given to minimize the pressure pulsations at the inlet of the turbines. The recommendations consist of a wise choice of operating configurations of the turbines.

The wave speed in the penstock at the Hydropower laboratory was found by applying Seismic interferometry and deconvolution interferometry as post-processing techniques. The results prove that the methods can be used to detect the propagation velocity in a penstock containing elastic waves generated by a model Francis turbine during steady operation. It is recommended to use flush mounted transducers since they remove many uncertainties related to dynamic pressure measurements. The pressure data obtained at Kvilldal hydropower plant did not unveil the propagation velocity due to the level of noise in the signals. The wave speed found in the penstock at the Hydropower Laboratory was considerably lower than the expected theoretical propagation velocity. However, the wave speed at Kvilldal should be more predictable and less sensitive to variations from air entrainment due to the high pressure.

Further Work

Further investigation on application of seismic interferometry as a post-processing technique to find the propagation velocity is necessary in order to develop the method. Experiments could be done on any pipe section with a known excitation force. The frequency and strength of the excitation force, the length between pressure transducers and sampling rate should be taken into consideration in the planning of the experiments. At least three flush mounted pressure transducers should be installed in the axial direction with a known distance.

The measurements from Kvilldal should be investigated further. The limited time of the work related to this thesis has made it difficult to get a full overview of the events happening in the data. The figures presented can be used to find interesting operation points to investigate further. It could also be an idea to apply statistical models to investigate the randomness of events at specific loads.

The measurements from Kvilldal can also be used in validation of simulations by trying to develop simulation models that replicate events.

The numerical model of Kvilldal can be improved. One main concern is the reflection points related to the series junctions. These are simply two pipes with different diameters in the model, while the connection at Kvilldal is a smooth transition over several meters. The difference between the two cases would be interesting to pursue.

Bibliography

- [1] ANTONSEN, Ø. *Unsteady flow in wicket gate and runner with focus on static and dynamic load on runner*. PhD thesis, NTNU, Fakultet for ingeniørvitenskap og teknologi, 2007.
- [2] BERGH, H., AND TIJDEMAN, H. Theoretical and experimental results for the dynamic response of pressure measuring systems. Nationaal lucht-en ruimtevaartlaboratorium, 1965.
- [3] BREKKE, H. Pumper & turbiner. *Vannkraftlaboratoriet NTNU* (2003).
- [4] CHAUDHRY, M. H. Transient-flow equations. In *Applied hydraulic transients*. Springer, 2014.
- [5] CLAERBOUT, J. F. Synthesis of a layered medium from its acoustic transmission response. *Geophysics* 33, 2 (1968), 264–269.
- [6] CLAUDE, B. *Fatigue limit in metals*. ISTE Ltd : John Wiley & Sons, 2014.
- [7] CLAUDE, B., AND PINEAU, A. *Fatigue of materials and structures-fundamentals*, 2010.
- [8] CURTIS, A., GERSTOFT, P., SATO, H., SNIEDER, R., AND WAPENAAR, K. Seismic interferometry—turning noise into signal. *The Leading Edge* 25, 9 (2006), 1082–1092.
- [9] DÖRFLER, P., SICK, M., AND COUTU, A. *Flow-induced pulsation and vibration in hydroelectric machinery: engineer’s guidebook for planning, design and troubleshooting*. Springer, 2012.
- [10] DÖRFLER, P. K. Evaluating 1d models for vortex-induced pulsation in francis turbines. In *3rd IAHR International Meeting of the Workgroup on Cavitation and Dynamic Problems in Hydraulic Machinery and Systems, Brno, Czech Republic, Oct (2009)*, pp. 14–16.
- [11] E.BENJAMIN WYLIE, V. L. S. *Fluid Transients corrected edition*, fourth ed. Thomson-Shore, Dexter,MI, 1988.
- [12] FREND, R. Piping vibration part 1. natural frequency of a pipe, 2016. [<https://www.petroskills.com/blog/entry/piping-vibration-calculate-natural-frequency#.XOetz8gzaUk>].
- [13] FU, T., DENG, Z. D., DUNCAN, J. P., ZHOU, D., CARLSON, T. J., JOHNSON, G. E., AND HOU, H. Assessing hydraulic conditions through francis turbines using an autonomous sensor device. *Renewable Energy* 99 (2016), 1244–1252.

-
- [14] GE-MEASUREMENT. Unik 5000 datasheet, 2018. [https://www.gemeasurement.com/sites/gemc.dev/files/unik_5000_datasheet_english.pdf].
- [15] GHIDAOU, M. S., ZHAO, M., MCINNIS, D. A., AND AXWORTHY, D. H. A review of water hammer theory and practice. *Applied Mechanics Reviews* 58, 1 (2005), 49–76.
- [16] GIDSKEHAUG, S. L. Trykkpulsasjoner i francisturbin. Master's thesis, NTNU, 2010.
- [17] GONGWER, C. A study of vanes singing in water. *JOURNAL OF APPLIED MECHANICS-TRANSACTIONS OF THE ASME* 19, 4 (1952), 432–438.
- [18] HAAVIK, K. E. *Source-Depth Diversity for Enhanced Marine Seismic Imaging*. PhD thesis, NTNU, 2016.
- [19] HARANO, M., TANI, K., AND NOMOTO, S. Practical application of high-performance francis-turbine runner fitted with splitter blades at ontake and shinkurobegawa no. 3 power stations of the kansai electric power co., inc. *Hitachi Review* 55, 3 (2006), 109.
- [20] HESKESTAD, G., AND OLBERTS, D. Influence of trailing-edge geometry on hydraulic-turbine-blade vibration resulting from vortex excitation. *Journal of Engineering for Power* 82, 2 (1960), 103–109.
- [21] HOU, Y., LI, R., AND ZHANG, J. Research on the length ratio of splitter blades for ultra-high head francis runners. *Procedia Engineering* 31 (2012), 92–96.
- [22] HUANG, X., ORAM, C., AND SICK, M. Static and dynamic stress analyses of the prototype high head francis runner based on site measurement. *IOP Conference Series: Earth and Environmental Science* 22 (2014), 032052.
- [23] JAEGER, C. The theory of resonance in hydropower systems. discussion of incidents and accidents occurring in pressure systems. *Journal of Basic Engineering* 85, 4 (1963), 631–640.
- [24] JERNSLETTEN, J. *Analysis of Non-Stationary Flow in a Francis Reversible Pump Turbine Runner*. PhD thesis, Norwegian Institute of Technology, 1995.
- [25] KOBRO, E. *Measurement of pressure pulsations in Francis turbines*. PhD thesis, NTNU, 2010.
- [26] KULITE. Kulite khm 375 miniature high pressure pressure transducer datasheet, 2018. [<https://www.kulite.com/assets/media/2018/01/HKM-375.pdf>].
- [27] LEE, Y.-L., BARKEY, M. E., AND KANG, H.-T. *Metal fatigue analysis handbook: practical problem-solving techniques for computer-aided engineering*. Elsevier, 2011.
- [28] LIU, X., LUO, Y., AND WANG, Z. A review on fatigue damage mechanism in hydro turbines. *Renewable and Sustainable Energy Reviews* 54 (2016), 1–14.
- [29] MELESHKO, V. V., AND AREF, H. A bibliography of vortex dynamics 1858-1956. *Advances in Applied Mechanics* 41, 197 (2007), 197–292.
- [30] MODERN POWER SYSTEMS, U. T. P. L. Ulla førre high head hydro power scheme. picture is taken from a illustration of Ulla Førre, at the hydropower laboratory at NTNU.

-
- [31] NEK IEC 60193 Hydraulic turbines, storage pumps and pump-turbines - Model acceptance tests, 2019.
- [32] NENNEMANN, B., VU, T., AND FARHAT, M. CFD prediction of unsteady wicket gate-runner interaction in francis turbines: A new standard hydraulic design procedure, 2005.
- [33] NICOLET, C., ZOBEIRI, A., MARUZEWSKI, P., AND AVELLAN, F. On the upper part load vortex rope in francis turbine: Experimental investigation. *IOP Conference Series: Earth and Environmental Science* 12 (2010), 012053.
- [34] NIELSEN, T. Dynamic dimensioning of hydro power plants. *Vannkraftlaboratiet, NTNU* (2015).
- [35] NORTON, M. P., AND KARZUB, D. G. *Fundamentals of noise and vibration analysis for engineers*. Cambridge university press, 2003.
- [36] OLESEN, H. Detection of pressure variations in thin walled tubes by vibration measurements. In *Pipe vibration and pressure detection*. Bruel & Kjaer, 1972, pp. 3–9.
- [37] RAYLE, R. E. An investigation of the influence of orifice geometry on static pressure measurements. Master’s thesis, Massachusetts Institute of Technology, 1949.
- [38] RHEINGANS, W. Power swings in hydroelectric power plants. *Trans. ASME* 62, 3 (1940), 171–184.
- [39] RUCHONNET, N., NICOLET, C., AND AVELLAN, F. Hydroacoustic modeling of rotor stator interaction in francis pump-turbine. In *Proceedings of IAHR Int. Meeting of Working Group on Cavitation and Dynamic Problems in Hydraulic Machinery and Systems, Barcelona, 28-30 June* (2006).
- [40] RUDOLF, P., HABÁN, V., POCHYLÝ, F., KOUTNÍK, J., AND KRÜGER, K. Collapse of cylindrical cavitating region and conditions for existence of elliptical form of cavitating vortex rope. In *Proc. IAHR Int. Meeting of WG on Cavitation and Dynamic Problems in Hydraulic Machinery and Systems, Timisoara* (2007).
- [41] SEIDEL, U., HÜBNER, B., LÖFFLAD, J., AND FAIGLE, P. Evaluation of RSI-induced stresses in francis runners. *IOP Conference Series: Earth and Environmental Science* 15 (2012), 052010.
- [42] STATKRAFT. Brochure of ulla førre powerplants from statkraft, 2018. [<https://www.statkraft.no/globalassets/1-statkraft-public/04-energy-sources/power-plants/brochures/10152-ulla-forre-kraftstasjonsbrosjyre-8s-no-single.pdf>].
- [43] SUO, L., AND WYLIE, E. B. Hydraulic transients in rock-bored tunnels. *Journal of Hydraulic Engineering* 116, 2 (1990), 196–210.
- [44] THEODORO, F. R. F., REIS, M. L. C. D. C., AND D’SOUTO, C. An overview of the dynamic calibration of piezoelectric pressure transducers. *Journal of Physics: Conference Series* 975, 1 (2018), 012002.
- [45] TRIVEDI, C., AND CERVANTES, M. J. Fluid-structure interactions in francis turbines: A perspective review. *Renewable and Sustainable Energy Reviews* 68 (2017), 87–101.
-

-
- [46] TWYMAN, J. Wave speed calculation for water hammer analysis. *Obras y Proyectos 1*, 20 (2018), 86–92.
- [47] VASCONCELOS, I., AND SNIEDER, R. Interferometry by deconvolution, part I: Theory and numerical examples, 2007.
- [48] VU, T. C., NENNEMANN, B., AUSONI, P., FARHAT, M., AND AVELLAN, F. Unsteady cfd prediction of von kármán vortex shedding in hydraulic turbine stay vanes. *Proceedings of Hydro2007, Granada* (2007).
- [49] WAPENAAR, K., DRAGANOV, D., SNIEDER, R., CAMPMAN, X., AND VERDEL, A. Tutorial on seismic interferometry: Part I: Basic principles and applications. *Geophysics* 75, 5 (2010), 75A195–75A209.
- [50] WU, Y., LI, S., LIU, S., DOU, H.-S., AND QIAN, Z. Vibration induced by hydraulic excitation. In *Vibration of hydraulic machinery*. Springer, 2013, ch. 6, pp. 147–228.
- [51] YUNUS, A. C., AND CIMBALA, J. M. Fluid mechanics fundamentals and applications. *International Edition, McGraw Hill Publication 185201* (2006).
- [52] ZHANG, M., LIU, Y., WANG, W., WANG, P., AND LI, J. The fatigue of impellers and blades. *Engineering Failure Analysis* 62 (2016), 208–231.
- [53] ZOBELI, A., KUENY, J.-L., FARHAT, M., AND AVELLAN, F. Pump-turbine rotor-stator interactions in generating mode: pressure fluctuation in distributor channel. *23rd IAHR symposium on hydraulic machinery and systems* (2006).

Appendix A

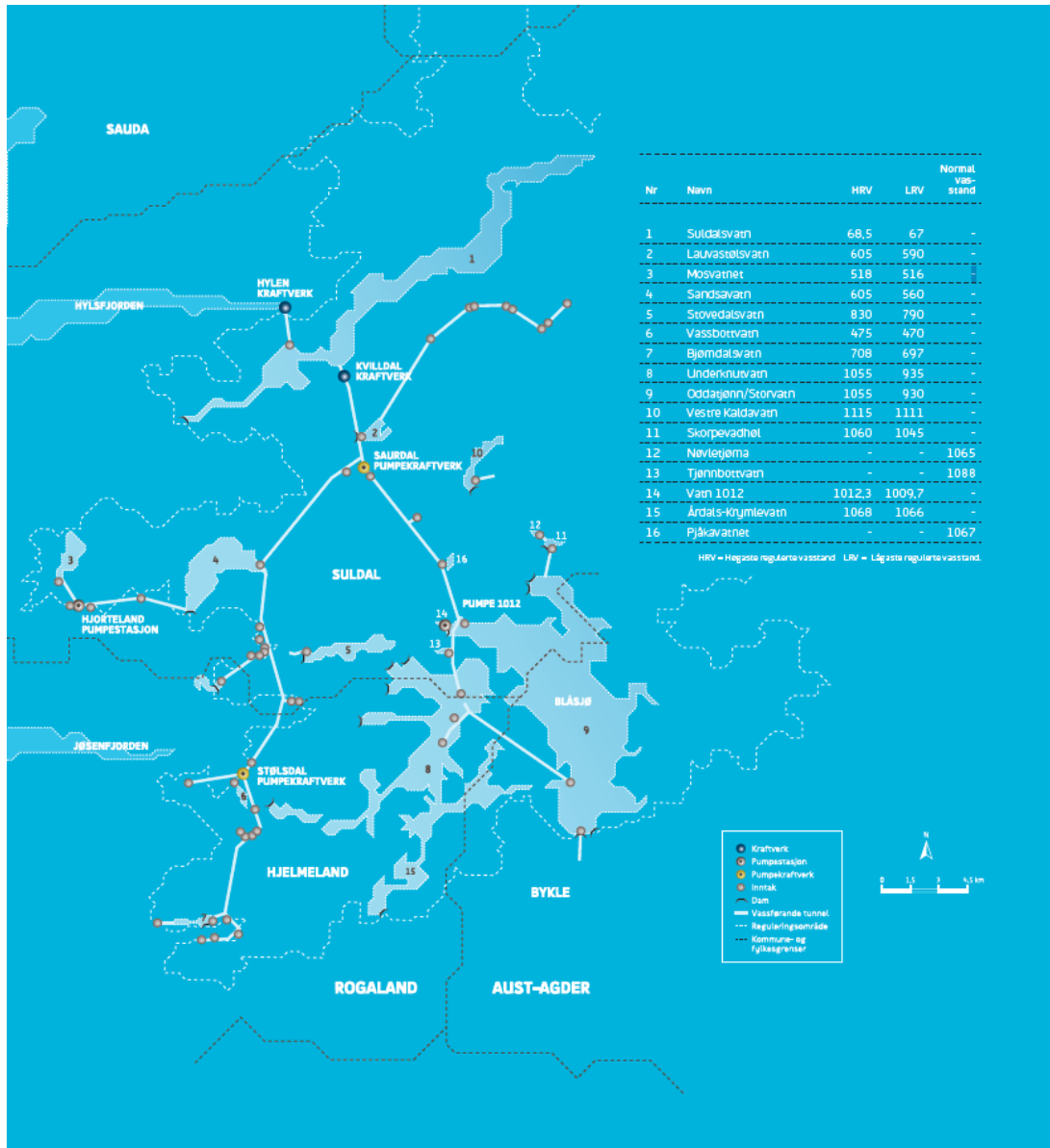


Figure 10.1: Ulla Førre Power plant system

Appendix B

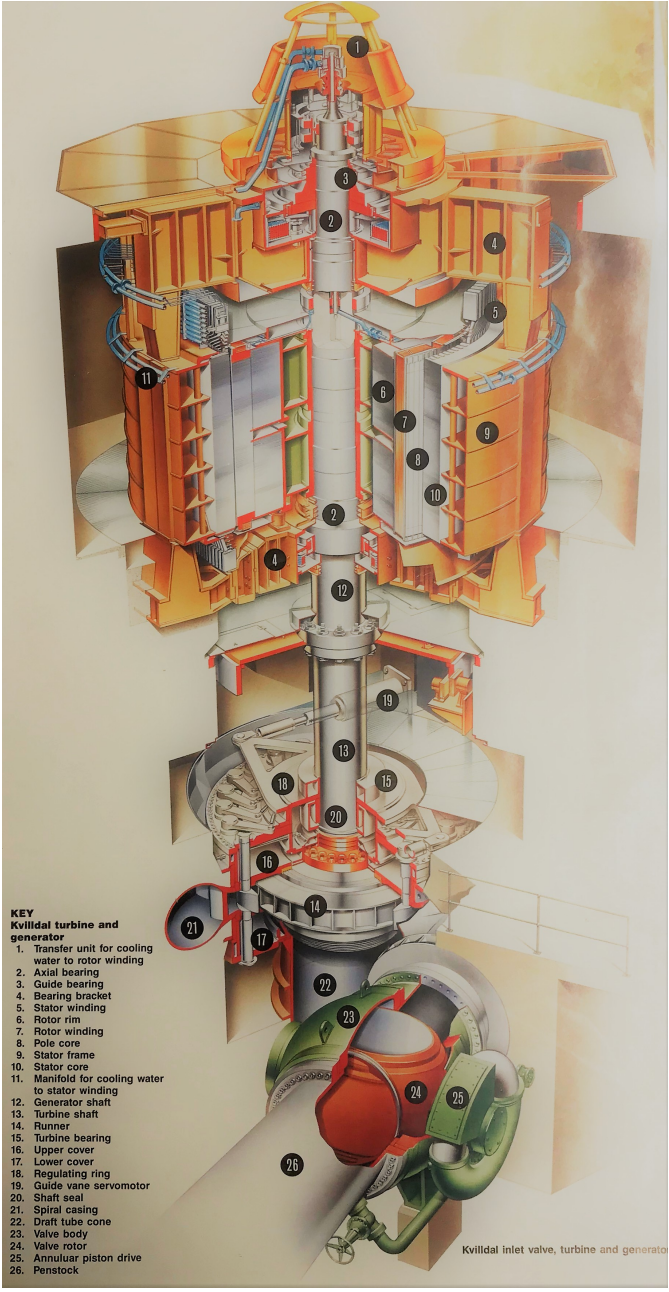


Figure 10.2: Kvilldal turbine [30]

Appendix C

CALIBRATION REPORT

CALIBRATION PROPERTIES

Calibrated by: Magnus Perkunder
 Type/Producer: Druck UNIK 5000
 SN: 5506047
 Range: 0-70 bar a
 Unit: kPa
 test
 Druck PTX 1830
 2867610
 0-10 bar a
 kPa

CALIBRATION SOURCE PROPERTIES

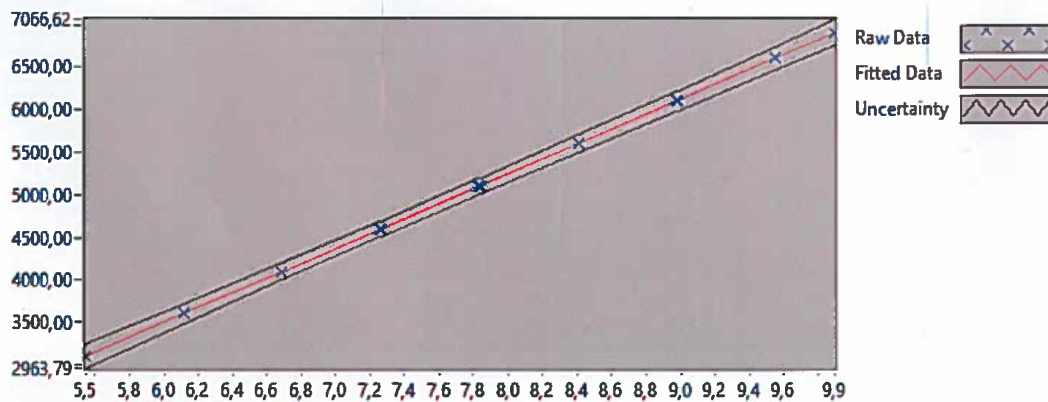
Type/Producer: Pressurements deadweight tester P3223-1
 SN: 66256
 Uncertainty [%]: 0,01

POLY FIT EQUATION:

$Y = -1,74248583E+3X^0 + 874,17282607E+0X^1$

CALIBRATION SUMMARY:

Max Uncertainty : 0,044868 [%]
 Max Uncertainty : 1,547188 [kPa]
 RSQ : 0,999997
 Calibration points : 36



Magnus Perkunder
 Magnus Perkunder

CALIBRATION VALUES

<u>Value [kPa]</u>	<u>Voltage [V]</u>	<u>Best Poly Fit [kPa]</u>	<u>Deviation [kPa]</u>	<u>Uncertainty [%]</u>	<u>Uncertainty [kPa]</u>
<u>3103,727120</u>	<u>5,546115</u>	<u>3105,777221</u>	<u>-2,050100</u>	<u>0,044735</u>	<u>1,388452</u>
<u>3604,482475</u>	<u>6,116606</u>	<u>3604,485178</u>	<u>-0,002702</u>	<u>0,032590</u>	<u>1,174702</u>
<u>4105,237830</u>	<u>6,689019</u>	<u>4104,872457</u>	<u>0,365373</u>	<u>0,024593</u>	<u>1,009606</u>
<u>4605,993185</u>	<u>7,254722</u>	<u>4599,394841</u>	<u>6,598344</u>	<u>0,019929</u>	<u>0,917907</u>
<u>5106,748539</u>	<u>7,824501</u>	<u>5097,480647</u>	<u>9,267892</u>	<u>0,018095</u>	<u>0,924074</u>
<u>5607,503894</u>	<u>8,406323</u>	<u>5606,093419</u>	<u>1,410475</u>	<u>0,018216</u>	<u>1,021436</u>
<u>6108,259249</u>	<u>8,980919</u>	<u>6108,389841</u>	<u>-0,130592</u>	<u>0,019438</u>	<u>1,187295</u>
<u>6609,014604</u>	<u>9,553384</u>	<u>6608,822953</u>	<u>0,191651</u>	<u>0,021186</u>	<u>1,400168</u>
<u>6909,467817</u>	<u>9,900258</u>	<u>6912,050522</u>	<u>-2,582706</u>	<u>0,022371</u>	<u>1,545719</u>
<u>6909,467817</u>	<u>9,896950</u>	<u>6909,158904</u>	<u>0,308912</u>	<u>0,022392</u>	<u>1,547188</u>
<u>6609,014604</u>	<u>9,554365</u>	<u>6609,680552</u>	<u>-0,665949</u>	<u>0,021198</u>	<u>1,401010</u>
<u>6108,259249</u>	<u>8,981680</u>	<u>6109,054745</u>	<u>-0,795496</u>	<u>0,019403</u>	<u>1,185159</u>
<u>5607,503894</u>	<u>8,406649</u>	<u>5606,378405</u>	<u>1,125489</u>	<u>0,018159</u>	<u>1,018283</u>
<u>5106,748539</u>	<u>7,835412</u>	<u>5107,018671</u>	<u>-0,270131</u>	<u>0,017973</u>	<u>0,917857</u>
<u>4605,993185</u>	<u>7,258876</u>	<u>4603,026408</u>	<u>2,966777</u>	<u>0,019823</u>	<u>0,913049</u>
<u>4105,237830</u>	<u>6,690718</u>	<u>4106,358319</u>	<u>-1,120489</u>	<u>0,024529</u>	<u>1,006956</u>
<u>3604,482475</u>	<u>6,117574</u>	<u>3605,331558</u>	<u>-0,849083</u>	<u>0,032551</u>	<u>1,173284</u>
<u>3103,727120</u>	<u>5,546875</u>	<u>3106,441391</u>	<u>-2,714270</u>	<u>0,044868</u>	<u>1,392588</u>
<u>3103,727120</u>	<u>5,545578</u>	<u>3105,307356</u>	<u>-1,580236</u>	<u>0,044674</u>	<u>1,386572</u>
<u>3604,482475</u>	<u>6,118017</u>	<u>3605,718659</u>	<u>-1,236184</u>	<u>0,032536</u>	<u>1,172759</u>
<u>4105,237830</u>	<u>6,690637</u>	<u>4106,286852</u>	<u>-1,049022</u>	<u>0,024527</u>	<u>1,006885</u>
<u>4605,993185</u>	<u>7,262251</u>	<u>4605,976316</u>	<u>0,016869</u>	<u>0,019821</u>	<u>0,912957</u>
<u>5106,748539</u>	<u>7,836941</u>	<u>5108,355023</u>	<u>-1,606484</u>	<u>0,017952</u>	<u>0,916751</u>
<u>5607,503894</u>	<u>8,409396</u>	<u>5608,779261</u>	<u>-1,275367</u>	<u>0,018086</u>	<u>1,014159</u>
<u>6108,259249</u>	<u>8,981033</u>	<u>6108,489004</u>	<u>-0,229755</u>	<u>0,019462</u>	<u>1,188798</u>
<u>6609,014604</u>	<u>9,553572</u>	<u>6608,987586</u>	<u>0,027018</u>	<u>0,021233</u>	<u>1,403324</u>
<u>6909,467817</u>	<u>9,898291</u>	<u>6910,331019</u>	<u>-0,863203</u>	<u>0,022358</u>	<u>1,544800</u>
<u>6609,014604</u>	<u>9,554397</u>	<u>6609,708579</u>	<u>-0,693975</u>	<u>0,021189</u>	<u>1,400378</u>
<u>6108,259249</u>	<u>8,982843</u>	<u>6110,071642</u>	<u>-1,812393</u>	<u>0,019395</u>	<u>1,184705</u>
<u>5607,503894</u>	<u>8,409915</u>	<u>5609,233520</u>	<u>-1,729626</u>	<u>0,018152</u>	<u>1,017875</u>
<u>5106,748539</u>	<u>7,835495</u>	<u>5107,090898</u>	<u>-0,342359</u>	<u>0,017968</u>	<u>0,917578</u>
<u>4605,993185</u>	<u>7,261756</u>	<u>4605,543786</u>	<u>0,449399</u>	<u>0,019853</u>	<u>0,914406</u>
<u>4105,237830</u>	<u>6,689389</u>	<u>4105,195982</u>	<u>0,041848</u>	<u>0,024536</u>	<u>1,007271</u>
<u>3604,482475</u>	<u>6,116981</u>	<u>3604,813052</u>	<u>-0,330577</u>	<u>0,032559</u>	<u>1,173581</u>
<u>3103,727120</u>	<u>5,543502</u>	<u>3103,493131</u>	<u>0,233989</u>	<u>0,044708</u>	<u>1,387625</u>
<u>3103,727120</u>	<u>5,542710</u>	<u>3102,800457</u>	<u>0,926663</u>	<u>0,044789</u>	<u>1,390137</u>

COMMENTS:

The uncertainty is calculated with 95% confidence. The uncertainty includes the randomness in the calibrated instrument during the calibration, systematic uncertainty in the instrument or property which the instrument under calibration is compared with (dead weight manometer, calibrated weights etc.), and due to regression analysis to fit the calibration points to a linear calibration equation. The calculated uncertainty can be used as the total systematic uncertainty of the calibrated instrument with the given calibration equation.

CALIBRATION REPORT

CALIBRATION PROPERTIES

Calibrated by: Magnus Perkunder
Type/Producer: Druck UNIK 5000
SN: 5506048
Range: 0-70 bar a
Unit: kPa
test
Druck PTX 1830
2867610
0-10 bar a
kPa

CALIBRATION SOURCE PROPERTIES

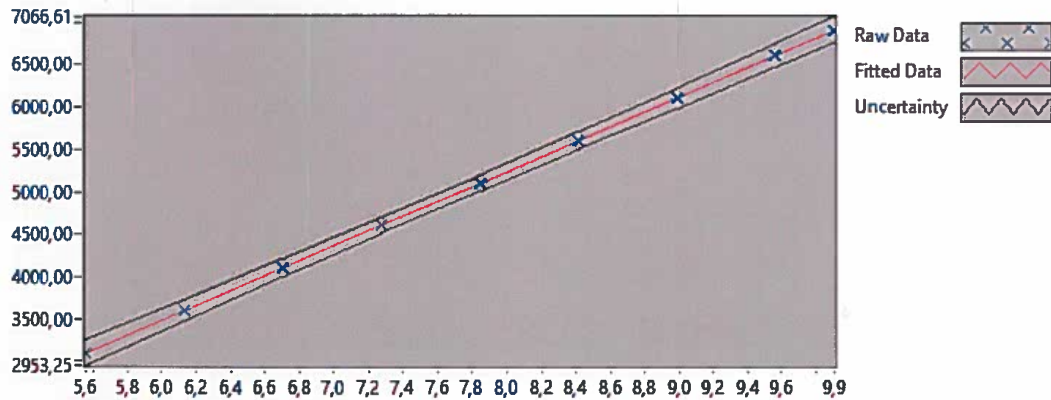
Type/Producer: Pressurements deadweight tester P3223-1
SN: 66256
Uncertainty [%]: 0,01


POLY FIT EQUATION:

$Y = -1,75682085E+3X^0 + 875,10201033E+0X^1$

CALIBRATION SUMMARY:

Max Uncertainty : 0,048096 [%]
Max Uncertainty : 1,554784 [kPa]
RSQ : 0,999997
Calibration points : 36




Magnus Perkunder

CALIBRATION VALUES

<u>Value [kPa]</u>	<u>Voltage [V]</u>	<u>Best Poly Fit [kPa]</u>	<u>Deviation [kPa]</u>	<u>Uncertainty [%]</u>	<u>Uncertainty [kPa]</u>
<u>3103,729123</u>	<u>5,554509</u>	<u>3103,940874</u>	<u>-0,211751</u>	<u>0,048029</u>	<u>1,490699</u>
<u>3604,484477</u>	<u>6,125981</u>	<u>3604,037681</u>	<u>0,446796</u>	<u>0,034953</u>	<u>1,259864</u>
<u>4105,239832</u>	<u>6,695752</u>	<u>4102,645486</u>	<u>2,594346</u>	<u>0,026252</u>	<u>1,077707</u>
<u>4605,995187</u>	<u>7,269279</u>	<u>4604,539625</u>	<u>1,455562</u>	<u>0,020920</u>	<u>0,963585</u>
<u>5106,750542</u>	<u>7,840356</u>	<u>5104,290417</u>	<u>2,460125</u>	<u>0,018674</u>	<u>0,953615</u>
<u>5607,505896</u>	<u>8,411584</u>	<u>5604,173601</u>	<u>3,332295</u>	<u>0,018383</u>	<u>1,030807</u>
<u>6108,261251</u>	<u>8,985955</u>	<u>6106,806527</u>	<u>1,454724</u>	<u>0,019461</u>	<u>1,188729</u>
<u>6609,016606</u>	<u>9,553277</u>	<u>6603,270890</u>	<u>5,745716</u>	<u>0,021286</u>	<u>1,406791</u>
<u>6909,469819</u>	<u>9,900080</u>	<u>6906,758980</u>	<u>2,710838</u>	<u>0,022353</u>	<u>1,544493</u>
<u>6909,469819</u>	<u>9,900481</u>	<u>6907,109810</u>	<u>2,360009</u>	<u>0,022502</u>	<u>1,554784</u>
<u>6609,016606</u>	<u>9,559142</u>	<u>6608,403790</u>	<u>0,612816</u>	<u>0,021179</u>	<u>1,399726</u>
<u>6108,261251</u>	<u>8,987690</u>	<u>6108,324575</u>	<u>-0,063323</u>	<u>0,019311</u>	<u>1,179559</u>
<u>5607,505896</u>	<u>8,419740</u>	<u>5611,310472</u>	<u>-3,804576</u>	<u>0,018289</u>	<u>1,025581</u>
<u>5106,750542</u>	<u>7,837956</u>	<u>5102,190153</u>	<u>4,560388</u>	<u>0,018497</u>	<u>0,944579</u>
<u>4605,995187</u>	<u>7,269640</u>	<u>4604,856014</u>	<u>1,139173</u>	<u>0,020901</u>	<u>0,962679</u>
<u>4105,239832</u>	<u>6,703174</u>	<u>4109,140220</u>	<u>-3,900388</u>	<u>0,026264</u>	<u>1,078218</u>
<u>3604,484477</u>	<u>6,127749</u>	<u>3605,584389</u>	<u>-1,099911</u>	<u>0,034941</u>	<u>1,259448</u>
<u>3103,729123</u>	<u>5,554472</u>	<u>3103,909126</u>	<u>-0,180004</u>	<u>0,048020</u>	<u>1,490415</u>
<u>3103,729123</u>	<u>5,554500</u>	<u>3103,932828</u>	<u>-0,203705</u>	<u>0,047989</u>	<u>1,489446</u>
<u>3604,484477</u>	<u>6,127666</u>	<u>3605,512221</u>	<u>-1,027744</u>	<u>0,035010</u>	<u>1,261935</u>
<u>4105,239832</u>	<u>6,698065</u>	<u>4104,669623</u>	<u>0,570209</u>	<u>0,026148</u>	<u>1,073456</u>
<u>4605,995187</u>	<u>7,269722</u>	<u>4604,927641</u>	<u>1,067546</u>	<u>0,020809</u>	<u>0,958484</u>
<u>5106,750542</u>	<u>7,843330</u>	<u>5106,893391</u>	<u>-0,142849</u>	<u>0,018358</u>	<u>0,937490</u>
<u>5607,505896</u>	<u>8,414078</u>	<u>5606,355462</u>	<u>1,150435</u>	<u>0,018161</u>	<u>1,018364</u>
<u>6108,261251</u>	<u>8,989645</u>	<u>6110,035314</u>	<u>-1,774063</u>	<u>0,019314</u>	<u>1,179768</u>
<u>6609,016606</u>	<u>9,563054</u>	<u>6611,827183</u>	<u>-2,810577</u>	<u>0,021136</u>	<u>1,396866</u>
<u>6909,469819</u>	<u>9,906390</u>	<u>6912,280620</u>	<u>-2,810802</u>	<u>0,022336</u>	<u>1,543305</u>
<u>6909,469819</u>	<u>9,905547</u>	<u>6911,543023</u>	<u>-2,073205</u>	<u>0,022348</u>	<u>1,544119</u>
<u>6609,016606</u>	<u>9,563854</u>	<u>6612,527135</u>	<u>-3,510529</u>	<u>0,021141</u>	<u>1,397222</u>
<u>6108,261251</u>	<u>8,989459</u>	<u>6109,873078</u>	<u>-1,611827</u>	<u>0,019328</u>	<u>1,180601</u>
<u>5607,505896</u>	<u>8,417264</u>	<u>5609,144142</u>	<u>-1,638245</u>	<u>0,018199</u>	<u>1,020490</u>
<u>5106,750542</u>	<u>7,845143</u>	<u>5108,479430</u>	<u>-1,728888</u>	<u>0,018337</u>	<u>0,936413</u>
<u>4605,995187</u>	<u>7,275695</u>	<u>4610,154299</u>	<u>-4,159112</u>	<u>0,020863</u>	<u>0,960966</u>
<u>4105,239832</u>	<u>6,699141</u>	<u>4105,611015</u>	<u>-0,371183</u>	<u>0,026312</u>	<u>1,080173</u>
<u>3604,484477</u>	<u>6,126190</u>	<u>3604,220579</u>	<u>0,263899</u>	<u>0,035013</u>	<u>1,262052</u>
<u>3103,729123</u>	<u>5,552898</u>	<u>3102,531316</u>	<u>1,197807</u>	<u>0,048096</u>	<u>1,492783</u>

COMMENTS:

The uncertainty is calculated with 95% confidence. The uncertainty includes the randomness in the calibrated instrument during the calibration, systematic uncertainty in the instrument or property which the instrument under calibration is compared with (dead weight manometer, calibrated weights etc.), and due to regression analysis to fit the calibration points to a linear calibration equation. The calculated uncertainty can be used as the total systematic uncertainty of the calibrated instrument with the given calibration equation.

CALIBRATION REPORT

CALIBRATION PROPERTIES

Calibrated by: Magnus Perkunder
 Type/Producer: Druck UNIK 5000
 SN: 5506049
 Range: 0-70 bar a
 Unit: kPa
 test
 Druck PTX 1830
 2867610
 0-10 bar a
 kPa

CALIBRATION SOURCE PROPERTIES

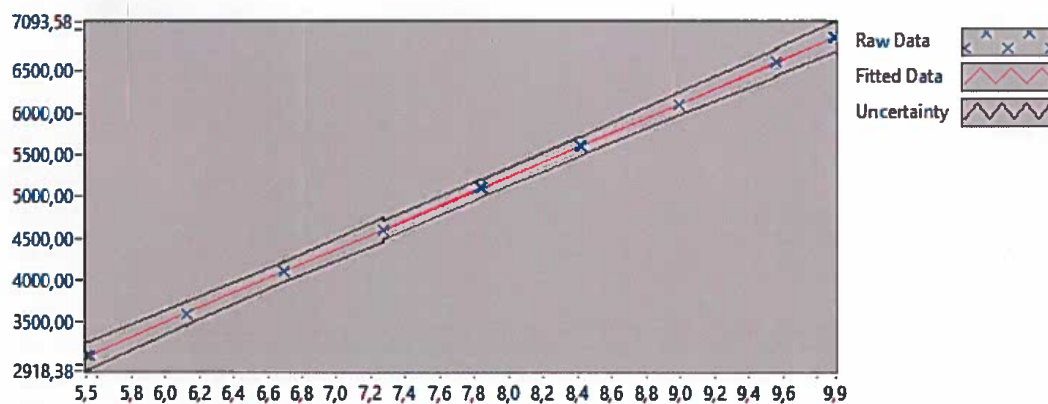
Type/Producer: Pressurements deadweight tester P3223-1
 SN: 66256
 Uncertainty [%]: 0,01

POLY FIT EQUATION:

$Y = -1,75108386E+3X^0 + 874,68193622E+0X^1$

CALIBRATION SUMMARY:

Max Uncertainty : 0,056026 [%]
 Max Uncertainty : 1,821237 [kPa]
 RSQ : 0,999995
 Calibration points : 36



Magnus Perkunder
 Magnus Perkunder

CALIBRATION VALUES

Value [kPa]	Voltage [V]	Best Poly Fit [kPa]	Deviation [kPa]	Uncertainty [%]	Uncertainty [kPa]
<u>3103,729123</u>	<u>5,553557</u>	<u>3106,512526</u>	<u>-2,783404</u>	<u>0,053981</u>	<u>1,675422</u>
<u>3604,484477</u>	<u>6,126964</u>	<u>3608,060498</u>	<u>-3,576021</u>	<u>0,038999</u>	<u>1,405729</u>
<u>4105,239832</u>	<u>6,694078</u>	<u>4104,105367</u>	<u>1,134465</u>	<u>0,030839</u>	<u>1,266020</u>
<u>4605,995187</u>	<u>7,268001</u>	<u>4606,105194</u>	<u>-0,110008</u>	<u>0,030551</u>	<u>1,407173</u>
<u>5106,750542</u>	<u>7,840137</u>	<u>5106,541956</u>	<u>0,208585</u>	<u>0,021147</u>	<u>1,079935</u>
<u>5607,505896</u>	<u>8,413534</u>	<u>5608,082172</u>	<u>-0,576275</u>	<u>0,021206</u>	<u>1,189148</u>
<u>6108,261251</u>	<u>8,983419</u>	<u>6106,550378</u>	<u>1,710873</u>	<u>0,022603</u>	<u>1,380680</u>
<u>6609,016606</u>	<u>9,555608</u>	<u>6607,033620</u>	<u>1,982986</u>	<u>0,024905</u>	<u>1,645969</u>
<u>6909,469819</u>	<u>9,898419</u>	<u>6906,884696</u>	<u>2,585123</u>	<u>0,026359</u>	<u>1,821237</u>
<u>6609,016606</u>	<u>9,554972</u>	<u>6606,477680</u>	<u>2,538926</u>	<u>0,025091</u>	<u>1,658293</u>
<u>6108,261251</u>	<u>8,985828</u>	<u>6108,657221</u>	<u>-0,395970</u>	<u>0,022589</u>	<u>1,379821</u>
<u>5607,505896</u>	<u>8,412394</u>	<u>5607,085267</u>	<u>0,420630</u>	<u>0,020910</u>	<u>1,172556</u>
<u>5106,750542</u>	<u>7,839435</u>	<u>5105,928291</u>	<u>0,822250</u>	<u>0,020796</u>	<u>1,062008</u>
<u>4605,995187</u>	<u>7,269628</u>	<u>4607,528180</u>	<u>-1,532993</u>	<u>0,025952</u>	<u>1,195334</u>
<u>4105,239832</u>	<u>6,695858</u>	<u>4105,662240</u>	<u>-0,422408</u>	<u>0,029112</u>	<u>1,195133</u>
<u>3604,484477</u>	<u>6,123608</u>	<u>3605,125535</u>	<u>-0,641058</u>	<u>0,039050</u>	<u>1,407563</u>
<u>3103,729123</u>	<u>5,550931</u>	<u>3104,215509</u>	<u>-0,486387</u>	<u>0,054062</u>	<u>1,677951</u>
<u>3103,729123</u>	<u>5,537275</u>	<u>3092,270965</u>	<u>11,458158</u>	<u>0,056026</u>	<u>1,738908</u>
<u>3103,729123</u>	<u>5,550806</u>	<u>3104,106189</u>	<u>-0,377067</u>	<u>0,054068</u>	<u>1,678118</u>
<u>3604,484477</u>	<u>6,125268</u>	<u>3606,577214</u>	<u>-2,092737</u>	<u>0,041624</u>	<u>1,500349</u>
<u>4105,239832</u>	<u>6,697187</u>	<u>4106,824394</u>	<u>-1,584562</u>	<u>0,029039</u>	<u>1,192121</u>
<u>4605,995187</u>	<u>7,269972</u>	<u>4607,829521</u>	<u>-1,834334</u>	<u>0,023111</u>	<u>1,064482</u>
<u>5106,750542</u>	<u>7,842562</u>	<u>5108,663150</u>	<u>-1,912608</u>	<u>0,020710</u>	<u>1,057586</u>
<u>5607,505896</u>	<u>8,415035</u>	<u>5609,395642</u>	<u>-1,889745</u>	<u>0,020905</u>	<u>1,172242</u>
<u>6108,261251</u>	<u>8,987810</u>	<u>6110,390894</u>	<u>-2,129643</u>	<u>0,022592</u>	<u>1,379955</u>
<u>6609,016606</u>	<u>9,559428</u>	<u>6610,375423</u>	<u>-1,358817</u>	<u>0,024896</u>	<u>1,645359</u>
<u>6909,469819</u>	<u>9,903684</u>	<u>6911,489205</u>	<u>-2,019386</u>	<u>0,026354</u>	<u>1,820890</u>
<u>6909,469819</u>	<u>9,902154</u>	<u>6910,151274</u>	<u>-0,681455</u>	<u>0,026337</u>	<u>1,819764</u>
<u>6609,016606</u>	<u>9,560129</u>	<u>6610,987855</u>	<u>-1,971250</u>	<u>0,024867</u>	<u>1,643467</u>
<u>6108,261251</u>	<u>8,985428</u>	<u>6108,307691</u>	<u>-0,046440</u>	<u>0,022562</u>	<u>1,378141</u>
<u>5607,505896</u>	<u>8,410792</u>	<u>5605,683973</u>	<u>1,821924</u>	<u>0,020985</u>	<u>1,176748</u>
<u>5106,750542</u>	<u>7,835684</u>	<u>5102,647519</u>	<u>4,103023</u>	<u>0,020730</u>	<u>1,058616</u>
<u>4605,995187</u>	<u>7,269252</u>	<u>4607,199325</u>	<u>-1,204138</u>	<u>0,023254</u>	<u>1,071089</u>
<u>4105,239832</u>	<u>6,689357</u>	<u>4099,975631</u>	<u>5,264201</u>	<u>0,029487</u>	<u>1,210513</u>
<u>3604,484477</u>	<u>6,125111</u>	<u>3606,439793</u>	<u>-1,955316</u>	<u>0,039212</u>	<u>1,413406</u>
<u>3103,729123</u>	<u>5,553198</u>	<u>3106,198245</u>	<u>-2,469122</u>	<u>0,054011</u>	<u>1,676352</u>

COMMENTS:

The uncertainty is calculated with 95% confidence. The uncertainty includes the randomness in the calibrated instrument during the calibration, systematic uncertainty in the instrument or property which the instrument under calibration is compared with (dead weight manometer, calibrated weights etc.), and due to regression analysis to fit the calibration points to a linear calibration equation. The calculated uncertainty can be used as the total systematic uncertainty of the calibrated instrument with the given calibration equation.

CALIBRATION REPORT

CALIBRATION PROPERTIES

Calibrated by: Magnus Perkunder
 Type/Producer: Druck UNIK 5000
 SN: 5506050
 Range: 0-70 bar a
 Unit: kPa
 test
 Druck PTX 1830
 2867610
 0-10 bar a
 kPa

CALIBRATION SOURCE PROPERTIES

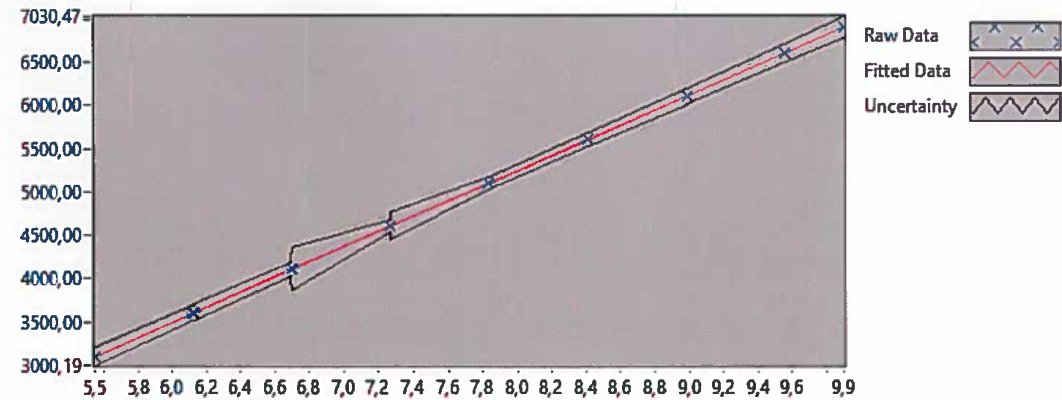
Type/Producer: Pressurements deadweight tester P3223-1
 SN: 66256
 Uncertainty [%]: 0,01

POLY FIT EQUATION:

$Y = -1,74876411E+3X^0 + 874,68757229E+0X^1$

CALIBRATION SUMMARY:

Max Uncertainty : 0,059992 [%]
 Max Uncertainty : 2,462796 [kPa]
 RSQ : 0,999998
 Calibration points : 36



Magnus Perkunder
 Magnus Perkunder

CALIBRATION VALUES

<u>Value [kPa]</u>	<u>Voltage [V]</u>	<u>Best Poly Fit [kPa]</u>	<u>Deviation [kPa]</u>	<u>Uncertainty [%]</u>	<u>Uncertainty [kPa]</u>
<u>3103,729123</u>	<u>5,547422</u>	<u>3103,497381</u>	<u>0,231742</u>	<u>0,033283</u>	<u>1,033025</u>
<u>3604,484477</u>	<u>6,121357</u>	<u>3605,511172</u>	<u>-1,026695</u>	<u>0,026561</u>	<u>0,957393</u>
<u>4105,239832</u>	<u>6,700660</u>	<u>4112,219973</u>	<u>-6,980141</u>	<u>0,059992</u>	<u>2,462796</u>
<u>4605,995187</u>	<u>7,267828</u>	<u>4608,314539</u>	<u>-2,319353</u>	<u>0,034186</u>	<u>1,574594</u>
<u>5106,750542</u>	<u>7,836756</u>	<u>5105,948736</u>	<u>0,801806</u>	<u>0,014788</u>	<u>0,755184</u>
<u>5607,505896</u>	<u>8,410169</u>	<u>5607,506365</u>	<u>-0,000469</u>	<u>0,014702</u>	<u>0,824432</u>
<u>6108,261251</u>	<u>8,984250</u>	<u>6109,647476</u>	<u>-1,386225</u>	<u>0,015574</u>	<u>0,951280</u>
<u>6609,016606</u>	<u>9,556014</u>	<u>6609,762633</u>	<u>-0,746027</u>	<u>0,016717</u>	<u>1,104856</u>
<u>6909,469819</u>	<u>9,898678</u>	<u>6909,486803</u>	<u>-0,016984</u>	<u>0,017510</u>	<u>1,209851</u>
<u>6909,469819</u>	<u>9,898446</u>	<u>6909,283161</u>	<u>0,186658</u>	<u>0,017531</u>	<u>1,211282</u>
<u>6609,016606</u>	<u>9,555369</u>	<u>6609,198383</u>	<u>-0,181777</u>	<u>0,016735</u>	<u>1,106024</u>
<u>6108,261251</u>	<u>8,983413</u>	<u>6108,915901</u>	<u>-0,654650</u>	<u>0,015533</u>	<u>0,948775</u>
<u>5607,505896</u>	<u>8,406074</u>	<u>5603,924604</u>	<u>3,581292</u>	<u>0,014779</u>	<u>0,828735</u>
<u>4105,239832</u>	<u>6,690609</u>	<u>4103,428524</u>	<u>1,811308</u>	<u>0,019247</u>	<u>0,790143</u>
<u>3604,484477</u>	<u>6,117388</u>	<u>3602,039343</u>	<u>2,445135</u>	<u>0,024806</u>	<u>0,894141</u>
<u>3103,729123</u>	<u>5,548200</u>	<u>3104,177707</u>	<u>-0,448584</u>	<u>0,033252</u>	<u>1,032055</u>
<u>3103,729123</u>	<u>5,547679</u>	<u>3103,721788</u>	<u>0,007335</u>	<u>0,033253</u>	<u>1,032081</u>
<u>3604,484477</u>	<u>6,118708</u>	<u>3603,194154</u>	<u>1,290324</u>	<u>0,024729</u>	<u>0,891340</u>
<u>4105,239832</u>	<u>6,694043</u>	<u>4106,431816</u>	<u>-1,191984</u>	<u>0,026573</u>	<u>1,090874</u>
<u>4605,995187</u>	<u>7,262687</u>	<u>4603,817640</u>	<u>2,177547</u>	<u>0,015942</u>	<u>0,734283</u>
<u>5106,750542</u>	<u>7,837169</u>	<u>5106,310203</u>	<u>0,440338</u>	<u>0,014664</u>	<u>0,748877</u>
<u>5607,505896</u>	<u>8,410631</u>	<u>5607,910374</u>	<u>-0,404478</u>	<u>0,014717</u>	<u>0,825236</u>
<u>6108,261251</u>	<u>8,983330</u>	<u>6108,842940</u>	<u>-0,581689</u>	<u>0,015542</u>	<u>0,949358</u>
<u>6609,016606</u>	<u>9,555139</u>	<u>6608,996941</u>	<u>0,019664</u>	<u>0,016890</u>	<u>1,116273</u>
<u>6909,469819</u>	<u>9,898123</u>	<u>6909,001498</u>	<u>0,468321</u>	<u>0,017543</u>	<u>1,212122</u>
<u>6609,016606</u>	<u>9,555032</u>	<u>6608,903666</u>	<u>0,112940</u>	<u>0,016757</u>	<u>1,107442</u>
<u>6108,261251</u>	<u>8,982434</u>	<u>6108,059647</u>	<u>0,201605</u>	<u>0,015555</u>	<u>0,950134</u>
<u>5607,505896</u>	<u>8,410410</u>	<u>5607,716628</u>	<u>-0,210732</u>	<u>0,014740</u>	<u>0,826519</u>
<u>5106,750542</u>	<u>7,837503</u>	<u>5106,602057</u>	<u>0,148484</u>	<u>0,014743</u>	<u>0,752863</u>
<u>4605,995187</u>	<u>7,263820</u>	<u>4604,808683</u>	<u>1,186504</u>	<u>0,016036</u>	<u>0,738602</u>
<u>4105,239832</u>	<u>6,692005</u>	<u>4104,649499</u>	<u>0,590333</u>	<u>0,019958</u>	<u>0,819315</u>
<u>3604,484477</u>	<u>6,119971</u>	<u>3604,298116</u>	<u>0,186361</u>	<u>0,024642</u>	<u>0,888221</u>
<u>3604,484477</u>	<u>6,119951</u>	<u>3604,280651</u>	<u>0,203826</u>	<u>0,024639</u>	<u>0,888098</u>
<u>3103,729123</u>	<u>5,547910</u>	<u>3103,924188</u>	<u>-0,195065</u>	<u>0,033198</u>	<u>1,030385</u>
<u>4605,995187</u>	<u>7,264413</u>	<u>4605,327252</u>	<u>0,667935</u>	<u>0,015897</u>	<u>0,732198</u>
<u>5106,750542</u>	<u>7,838146</u>	<u>5107,165148</u>	<u>-0,414606</u>	<u>0,014712</u>	<u>0,751303</u>

COMMENTS:

The uncertainty is calculated with 95% confidence. The uncertainty includes the randomness in the calibrated instrument during the calibration, systematic uncertainty in the instrument or property which the instrument under calibration is compared with (dead weight manometer, calibrated weights etc.), and due to regression analysis to fit the calibration points to a linear calibration equation. The calculated uncertainty can be used as the total systematic uncertainty of the calibrated instrument with the given calibration equation.

Appendix D



Figure 10.3: Picture of pressure transducer placed on the draft tube of turbine 1.



Figure 10.4: Picture of pressure transducer placed on the draft tube of turbine 2.



Figure 10.5: Picture of pressure transducer placed on the draft tube of turbine 3.



Figure 10.6: Picture of pressure transducer placed on the draft tube of turbine 4.



Figure 10.7: Picture of pressure transducer placed upstream the bulb valve, (PU1, PU2, PU3, PU4). The mounting is similar on all the turbines.



Figure 10.8: Picture of pressure transducer placed downstream the bulb valve, (PD1, PD2, PD3, PD4). The mounting is identical on all the turbines.

Appendix E

fft of Turbine 4 measurement nr. 60-90
Case: Turbine 4: Bulb valve closed

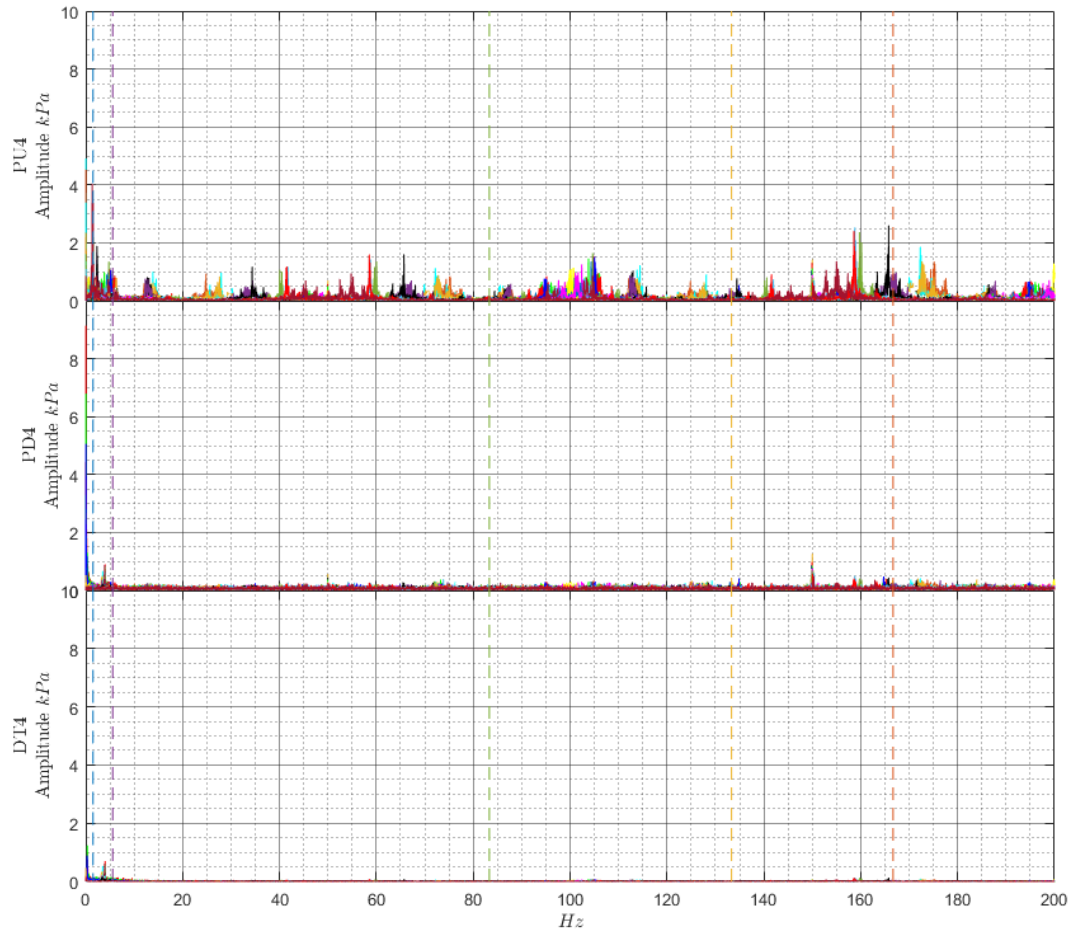


Figure 10.9: Spectral analysis of measurement 93-98, Turbine 4.

fft of Turbine 3 measurement nr. 60-90
Case: Turbine 4: Bulb valve closed

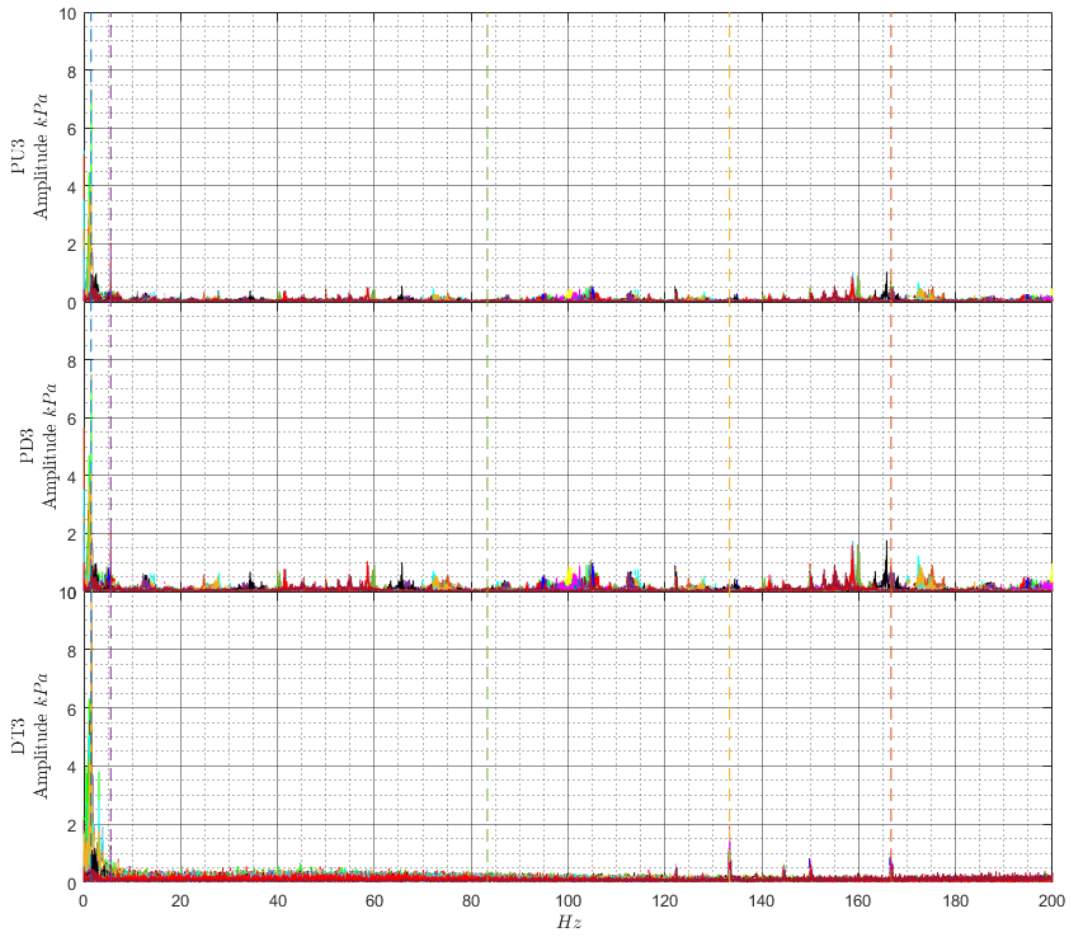


Figure 10.10: Spectral analysis of measurement 60-90, Turbine 3.

fft of Turbine 2 measurement nr. 60-90
Case: Turbine 4: Bulb valve closed

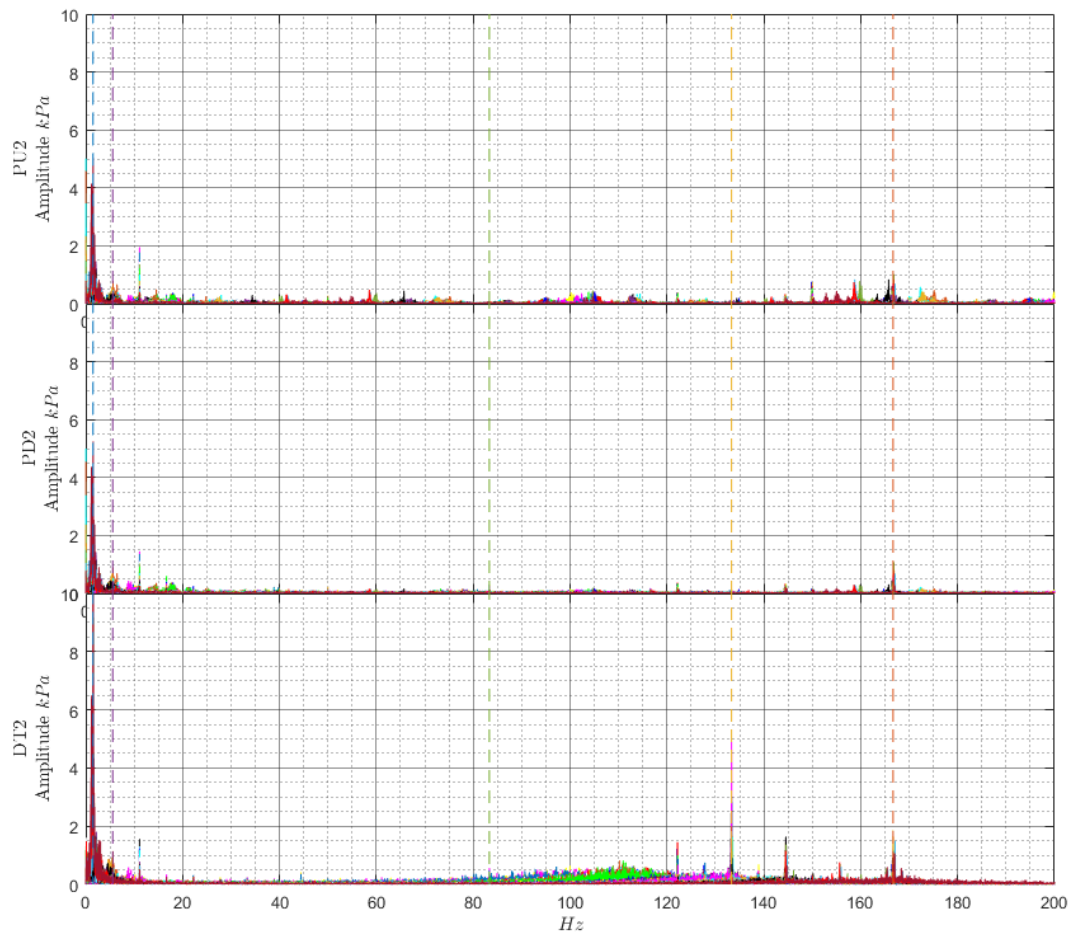


Figure 10.11: Spectral analysis of measurement 60-90, Turbine 2.

fft of Turbine 1 measurement nr. 60-90
Case: Turbine 4: Bulb valve closed

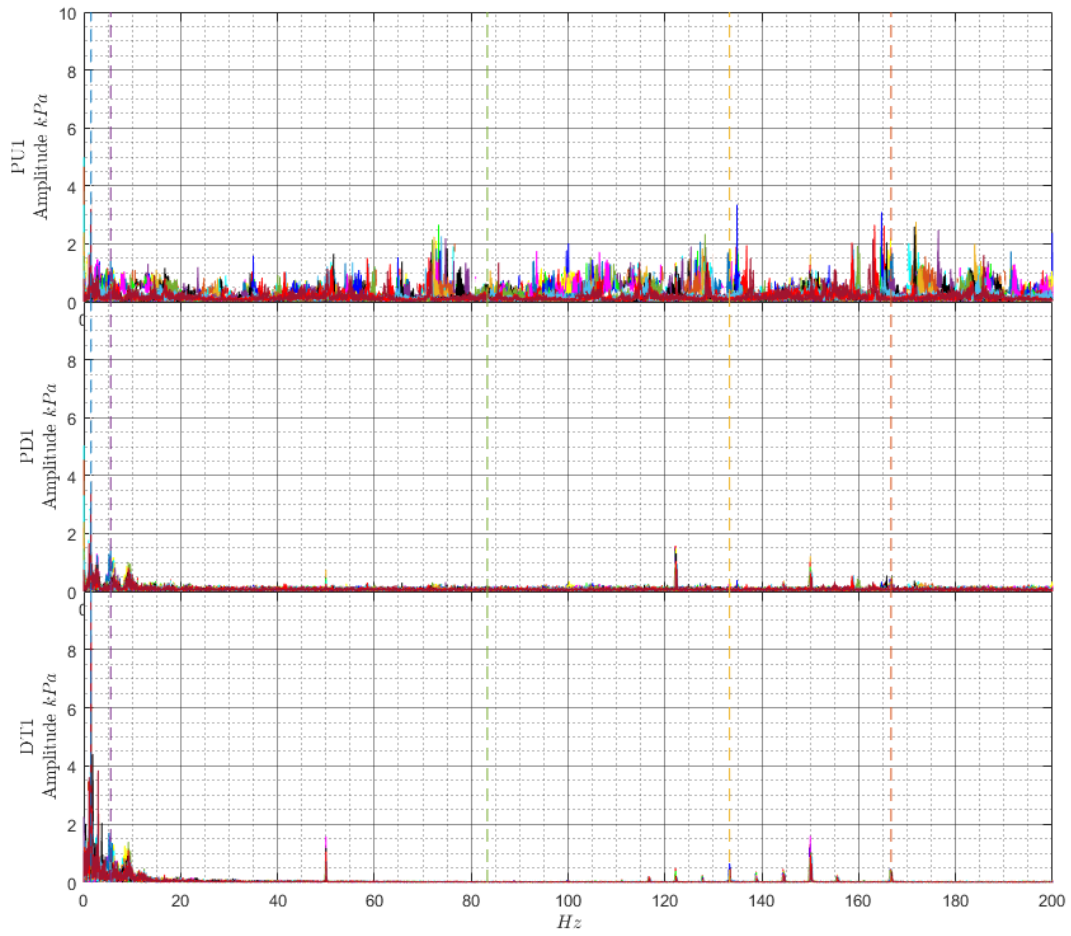


Figure 10.12: Spectral analysis of measurement 60-90, Turbine 1.

fft of Turbine 4 measurement nr. 93-98
Case: Turbine 4 & 3: Bulb valve closed

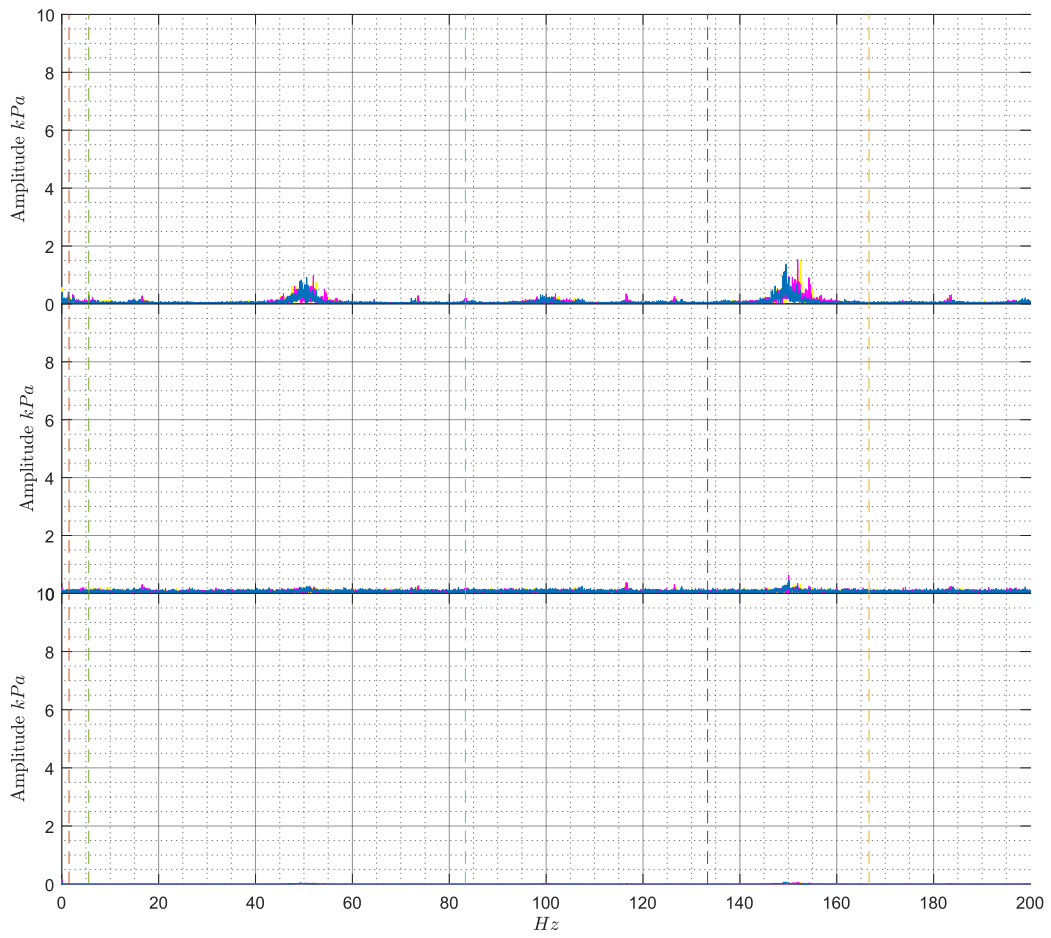


Figure 10.13: Spectral analysis of measurement 93-98, Turbine 4.

fft of Turbine 3 measurement nr. 93-98
Case: Turbine 4 & 3: Bulb valve closed

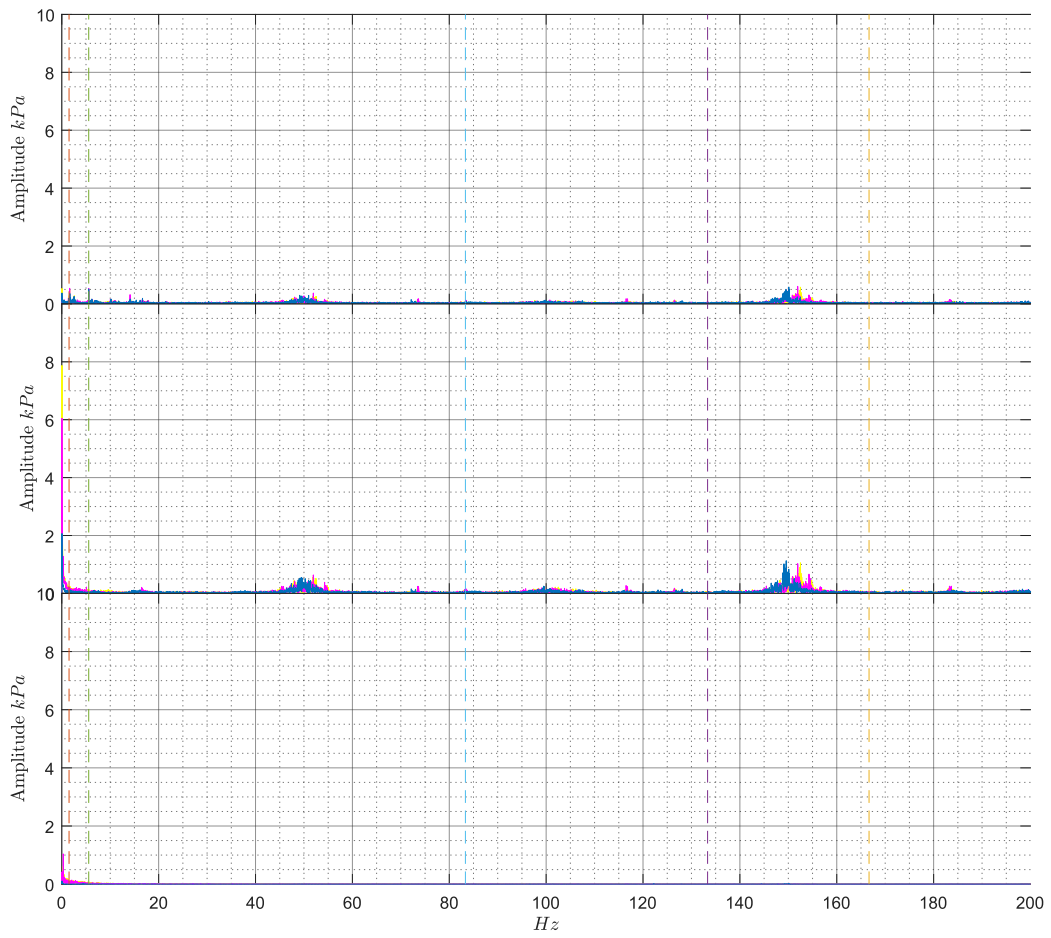


Figure 10.14: Spectral analysis of measurement 93-98, Turbine 3.

fft of Turbine 2 measurement nr. 93-98
Case: Turbine 4 & 3: Bulb valve closed

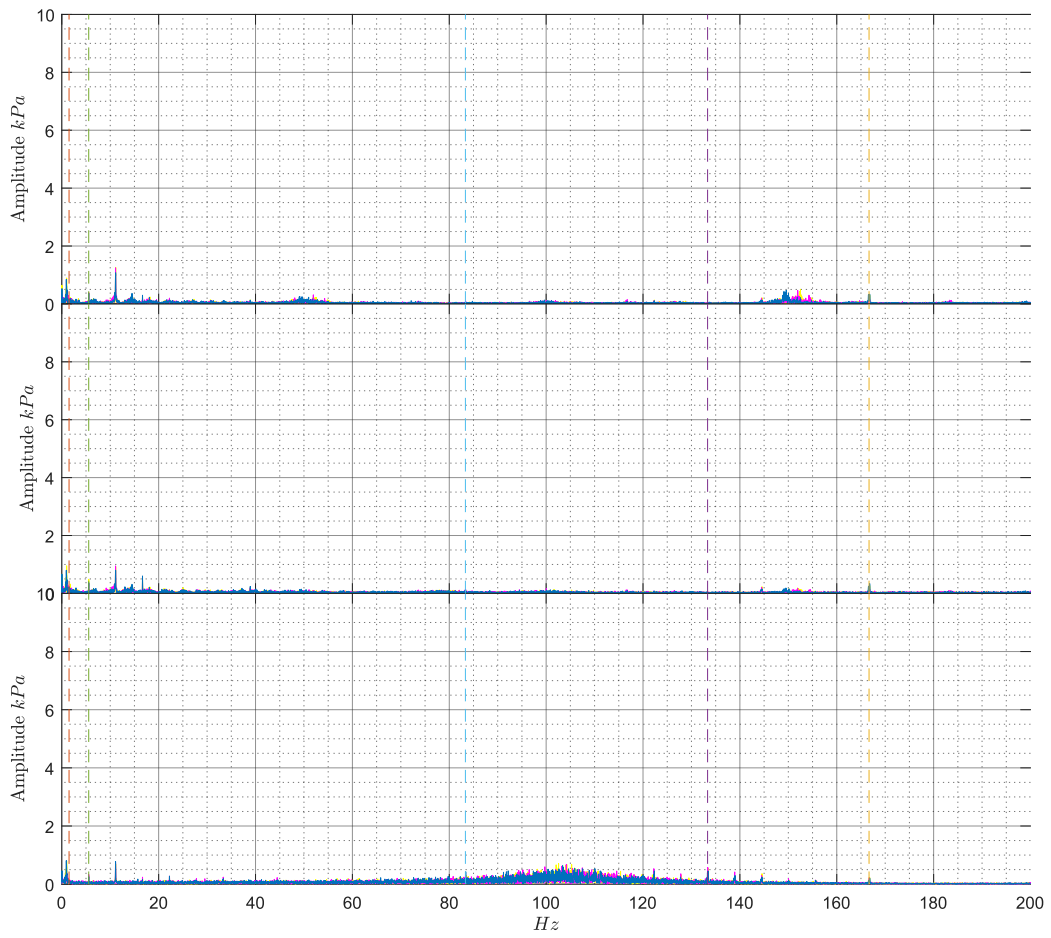


Figure 10.15: Spectral analysis of measurement 93-98, Turbine 2.

fft of Turbine 1 measurement nr. 93-98
Case: Turbine 4 & 3: Bulb valve closed

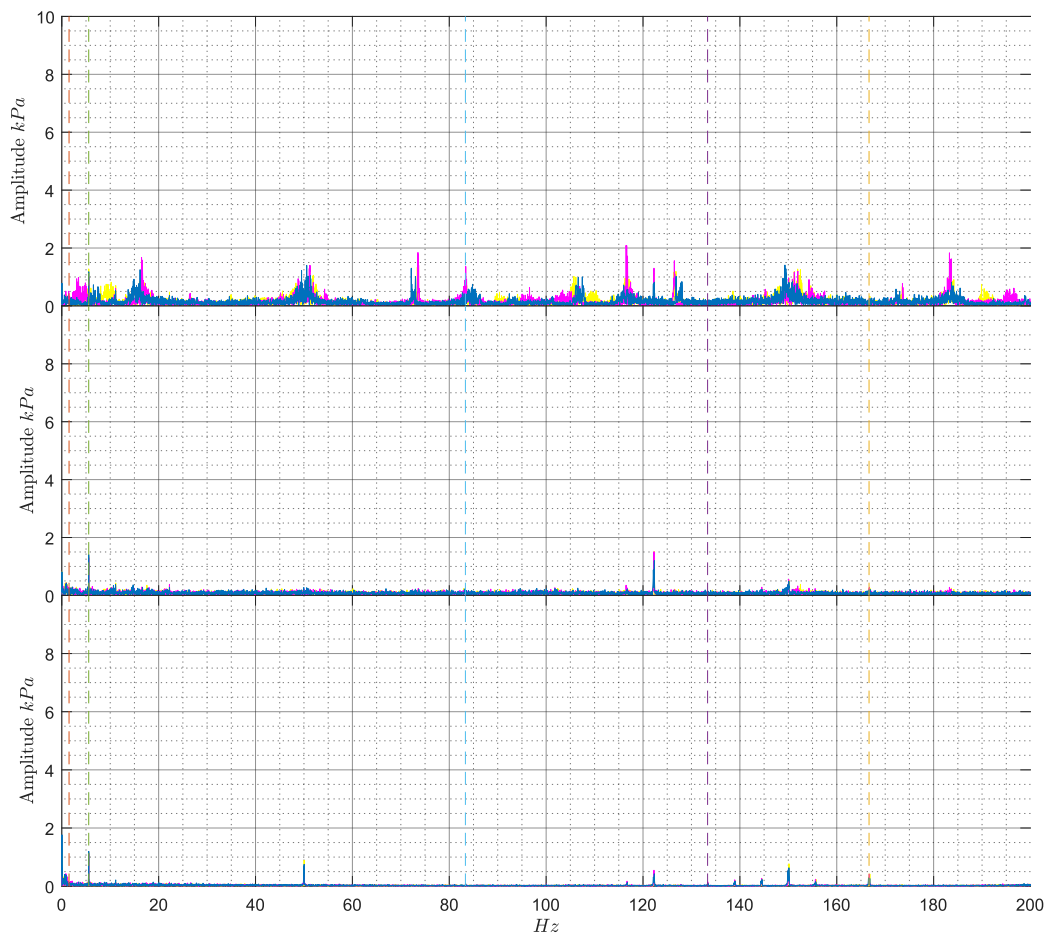


Figure 10.16: Spectral analysis of measurement 93-98, Turbine 1.

fft of Turbine 4 measurement nr. 99-111
Case: Turbine 3: Bulb valve closed

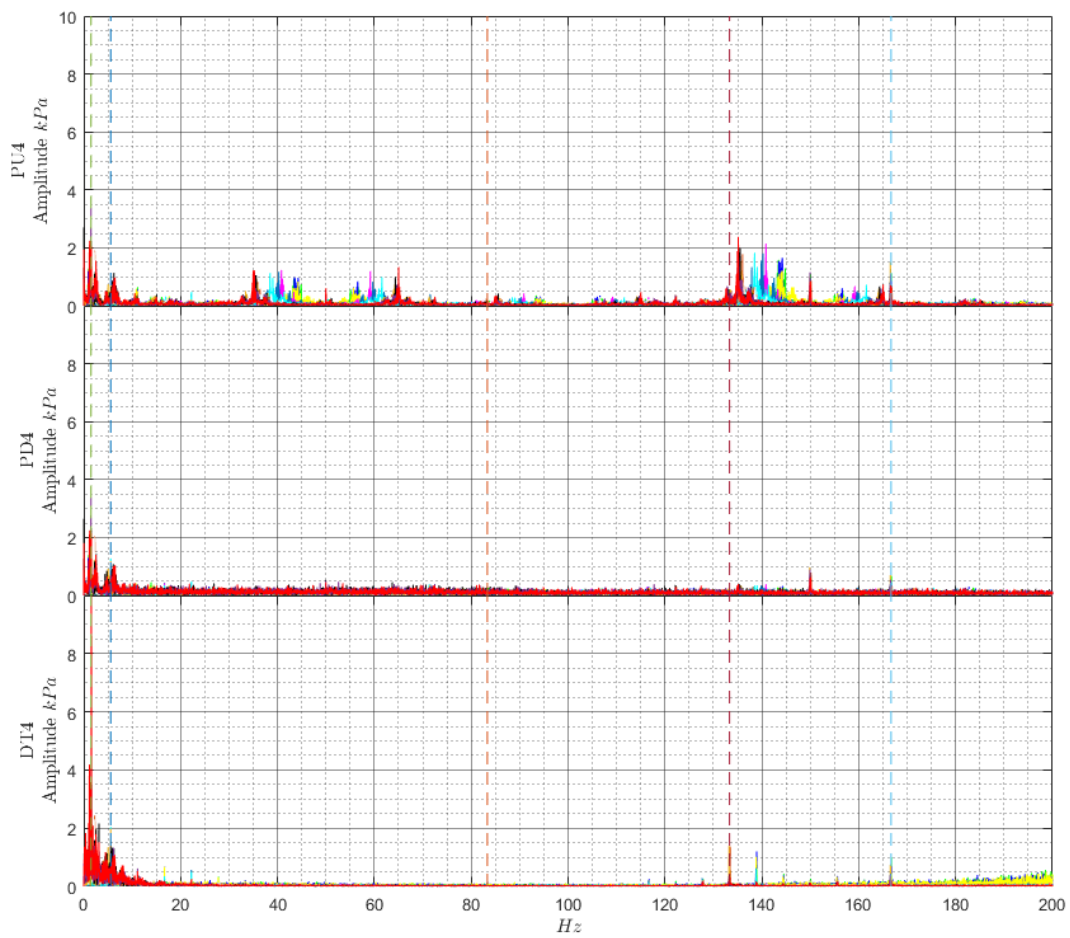


Figure 10.17: Spectral analysis of measurement 99-111, Turbine 4.

fft of Turbine 3 measurement nr. 99-111
Case: Turbine 3: Bulb valve closed

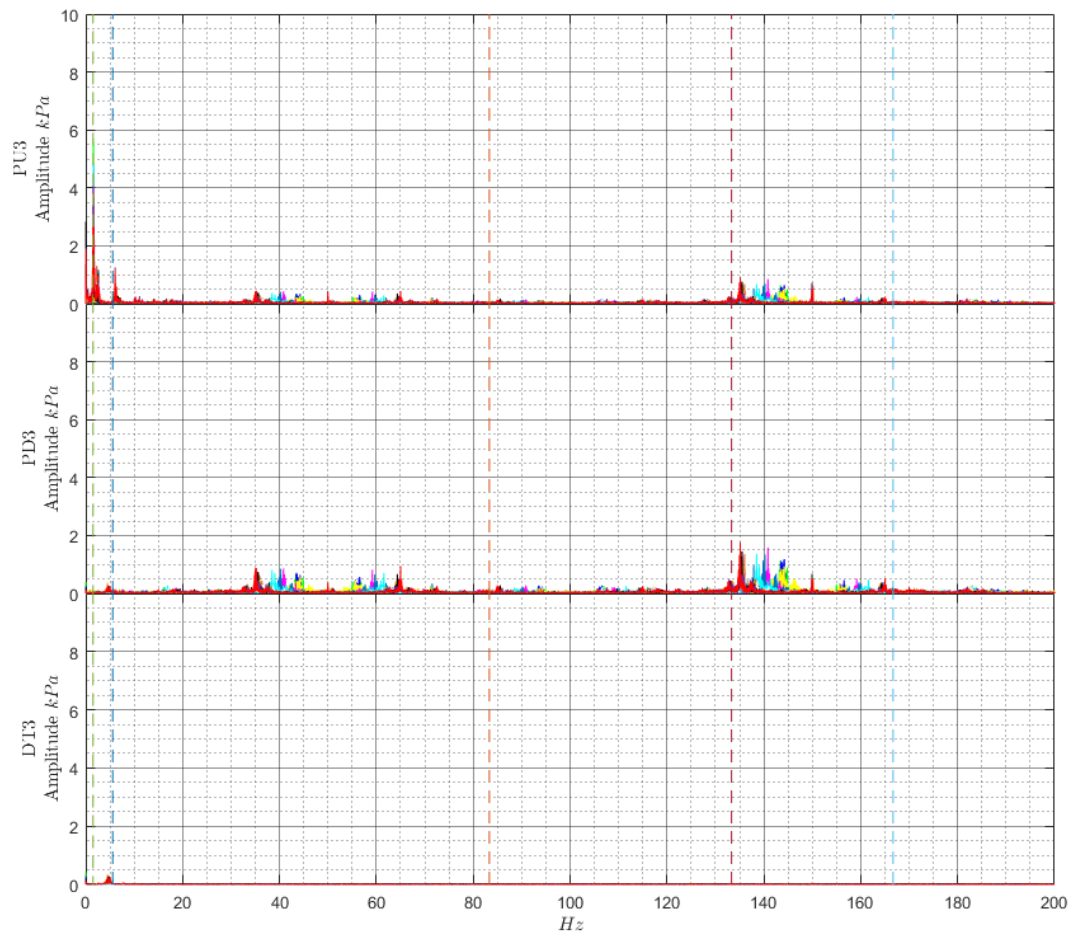


Figure 10.18: Spectral analysis of measurement 99-111, Turbine 3.

fft of Turbine 2 measurement nr. 99-111
Case: Turbine 3: Bulb valve closed

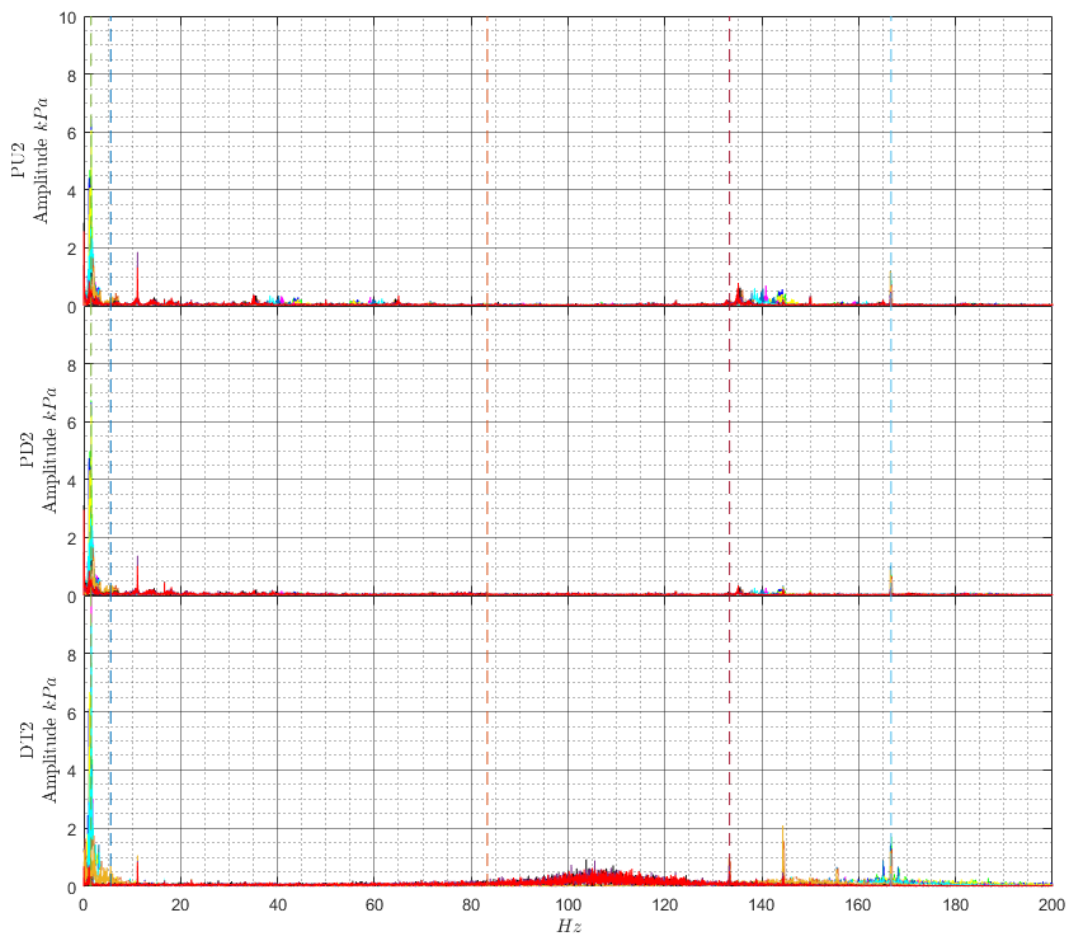


Figure 10.19: Spectral analysis of measurement 99-111, Turbine 2.

fft of Turbine 1 measurement nr. 99-111
Case: Turbine 3: Bulb valve closed

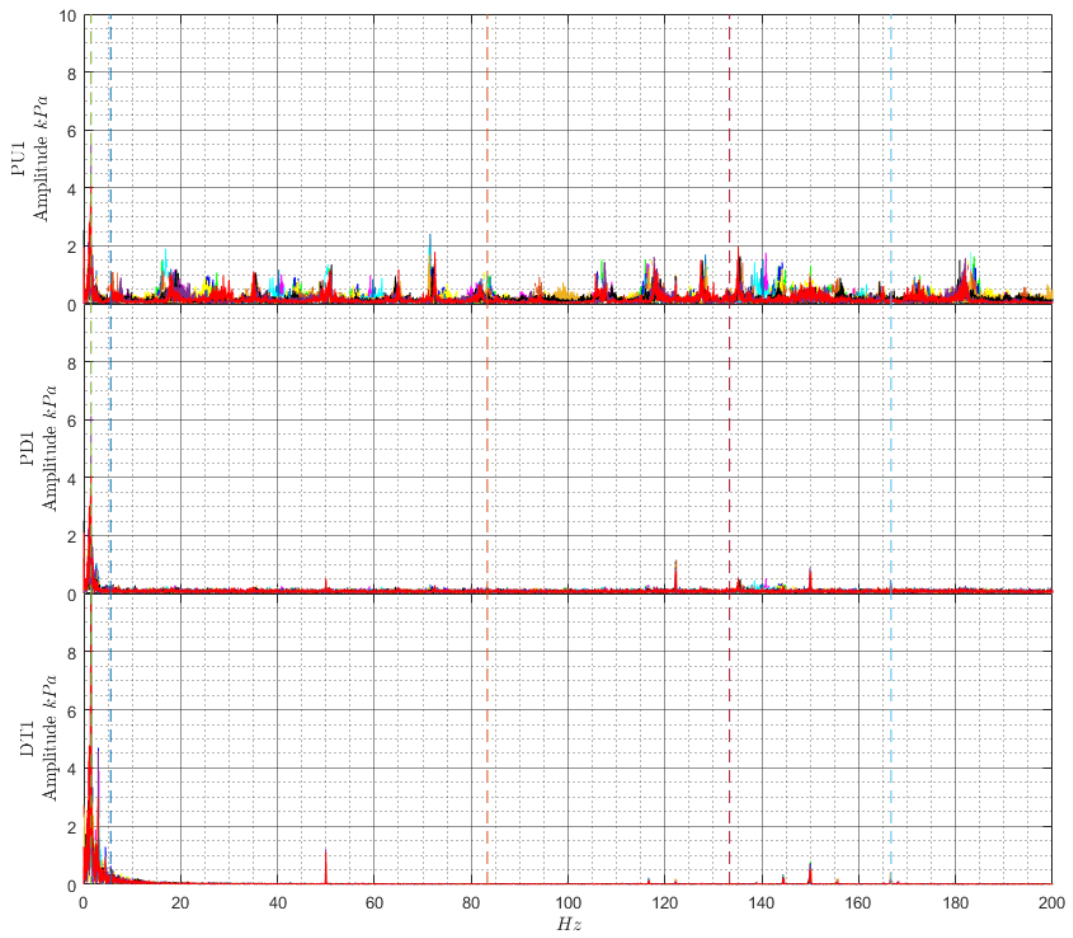


Figure 10.20: Spectral analysis of measurement 99-111, Turbine 1.

Appendix F

Investigation of fluid transients in a penstock attached to a Francis turbine rig using seismic interferometry

Magnus Farstad Perkunder^{1*}, Torbjørn K. Nielsen¹ and Celine Faudot¹

¹*Department of Energy and Process Engineering, NTNU, Hydropower laboratory, Norway*

** Corresponding author (magns.pk@gmail.com)*

Abstract. Pressure fluctuations in hydropower plants contribute to fatigue loads. Pressure pulsations generated by a reaction turbine will create fluid transients in the attached system which can increase the load on structural parts if resonance occurs. Several factors govern transients in a pipe system where the main parameters are the length between reflection points and the propagation velocity. This paper investigates how to find the propagation velocity of pressure waves measured in the penstock at the Hydropower Laboratory at NTNU by applying techniques from seismic interferometry. A simple 1-D model has been developed using the method of characteristics to compare the experimental results to a known system. Seismic interferometry is widely used in the oil and gas industry, and the basic principle is to obtain the Green's function between measured signals. The results from the experimental data and simulations are promising, but further research is needed to optimize both data acquisition and post processing.

1. Introduction

Reaction turbines operate by converting both pressure energy and kinetic energy in the flow to mechanical energy at the shaft [4]. For reaction turbines, there is a direct connection between the flow through the turbine and the flow in the conduit. Pressure fluctuations originating from a reaction turbine at steady state will propagate in the conduit and may cause a resonance condition in the power plant [3] [5] [6]. Resonance condition in a pipe system means that a disturbance in the system amplifies with time rather than being dampened. Consequences may be severe pressure and flow fluctuation [6].

The wave speed a and pipe lengths L govern if resonance condition can arise in a conduit system [1]. The water hammer effect describes how pressure pulses propagate in a pipe, i.e. a pipe with constant length and wave speed a will have a fundamental period $T_f = 4L/a$. A cyclic pressure fluctuation with amplitude A_p and frequency $f_p = 1/T_f$ will provoke resonance condition if the amplitude is large enough [6]. In addition to the fundamental harmonic higher harmonics can cause resonance condition. The total theoretical resonance frequency of a system is expected to be an odd harmonic [5].

Dörfler et al., presents a case where a power plant with four Francis turbines with separate penstocks experience resonance condition at high load. During tests for a new air injection system, significant differences in terms of power swings were detected. Dörfler et al. imply that variations in penstock length caused these differences [3]. Several cases of power plants experiencing resonance related to higher harmonic frequencies in the conduit are presented in [5].

To further improve the understanding of dynamic behavior in the penstock in a hydropower plant seismic interferometry has been applied to measurements conducted at the Hydropower laboratory at NTNU. The goal with the measurements and post-processing is to evaluate if seismic interferometry is applicable to determine the wave speed in a short pipe section. The level of noise in signals from pressure measurements in the conduit is high since the turbine, generator and other sources generate fluctuations. Measured data with a high level of noise are challenging to interpret without well-designed processing methods.

Interferometry is based on studying the interference phenomena between a pair of signals and thereby obtain information about differences [8]. The term originates from radio astronomy, where it refers to the cross-correlation methods applied to radio signals from distant objects [9]. The first to derive seismic interferometry theory was Claerbout in 1968 [10]. Since then different methods have been developed, and research has been done to improve techniques [7] [8] [18]. Seismic interferometry is divided into two main groups called controlled-source and passive seismic interferometry. In all cases, the response recorded at one receiver can be treated as there were a source at the other. Seismic interferometry is also often called Greens function retrieval since a point source response is equal to a Greens function convolved with a wavelet [8].

The measured response at points along a pipe section should unveil how fast pressure waves propagate and how distorted the signal gets from one point to another [11].

2. Basic Theory

2.1. Direct wave interferometry:

Pipe flow is often treated as 1-D flow [1]. With this in mind direct wave interferometry is described as by Waapenaar et al., [9] in the following manner:

Figure 1a illustrates how an impulse at location x_s at time t_0 radiates a plane wave in friction less medium with propagation velocity a . The wave propagates to the right along the x-axis.

At location x_A and x_B there are receivers. Figure 1b shows the recorded response at x_A at time t_A and figure 1c shows the response at x_B at time t_B . The responses are denoted $G(x_A, x_s, t)$ and $G(x_B, x_s, t)$. G stands for Green's function as the responses represent the Green's function between x_A or x_B with x_s . In figure 1 the source at x_s is an impulse and the Green's function at x_i is $G(x_i, x_s, t) = \delta(t - t_i)$ where $t_i = (x_i - x_s)/a$. δ is the dirac delta function.

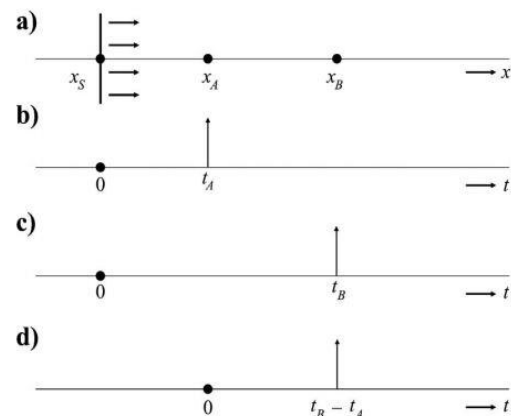


Figure 1. 1-D Wave propagating in friction less homogeneous fluid. Taken from [9].

Cross correlating the responses at x_A and x_B result in an impulse at $t_B - t_A$ shown in figure 1d. Since the responses at x_A and x_B have the same path from x_s to x_A the travel time $t_A - t_s$ cancels during cross-correlation. The result is that the impulse in figure 1d can be treated as there were a source at x_A measured at x_B i.e., the Green's function $G(x_B, x_A, t)$. Note that the source and propagation velocity is not needed. The same is true for the time of t_s since both responses are shifted the same amount.

More precisely the cross-correlation of the impulses at x_A and x_B is represented by $G(x_B, x_s, t) * G(x_A, x_s, -t)$ where the asterisk denotes temporal convolution. The time reversal of the second

Green's function turns the convolution into a correlation.

$$G(x_B, x_A, t) = G(x_B, x_S, t) * G(x_A, x_S, -t) \quad (1)$$

Equation (1) shows that the cross-correlation at two receivers gives the response at one of those receivers as if there were a source at the other. It also shows why seismic interferometry is often called Green's function retrieval. The source does not necessarily need to be an impulse it can also be a signal. If the signal is a wavelet $S(t)$ then the response at x_B and x_A can be written as

$$u(x_A, x_S, t) = G(x_A, x_S, t) * S(t) \quad \text{and} \quad u(x_B, x_S, t) = G(x_B, x_S, t) * S(t).$$

The cross-correlation of the responses at two receivers gives the Green's function between these receivers convolved with the auto correlation of the source function. This is expressed in equation (2).

$$G(x_B, x_A, t) * S_S(t) = u(x_B, x_S, t) * u(x_A, x_S, -t) \quad (2)$$

For retrieving the cross-correlation of two receivers in a field of random noise some additional steps are needed since the noise propagates in both directions. The steps are derived by Waapnar et al., in [8] and yields equation (3).

$$\{G(x_B, x_A, t) + G(x_B, x_A, -t)\} * S_N(t) = \langle u(x_B, t) * u(x_A, -t) \rangle \quad (3)$$

$S_N(t)$ is the autocorrelation of the random noise source, $\langle \dots \rangle$ indicates ensemble averaging, $u(x_i, t)$ are the responses at x_i . figure 2 illustrates the result of cross correlating the response at two receivers in a homogeneous distributed random noise field. The peak response in the cross-correlation plot acts as if it was a source at the other receiver.

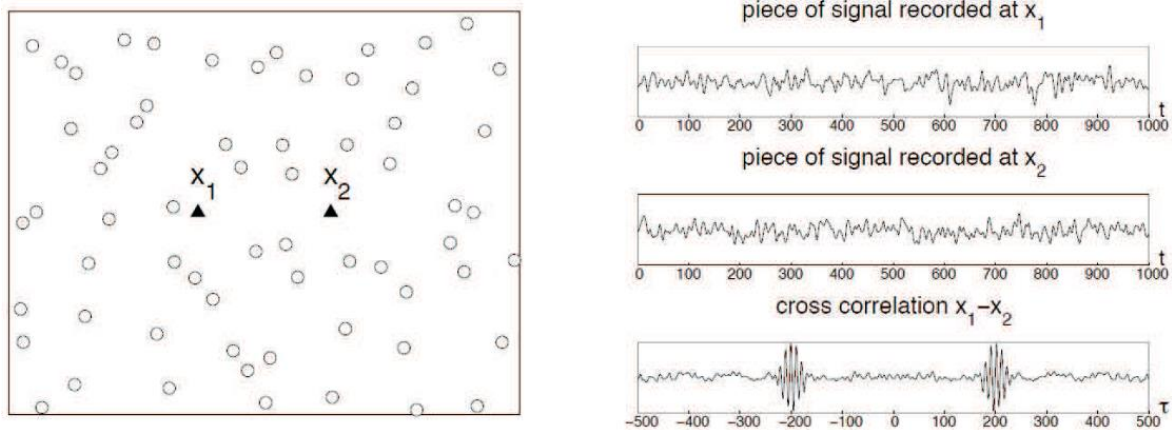


Figure 2. Homogeneous distribution of random noise around two receivers. Taken from [17].

The cross-correlation between two receivers in a medium with a homogeneous distribution of noise should be nearly symmetrical around $\tau = 0$ as in figure 2. Meaning that the positive and negative parts correspond to the Green's function and its anticausal counterpart [15] [16]. The causal and anticausal parts can be seen as the response peaks at the positive and negative τ -axis in the cross-correlation plot in figure 2. In reality, the causal and anticausal response may differ a lot in amplitude. The difference in amplitude is caused by differences in the energy flux in the traveling waves between two receivers. The effect of disturbances can be seen in figure 3.

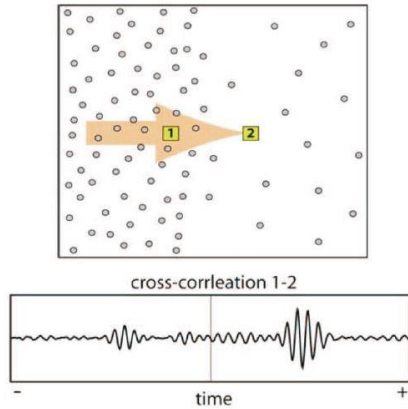


Figure 3. Cross-correlation response if noise sources are distributed in a non-homogeneous fashion. Taken from [11].

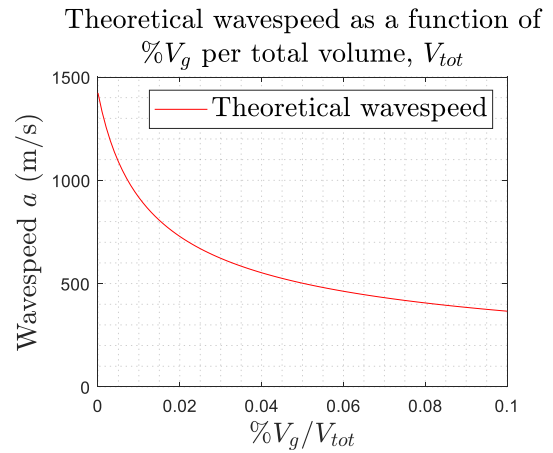


Figure 4. Wave speed plot recreated in MATLAB from [1]. (Static pressure 324 kPa)

2.2. Wave speed

A homogenous fluid in a completely filled pipe has a wave speed as described by equation (4) [1] [2]. A calculated example is presented under to get an indication of the expected wave speed in the Laboratory. The diameter and thickness used to calculate a are equal to the values in the hydropower laboratory at NTNU. The other values are as proposed in examples written by Wylie and Streeter [1]. The variation in a is due to different cases of pipe support. Well-fastened pipes have a lower wave speed than pipes only fastened in one end. Different ways to model ψ are proposed in [1] [2].

$$a^2 = \frac{K}{\rho \left(1 + \frac{D}{e} \frac{K}{E} \psi\right)} \quad (4)$$

Calculated wave speed using equation (4). ρ = Density of liquid (999 kg/m³), K = Volumetric compressibility modulus of liquid (2.2 GPa), D = Diameter of pipe (0.35 m), e = Thickness of pipe (0.01 m), E = Modulus of elasticity pipe (207.7 GPa), ψ = Pipe support parameter [1], a = theoretical wave speed (1261-1288 m/s)

As expressed in equation (4) the wave speed is dependent on several parameters. In addition to these, the effect of air entrainment is dominant as seen in figure 4. Wylie and Streeter recommend new expressions for both compressibility and density if air is present. The new expressions for K and ρ are functions of the amount of air in the mixture as well as the related parameter values, i.e. K_{water} , K_{air} , ρ_{water} , ρ_{air} . Variables related to the pipe are neglected in the new expression for the wave speed since the effect of air entrainment is dominant. figure 4 illustrates how a theoretical wave speed behaves as a function of the percentage of air per total volume [1]. The plot is recreated from [1] where it is validated with experimental data at a static pressure of 324 kPa.

3. Experimental Setup

3.1. Francis Test Rig

Measurements were conducted at the Waterpower laboratory at NTNU on the Francis model test rig. The rig was operated in open loop configuration and follows the steps (1-9) illustrated in figure 5. The open loop configuration used during the experiments maintained a head $H \approx 12.5$ (m). The guide

vanes were kept at maximum opening $\alpha = 14$ (degrees) to minimize obstruction of pressure fluctuations from the turbine, and to maximize rotor stator interaction [13].

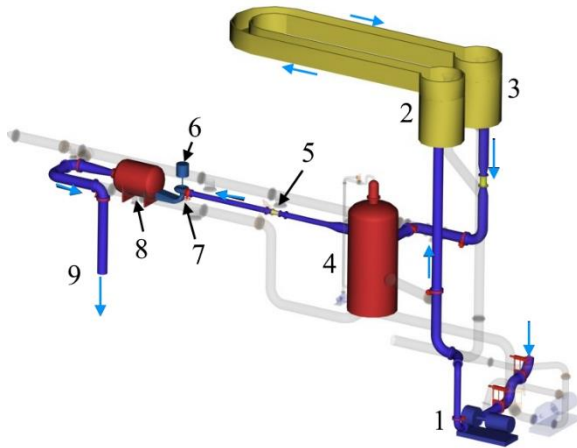


Figure 5. Open loop configuration. (1) centrifugal pump, (2) and (3) open water channel, (4) upstream pressure tank, (5) flowmeter, (6) generator, (7) Francis turbine, (8) downstream pressure tank, (9) water outlet to basement.

3.2. Pressure Sensors

The placements of the pressure sensors are illustrated in figure 6 which is a 2D presentation of (4), (5), (6), (7) and (8) in figure 1. The pressure sensors were placed along the penstock between the pressure tank (4) and the turbine inlet (7). Ideally, all sensors should have been mounted flush with the inner wall of the pipe to prevent disturbances and measurement uncertainties. A recessed sensor will have an added water column which will disturb the measurements [12]. Table 1 presents sensor type, placement, and mounting method.

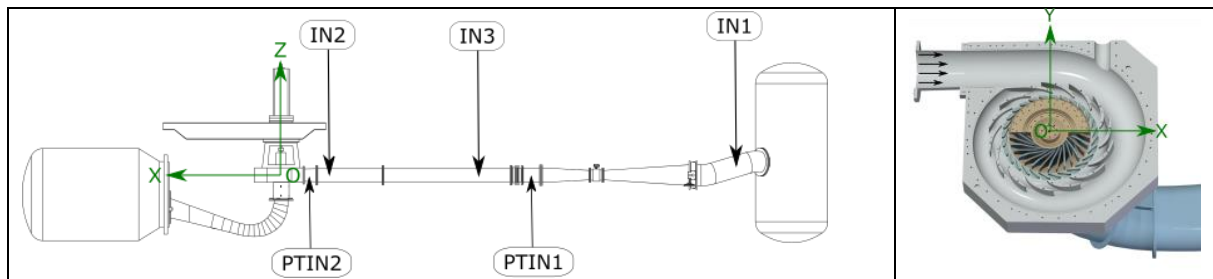


Figure 6. Overview of sensor setup

Sensor	Placement mm				Type	Mounting
	x	y	z	$\pm\mu$		
PTIN2	-880	0	0	6	Kuhlite KHM 375	Flush
IN3	-1136	0	0	10	Unik5000	recessed
IN2	-6453	0	0	30	Unik5000	recessed
PTIN1	-7801	0	0	3	Kuhlite KHM 375	flush
IN1	-13550*	0	0	?	Unik5000	recessed

Table 1. * indicates that the placement is not measured accurately. μ is the uncertainty related to the measured placement in mm.

Figure 7 illustrates how sensors PTIN2 and IN3 are mounted. IN3 which is recessed has a small column of water between the sensor and the main flow which may cause disturbances. Both sensor types have a sample rate more than 10 times the expected input signal. Static calibration of the transducers was performed following guidelines in IEC60193 [14]. Dynamic calibration should have been performed,

but necessary equipment was unavailable. The sensor IN1 is placed in a bend close to the pressure tank, accurate measurements of the placement were challenging to perform.



Figure 7. Recessed and flush mounted pressure sensor. Picture is rotated 90 degrees to the right. (Sensors are mounted on the lower part of the pipe).

3.3. Measurement Procedure

The measurements were conducted with constant maximum guide vane opening set to 14 degrees. The speed of the turbine was regulated between 300 and 400 rpm with increments of 10 rpm. The pressure sensors were connected to a DAQ-bridge and a LabVIEW program developed at the Waterpower laboratory was used to log the data.

3.4. 1-D Simulation Method of Characteristics

A 1-D simulation model was developed using the method of characteristics in order to compare the measured data with a known system with a set wave velocity and length. The model was validated against an example in [1]. The region modeled is the pipe section between the pressure tank (4) and the turbine (7) in figure 5. Boundary conditions at the inlet (4) and the outlet (7) of the pipe were varied to evoke different results. The pipe section was also divided into several sections with different cross-sections to simulate the flow meter (5) in figure 5.

3.5. Data Post Processing

MATLAB was used to post-process the simulated and measured data. First, a spectral analysis was conducted to identify frequency regions with enough energy to perform interferometry, and also regions with frequencies related to noise which were removed. Data from all sensors were cross-correlated with PTIN2 as a reference using the `xcorr`-function in MATLAB. Further improvement of the visualization was attempted by using the `deconvwnr`-function in MATLAB. The results from both methods were filtered with a band-pass filter and plotted with the `wiggle`-function in MATLAB.

4. Results

Figure 8 shows 0.3 seconds of a 30 second sample of the experimental data measured at PTIN2 and PTIN1. PTIN2 and PTIN1 are the flush mounted pressure transducers.

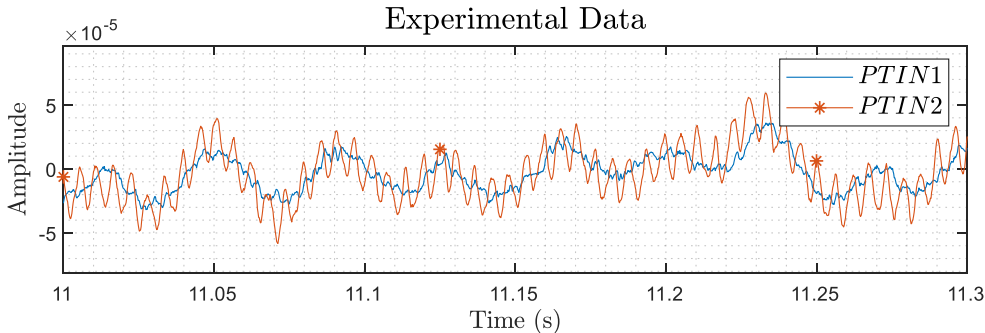


Figure 8. 0.3 (s) of 30 (s) sample measured at PTIN2 and PTIN1. Turbine speed: 350 rpm. Guide vane opening: 14 deg.

Figure 9 presents the spectral analysis of the data from figure 8. The analysis shows that there is much noise in the measurements, but also distinct peaks related to pressure pulsations from the turbine. The blade passing frequency = 175 Hz is the most dominant peak. The peaks at 50 Hz and 300 Hz are related respectively to noise from electrical equipment and noise from machinery. Many other peaks remain unidentified, but could be related to reflections in the conduit and higher harmonics.

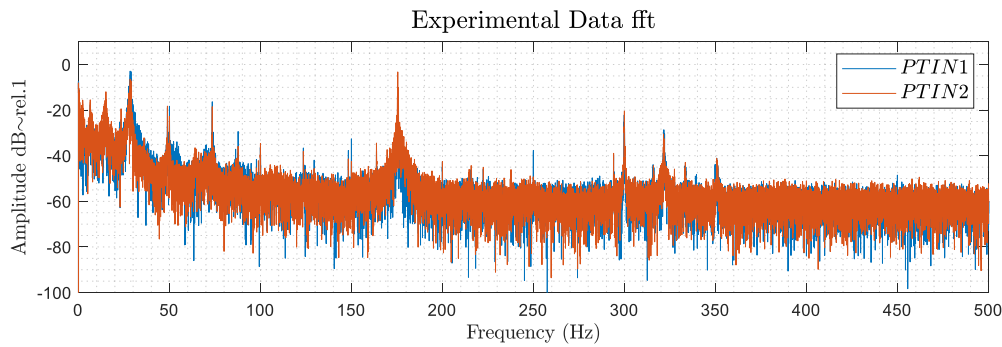


Figure 9. Spectral analysis of PTIN1 and PTIN2
Amplitude dB~rel.1.
Turbine speed: 350 rpm.
Guide vane opening: 14 deg.

Figure 10 shows the filtered Green's function between each receiver and PTIN2. The responses are plotted vertically with the turbine to the left at Distance = 0. Each transducer is plotted with a distance from the turbine equal to the distances in Table 1. The dashed lines are where the response from an impulse given at PTIN2 at $t = 0$ would be largest, given a certain wave speed. The dashed line is fitted to the data by trial and error, the others are only shown for comparison.

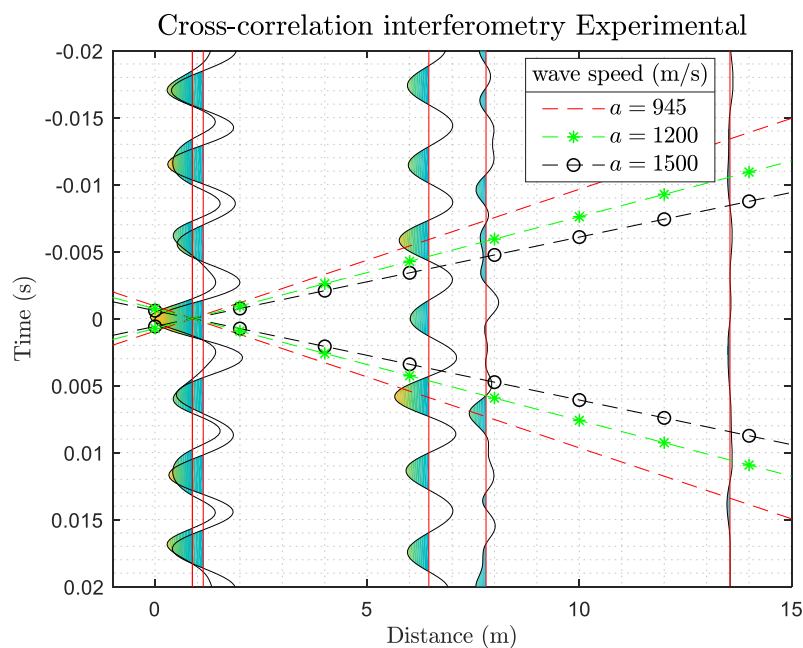


Figure 10. Cross-correlation interferometry applied to experimental data. Several measurements are added to minimize the effects of noise as described by equation (3).

The Greens function with PTIN2 as reference is plotted on the vertical axis with distance spacing as in figure 6. The turbine is at Distance = 0.

The dashed lines resemble the expected path of a response from an impulse at PTIN2 at $t = 0$ given the wave speed a .

Figure 11 shows the deconvolution interferometry of the experimental data. The responses and dashed lines are plotted as in figure 10.

Figure 12 shows the deconvolution interferometry of simulated data. The simulated data has a wave speed equal to 1000 (m/s). The location of where the pressure is retrieved from the simulated model ensures that the exact solution of the characteristic's method is obtained.

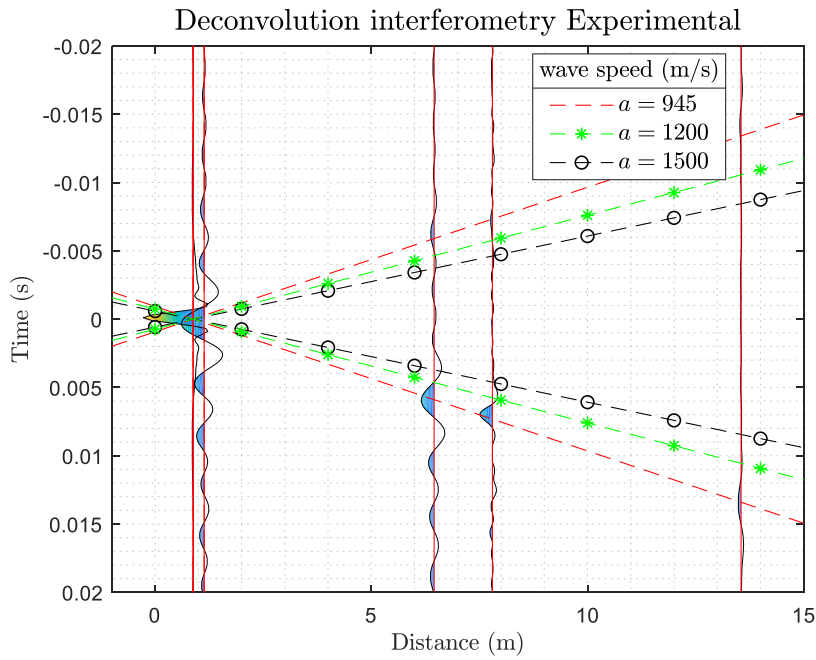


Figure 11. Deconvolution interferometry applied to the same experimental data as in figure 10.

Responses are located as in figure 10 and related to the same pressure sensors.

The dashed lines represent the same paths as in figure 10.

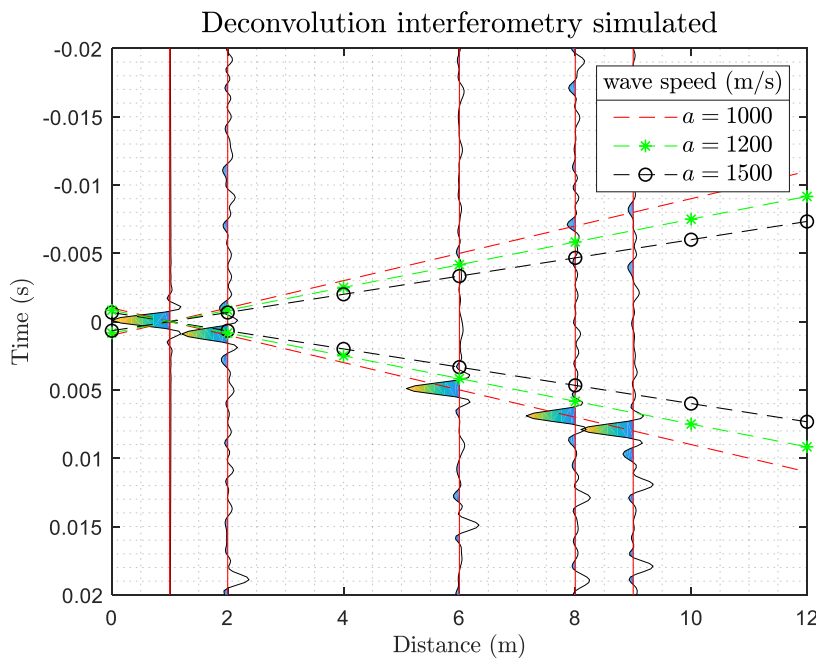


Figure 12. Deconvolution interferometry applied to simulated data. The simulation included a reflection point, friction and wave speed $a = 1000(m/s)$. Boundary condition at outlet was set to give an impulse at the start of the simulation and random noise throughout the simulation time. The inlet was set to constant head.

Figure 13 a shows a 5 second sampling of the numerical simulation. All points in time and space are included, time increment $dt = 0.0002(s)$, and space increment $dx = 0.1(m)$. Data from vertical lines at Distance = (1,2,6,8 and 9) would give the simulated pressure transducers used to produce figure 12. Figure 13 b shows the Green's function retrieved between the nodes at Distance = 0.1 (m) and the other nodes.

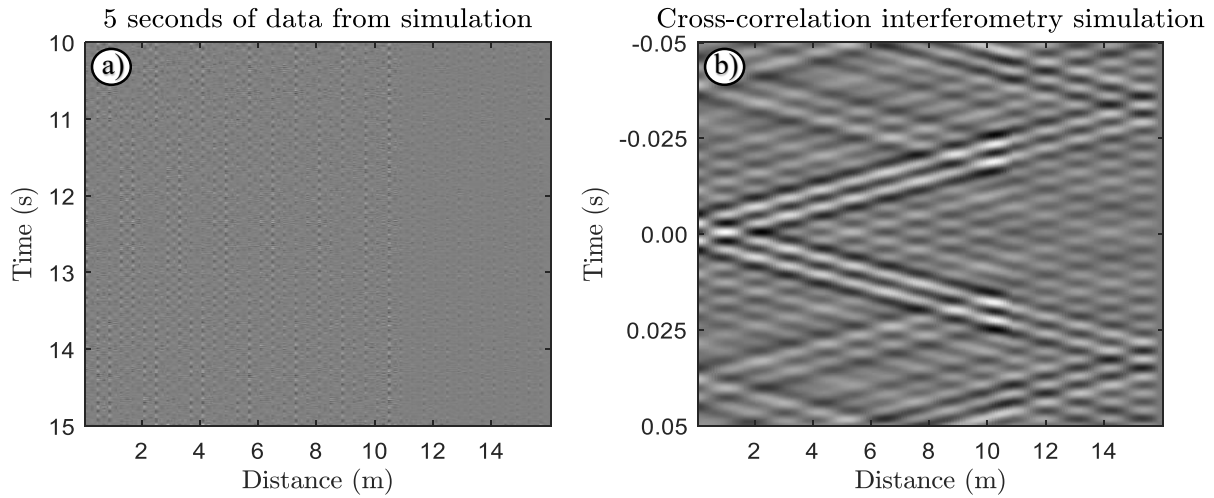


Figure 13. Simulated data and cross-correlation

5. Discussion

The cross-correlation of the experimental data in figure 10 show that the largest amplitudes are aligned with a straight line corresponding to a propagation velocity of 945 (m/s). The same is true for the amplitudes in figure 11. This is surprising since the wave speed is expected to be higher as the theoretical wave speed in equation (4) implies. One possible explanation for the low wave speed would be the presence of a tiny amount of air in the conduit. As figure 4 shows, the wave velocity is highly sensitive to the volumetric amount of air in water. Another possibility is that the data acquisition and post-processing is conducted in a way that loose vital information. Attempts to increase the frequency range to discover possible merged peaks have been made but higher resolution did not unveil a different result. It should also be noted that the Greens function between the recessed transducers (IN1-IN3) and PTIN2 needed a different filter than the flush mounted sensors. The recessed sensors gave unnaturally large amplitudes at high frequencies, as mentioned earlier a dynamic calibration was never performed. The experimental results are however promising since they show the same trends as the simulated data.

The results from the deconvolution interferometry show that the experimental and simulated data have similarities. The most significant difference is that the amplitudes in the experimental plot decrease and get smeared out while the amplitudes in the simulated plot are more constant throughout the pipe section. The simplicity of the simulated model is probably the reason for this. The simulated pipe sections are stiff, meaning that no energy is used to move or distort the pipe, and the friction term related to the acceleration of the fluid is neglected. In both plots the most significant peaks from the Green's function between the receivers follow the dashed line corresponding to the lowest wave velocity. The wave speed in the simulated data is $a = 1000$ (m/s). Both figure 11 and figure 12 show that the noise distribution is non-homogeneous since the responses are most substantial for $t > 0$, this can be compared to the situation in figure 3.

If measurement techniques allowed continuous measurement of the pressure along pipes, better pictures of how reflection points influence the flow could be produced as illustrated in figure 13. figure 13a shows a lot of noise and it is difficult to determine anything about the flow from the picture. By applying cross-correlation interferometry distinct lines appear where the cross-correlation return the greatest values, i.e. the peaks in figure 10.

6. Conclusion

Applying seismic interferometry as a post processing technique to evaluate experimental and simulated pipe flow in a penstock connected to a reaction turbine show interesting results. The technique is

promising and can be used to identify the wave speed in experimental results and to find reflection points in both experimental measurements and simulated data.

The results from the experimental data used in this paper are difficult to analyse, but they show the same behavior as the simulated results. The results indicate that the wave velocity is lower than the expected theoretical value. Further study is needed to optimize how to acquire and post-process data.

Acknowledgment

We want to thank Dr. Kjetil Håvik for his assistance during the development of this paper. The idea to try out seismic interferometry techniques appeared during conversations with Dr. Håvik. He has helped us find relevant literature, and he created the basis of the MATLAB script used for post-processing. This work would not have been done without him and his encouragement.

Reference list.

- [1] Wylie E B and Streeter V L 1983 *Fluid Transients* (Thomson-Shore, Dexter, MI, fourth edition)
- [2] Twyman J 2018 *Wave speed calculation for water hammer analysis. Obras y Proyectos*, (20), 86-92.
- [3] Dörfler P, Sick M and Coutu A 2012. *Flow-induced pulsation and vibration in hydroelectric machinery: engineer's guidebook for planning, design and troubleshooting*. Springer Science & Business Media.
- [4] Brekke H 2003 *Pumper & turbiner* Vannkraftlaboratoriet NTNU.
- [5] Jaeger C 1963 *The theory of resonance in hydropower systems. Discussion of incidents and accidents occurring in pressure systems*. Journal of Basic Engineering, 85(4), 631-640.
- [6] Chaudhry M H 1979 *Applied hydraulic transients* (No. 627 C4) New York: Van Nostrand Reinhold.
- [7] Haavik K E 2016 *Source-Depth Diversity for Enhanced Marine Seismic Imaging*. NTNU
- [8] Curtis A Gerstoft P Sato H Snieder R and Wapenaar K 2006 *Seismic interferometry—Turning noise into signal* The Leading Edge, 25(9), 1082-1092.
- [9] Wapenaar K Draganov D Snieder R Campman X & Verdel A 2010. *Tutorial on seismic interferometry: Part 1—Basic principles and applications*. Geophysics, 75(5), 75A195-75A209.
- [10] Claerbout J F 1968 *Synthesis of a layered medium from its acoustic transmission response*. Geophysics, 33(2), 264-269.
- [11] Vaezi Y 2016 *Application of Seismic Interferometry in Microseismic Monitoring*. Department of Physics, University of Alberta.
- [12] Franklin R and Wallace J M 2016 *Absolute Measurements of Static-Hole Error Using Flush Transducers*. J.Fluid Mech., 42(01), 33-48.
- [13] Antonsen Ø 2007 *Unsteady flow in wicket gate and runner with focus on static and dynamic load on runner*, NTNU
- [14] IEC 60193 1999 *Hydraulic turbines, storage pumps and pump-turbines- Model acceptance tests*, (1999-11-16)
- [15] Lobkis O I and Weaver R L 2001 *On the emergence of the Green's function in the correlations of a diffuse field*. The Journal of the Acoustical Society of America, 110(6), 3011-3017.
- [16] Snieder R and Hagerty M 2004 *Monitoring change in volcanic interiors using coda wave interferometry: Application to Arenal Volcano, Costa Rica*. Geophysical research letters, 31(9).
- [17] Garnier J and Papanicolaou G 2009 *Passive sensor imaging using cross correlations of noisy signals in a scattering medium*. SIAM Journal on Imaging Sciences, 2(2), 396-437.
- [18] Vasconcelos I and Snieder R 2007 *Interferometry by deconvolution, Part I: theory and numerical examples*. Center for Wave Phenomena and Department of Geophysics, Colorado School of Mines, Golden, CO 80401

Appendix G

Vedlegg til Risikovurderingsrapport

Francisriggen

Prosjekttittel	Interaction between turbine pressure pulsations and transients in penstock
Prosjektleder	Celine Faudot
Enhet	NTNU
HMS-koordinator	Morten Grønli
Linjeleder	Terese Løvås
Riggnavn	Francisriggen
Plassering	Vannkraftlaboratoriet
Romnummer	11,21
Riggansvarlig	Bård Aslak Brandåstrø

• VEDLEGG G FORSØKSPROSEDYRE

Experiment, name, number: Interaction between turbine pressure pulsations and transients in penstock	Date/ Sign
Project Leader: Celine Faudot	31/01 <i>Celine Faudot</i>
Experiment Leader: Celine Faudot	31/01 <i>Celine Faudot</i>
Operator, Duties: Johannes Kverno	31/1 <i>J. Kverno</i>

Conditions for the experiment:	Completed
Experiments should be run in normal working hours, 08:00-16:00 during winter time and 08.00-15.00 during summer time. Experiments outside normal working hours shall be approved.	
One person must always be present while running experiments, and should be approved as an experimental leader.	
An early warning is given according to the lab rules, and accepted by authorized personnel.	
Be sure that everyone taking part of the experiment is wearing the necessary protecting equipment and is aware of the shut down procedure and escape routes.	
Preparations	Carried out
Post the "Experiment in progress" sign.	
<i>Start up procedure</i>	
During the experiment	
<i>Control of temperature, pressure</i>	
End of experiment	
<i>Shut down procedure</i>	
Remove all obstructions/barriers/signs around the experiment.	
Tidy up and return all tools and equipment.	
Tidy and cleanup work areas.	
Return equipment and systems back to their normal operation settings (fire alarm)	
To reflect on before the next experiment and experience useful for others	
Was the experiment completed as planned and on scheduled in professional terms?	
Was the competence which was needed for security and completion of the experiment available to you?	
Do you have any information/ knowledge from the experiment that you should document and share with fellow colleagues?	

• VEDLEGG H OPPLÆRINGSPLAN FOR OPERATØRER

Experiment, name, number: Interaction between turbine pressure pulsations and transients in penstock	Date/ Sign
Project Leader: Celine Faudot	31/01 <i>C. Faudot</i>
Experiment Leader: Celine Faudot	31/01 <i>C. Faudot</i>
Operator Johannes Kverno	31/01 <i>J. Kverno</i>

Kjennskap til EPT LAB generelt	
Lab - adgang -rutiner/regler -arbeidstid	
Kjenner til evakueringsprosedyrer	
Aktivitetskalender	
Kjennskap til forsøkene	
Prosedyrer for forsøkene	
Nødstop	
Nærmeste brann/førstehjelpsstasjon	

